Development of a Miniature Electrothermal Thruster Using Microwave-Excited Microplasmas for Ultra Small Satellites

TAKAO Yoshinori

2007

Abstract

Microspacecraft have recently attracted increasing attentions in space technology for reduction of the overall mission costs. To realize such microspacecraft, every component must be miniaturized, and micropropulsion systems are no exceptions.

In this study, a miniature electrothermal thruster using microwave-excited microplasmas has been proposed. The microthruster consists of an azimuthally symmetric microplasma source and a conical converging-diverging (Laval) micronozzle. The microplasma source is composed of a dielectric tube covered with a grounded metal, having an inner radius of ∼1 mm and a length of ∼10 mm. Microwaves are injected into the plasma chamber, and then the propellant gas, Ar in this study, is ionized and heated up at pressures of 10–100 kPa. The micronozzle, with a throat diameter and length of ∼0.2 and ∼1 mm, respectively, converts high thermal energy of the plasma into directional kinetic energy, producing the thrust required.

Firstly, the microplasma source and the micronozzle flow have been computationally investigated using a numerical model consisting of three modules: a volume-averaged global model for plasma parameters, an electromagnetic model for microwaves, and a two-temperature fluid model for nozzle flows. Plasma parameters obtained for microwave powers of interest (≤ 10 W) are the plasma densities of 2.7×10^{19}–1.7×10^{22} m^{-3}, electron temperatures of 7.9×10^3–1.0×10^4 K, and heavy particle temperatures of 9.5×10^2–1.0×10^4 K. Surface waves are found to travel along the dielectric wall of the microplasma source at higher frequencies f and relative permittivities ε_d, e.g., $f > 5$ GHz at $\varepsilon_\mathrm{d} = 20$ or higher f at $\varepsilon_\mathrm{d} = 3.8$ and 9.2, resulting in the effective power deposition of microwaves. This is due to the relation between the wavelength and the chamber length, being described by theoretical dispersion equation. Supersonic flows in the diverging section of the micronozzle are decelerated because of high viscosity in thick boundary layers, where the effect is more significant under conditions in the or-

der of isothermal, radiative, and adiabatic walls. Consequently, making nozzle length short by increasing half-cone angles can improve the thrust performance in spite of divergence loss due to the large radial velocity. Thrusts of 2.5–3.5 mN and specific impulses of 130–180 s are obtained at a mass flow rate of 2.0 mg/s.

Then, a miniature plasma source was fabricated based on the numerical analysis above. The plasma source, however, could not absorb microwave powers effectively, showing the reflected power over 30 %, because of a relatively low frequency of 4 GHz, which is the available maximum value for the current setup. To reduce the reflection, the microplasma source has been improved by changing its structure, where the plasma source consists of a quartz tube 10 mm long and 1.5 mm in inner diameter and a microwave rod antenna 10 mm long covered with two types of ceramic tubes 1.0 mm in diameter. By means of optical emission spectroscopy and an electrostatic probe, it can be seen that at an Ar gas flow rate of 50 sccm, the emission intensity, electron density, and rotational temperature increase with increasing incident microwave power (2–10 W), microwave frequency (2 and 4 GHz), and dielectric constant (6 and 12–25), giving the electron densities of 10^{17}–10^{19} m^{-3} and rotational temperatures of 700–1800 K, where the rotational temperature is obtained by adding a small amount of N_2 to the Ar plasma and observing its rotational spectra. In addition, a desirable distribution of the rotational temperature is obtained for the microthruster.

Finally, performance testing of a microplasma thruster has been conducted and compared with numerical analysis, after the microplasma source is connected to a micronozzle, which is conically shaped, being fabricated in a 1.0–1.4 mm thick quartz plate with throat diameters of 0.12–0.2 mm. The thrust performance is improved by discharging the plasma; in the case of a gas flow rate of 60 sccm (1.8 mg/s), the thrust obtained is 1.4 mN giving the specific impulse of 79 s with the thrust efficiency of 8.7 % at a microwave power of 6 W, while the thrust and specific impulse are 0.9 mN and 51 s, respectively, in cold-gas operation. The pressure thrust is not negligible and contributes significantly to the total thrust. Moreover, a comparison with numerical analysis implies that the micronozzle tends to have an isothermal wall rather than an adiabatic one.

The thruster performance observed in the experiment is smaller than that estimated using the numerical model. Nonetheless, the thrust obtained is of the order of mN, which could be used for a station-keeping maneuver for microspacecraft ($\leq$ 10 kg).

Acknowledgments

I wish to express my special thanks to everyone who has helped me to complete this work for five years in Propulsion Engineering Laboratory, Department of Aeronautics and Astronautics, Graduate School of Engineering, Kyoto University (Ono Lab.).

First and foremost, I would like to thank my adviser, Prof. Kouichi Ono for his patience, insight, and assistance over the graduate course, and for giving me many chances to present papers in various international conferences. In addition to his immense knowledge of plasma physics, experimental techniques, and writing skill in English, his attitude toward education has been most invaluable.

I would also like to thank Prof. Kazuo Aoki and Prof. Takaji Inamuro for their careful review of this thesis and their valuable comments. I am again grateful to Associate Prof. Koji Eriguchi, Prof. Yuichi Setsuhara at Osaka University (the former associate professor), and Associate Prof. Kazuo Takahashi at Kyoto Institute of Technology (the former research associate) for fruitful discussion on my research and for giving me valuable advice about my life.

Many thanks to all current and former members in Ono Lab. for their encouragement and valuable discussion on plasma physics, electric propulsion, numerical methods, and experimental techniques, especially to Dr. Hiroyuki Kousaka, Dr. Yusuke Doi, Mr. Isao Fujikake, Mr. Atushi Sano, Mr. Daisuke Nakata, Mr. Shinya Sugiura, Mr. Hiroshi Yamamoto, Dr. Yugo Osano, and Mr. Keisuke Nakamura.

This research has been supported in part by a Grant-in-Aid for Scientific Research from the Ministry of Education, Culture, Sports, Science and Technology, Japan. I have also owed for three years to Research Fellowships of the Japan Society for the Promotion of Science for Young Scientists.

And last but not least, I would like to express my deepest gratitude to my family for their continuous support all my life.

Contents

1 Introduction

1.1 Nanosatellites

Microspacecraft have been considered in the aerospace community since the early 1980s and have gained increased attention ever since. The motivation behind this is the desire to reduce the overall mission costs and greatly increase launch rates. Reducing the scale of spacecraft decreases launch costs and simplifying the structure leads to short development periods. Moreover, microspacecraft mission scenarios may be envisioned where the mission is accomplished by a fleet of several microspacecraft to reduce the mission risk and increase the mission flexibility. Since loss of one microspacecraft would not eliminate the entire mission, a larger "mother"-spacecraft could release smaller microspacecraft to perform riskier portions of a mission, such as a close-up investigation of Saturn's ring objects, or the smaller microspacecraft could be placed on different trajectories around the target planet and provide an almost instantaneous, global survey of the target. Such high reliability and flexibility as well as low-cost performance are one of the greatest advantages for microspacecraft because their repair is not readily done in space [1].

These modern microspacecraft differ from spacecraft of similar mass and size, constructed at the dawn of the space age, by higher degrees of capability targeted for their subsystems as well as their scientific payloads. Improved capabilities may be achieved

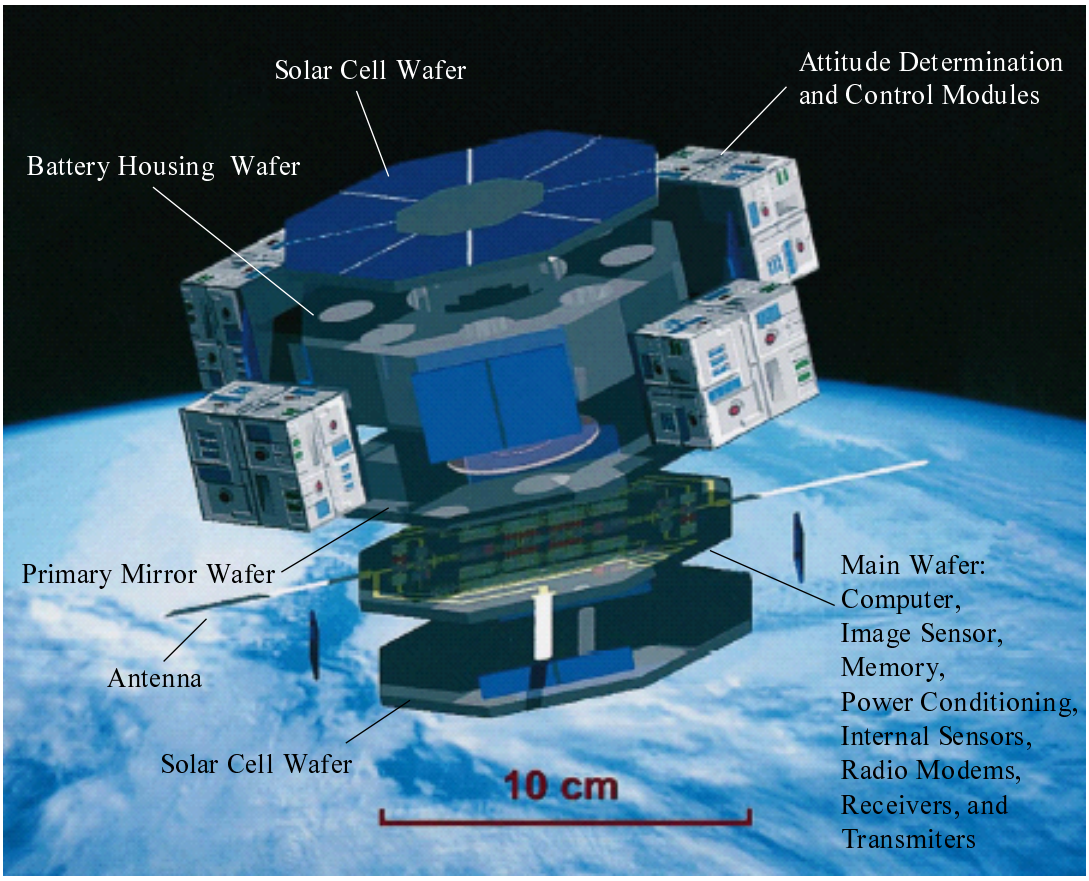

Figure 1.1: A conceptual design of microspacecraft [3].

through novel microfabrication techniques to be used in the construction of spacecraft systems and components. Such microelectromechanical systems (MEMS) technologies have progressed significantly and are anticipated to be employed to a large extent in future microspacecraft designs [2]. A conceptual design of such microspacecraft is shown in Fig. 1.1.

There currently exists a wide variety of views regarding the appropriate definition of what a microspacecraft is. In some cases, microspacecraft are classified according to their masses as follows: microsatellites (10–100 kg), nanosatellites (1–10 kg), and picosatellites (0.1–1 kg). Even a conceptual design of femtosatellites (< 100 g), which are a monolithic "satellite-on-a-chip" based on commercial complementary metal-oxide semiconductor (CMOS) technology, is presented and their use in future distributed space missions has recently been discussed [4]. To realize nanosatellites or below classes, every component must be miniaturized significantly and micropropulsion systems are

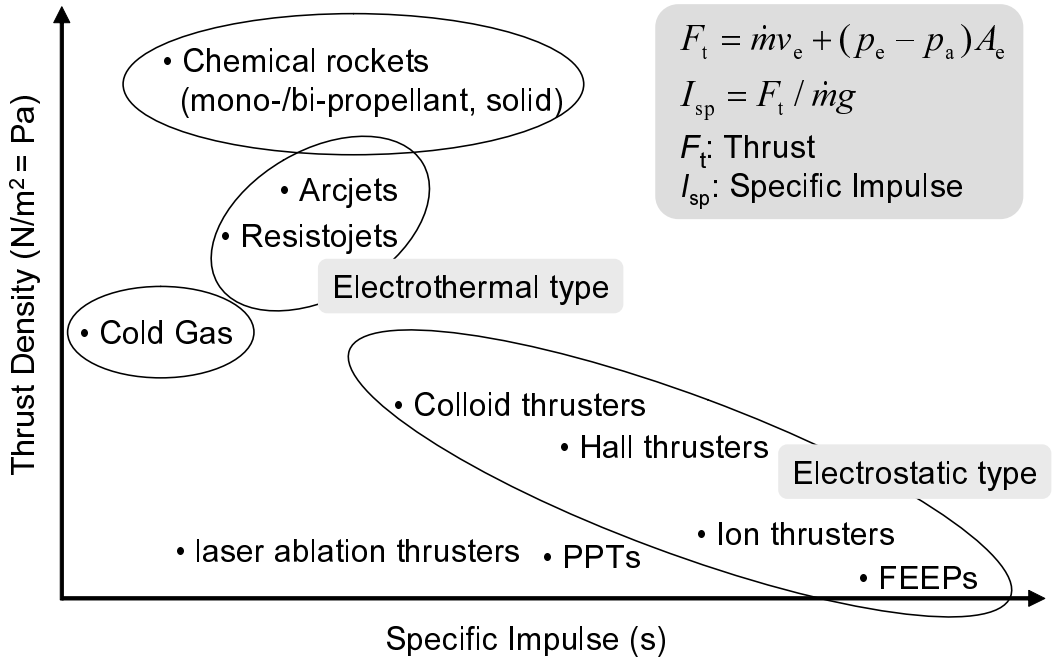

Figure 1.2: Performance of microthrusters, where $\dot{m}$ is the mass flow rate, v_e the exhaust velocity, p_e the nozzle exit pressure, p_a the ambient pressure, A_e the nozzle exit cross-sectional area, and g the gravitational constant. The thrust density is defined as F_t/A_e.

no exceptions. In addition, the power consumption should also be reduced drastically because power densities are estimated at 1 W/kg. The propulsion systems will not only consist of thrusters, but will also require miniature feed-system components, such as valves, tanks, and pressure regulators, etc. However, these areas are not taken into account and only thrusters are included in this work.

1.2 Microthrusters

Microspacecraft mission scenarios may involve a variety of propulsive maneuvers, such as attitude control, station-keeping, orbit raising/lowering, or even landing and take-off from a distant planet. Depending on the maneuver, different propulsion technologies will be needed. This paper will focus on relatively low-thrust propulsion systems which can be integrated with nanosatellites ($<$ 10 kg) for the purposes of attitude control (requiring a thrust of $\sim\mu$N) and station-keeping ($\sim$mN) maneuvers. In order to meet microspacecraft propulsion requirements, the use of lightweight, small sized, low-thrust,

and small-impulse-bit systems will be needed.

Various microthrusters have been proposed for microspacecraft applications, being under significant development for primary and attitude control: ion thrusters [5, 6], hall thrusters [7, 8], field emission thrusters (FEEPs) [9–11], colloid thrusters [12, 13], pulsed plasma thrusters (PPTs) [14], cold-gas thrusters [15], solid rocket array thrusters [16, 17], resistojets [18, 19], arcjets [20, 21], and laser-ablation thrusters [22, 23], etc., the performance of which is summarized in Fig. 1.2. Several microthrusters are briefly described below.

1.2.1 Ion thrusters

In an ion thruster, the propellant (typically xenon) is ionized in a gaseous plasma discharge. Ions are extracted from the plasma through a set of accelerator grids by means of electrostatic forces and accelerated across an electric potential difference of about 1 kV. In the process, xenon ions achieve a velocity of about 30,000 m/s, corresponding to a specific impulse of about 3000 s. Such high specific impulse is one of the greatest advantages. However, in addition to the thruster itself and the accelerator grid system, the neutralizer, which is used to neutralize the ion beam to avoid charging the spacecraft, is required, so that ion thrusters have complicated systems for miniaturization. It is also a challenging problem to discharge the plasma in a small space at very low pressures, and thus very high magnitude of magnetic fields is required for confinement of electrons in the plasma chamber. Owing to the above problems, miniature ion thrusters recently reported are relatively large thrusters for nanosatellites [5, 6], where the size is about 5 cm $\times$ 5 cm $\times$ 3 cm and the power is about 30 W.

1.2.2 Hall thrusters

Hall thrusters are electrostatic propulsion devices which often use xenon propellant, where plasma generation and ion beam acceleration are different from those in ion thrusters. In a Hall thruster, electrons emitted from a hollow cathode external to the thruster are accelerated toward a positive anode located upstream and inside an annular discharge chamber. On their way to the anode, the electrons cross a radial magnetic field extending across the annular chamber. Owing to Lorentz-force action, the electrons gyrate around the magnetic field lines and drift azimuthally through the annular channel, colliding with propellant gas atoms (xenon) and ionizing them.

The ions are accelerated away from the thruster by the same electric field that attracted the electrons. The ion beam is neutralized by additional electrons streaming off the cathode. Hall thrusters also have a high specific impulse of 1500–2000 s and are more compact for the same delivered thrust level than ion thrusters, so that Hall thrusters seem to be attractive at small scale. However, as described in ion thrusters, miniature Hall thrusters also require neutralizers and very high magnitude of magnetic fields to discharge plasmas in a small chamber at very low pressures. In addition, the plasma discharge could in turn degrade magnetic fields because of excessive heating of the thruster permanent magnets, resulting in low efficiency of ionization. The most aggressive miniature Hall thruster was about 4 mm in diameter with power over 100 W [7]. An improved miniature Hall thruster with magnets being water-cooled has recently been presented with powers of 10–40 W [8].

1.2.3 Field emission thrusters

In the field emission electric propulsion (FEEP) concept, ions are produced by field emission from a liquid metal (Cs, In, or others) surface with the metal acting as the propellant, fed into the thruster by the action of capillary forces. Typical FEEP concepts have thus several unique advantages over other electric propulsion concepts for microspacecraft applications. By avoiding the use of gaseous discharges to generate ions and instead relying on a field emission process, the FEEP concept leads to a high degree of miniaturization, circumventing issues related to high-surface/volume ratio gaseous discharges, and associated high potential electron wall losses. In addition, the use of a capillary-fed propellant supply eliminates the needs for valves and a pressurant supply. FEEP thrusters can deliver extremely small impulse bits in the 10^{-8} N s range and below with a thrust of a few micronewtons. However, the filed emission process requires high voltages (10 kV range) and thus relatively high specific power values compared with other electric propulsion devices, although they can produce fairly high specific impulse values between 6000 and 10,000 s. Some MEMS-based FEEP thrusters with field emitter array (FEA) technology have been investigated extensively and are one of the most promising microthrusters producing very low thrust and precise control of it [10, 11].

1.2.4 Colloid thrusters

Colloid thrusters are similar to FEEP devices, featuring emitter tips and accelerating electrodes resembling those used in FEEPs. However, unlike FEEP thrusters, they do not accelerate individual ions; rather, in a colloid thruster, thrust is produced by electrostatically accelerating fine charged liquid droplets ejected from a capillary. Consequently, colloid thrusters produce larger thrusts ($\sim$100 μN) and lower specific impulses ($\sim$1000 s) in comparison to FEEP thrusters. Some MEMS-based colloid thrusters have also been investigated with FEA technology, and are sometimes referred to as electrospray thrusters [12, 13].

1.2.5 Pulsed plasma thrusters

In a pulsed plasma thruster (PPT), propellant is ionized and then electromagnetically accelerated between two parallel electrodes in a pulsed mode of operation. In ablative PPT concepts, a solid Teflon bar is used as the fuel. Ablative PPTs have been valued for their relative simplicity of operation, simple propellant feed system, and compact solid propellant storage, featuring no moving parts with the exception of the fuel bar. Plasma velocities are quite high and can range between 10 and 35 km/s, resulting in high specific impulse of 1000–3500 s. PPTs can also provide very small impulse-bit values in the micronewton-second range, so that they are mainly targeted for attitude control and precise positioning. However, to ablate solid propellant PPTs require large and heavy capacitors to produce high voltages, and are characterized by low thruster efficiency and low thrust-to-power ratios.

1.2.6 Solid rocket array thrusters

Solid rocket array thrusters, so-called digital microthrusters, consist of a multitude of microfabricated, single-shot thrusters placed onto a wafer [16]. These devices may be used for attitude control, providing predetermined impulse bits by firing individual thrusters. Each thruster can be fired only once. It is estimated that the range of deliverable thrust values may be expanded to values between a few micronewtons and hundreds of millinewtons through proper selection of cavity and nozzle dimensions. Advantages of digital microthrusters are their relative simplicity, not requiring micromachined valves or complex feed systems. However, since every microthruster in

the array is located at a different moment arm with respect to the center of mass of the spacecraft, attitude control algorithms will need to take into account individual thruster locations. In addition, firing of one of the thruster arrays triggers firings of neighboring thrusters in some cases.

1.2.7 Resistojets

In a resistojet, a propellant, stored either in a gaseous or a liquid phase, is heated through conductive/convection from a heater element to vaporization, and the propellant is thermally exhausted through a nozzle. The simplicity of the device and the fact that liquid propellants may be used, allowing for compact propellant storage and reducing leakage concerns, make this concept attractive. Two types of MEMS-based resistojets have been presented so far. The one is the vaporizing liquid microthruster (VLM) [18], identifying it as a phase-change thruster concept which focuses on the use of liquid propellant, vaporizing them with heaters on demand to generate thrust, thus avoiding propellant storage and leakage concerns. The other relies on molecular flow in the heat exchanger region of the thruster and is thus termed the free molecular microresistojet (FMMR) [19]. In the FMMR concept, the thruster is operated at very low gaseous plenum pressures, typically between 50 and 500 Pa. A gas molecule entering the thruster impinges on a heated surface first before it can exit the nozzle. The exiting molecule will therefore maintain a kinetic energy equivalent to the heater temperature, being the maximum temperature inside the device, thus maximizing the achievable specific impulse. The extremely low feed pressures will ease valve leakage requirements.

1.3 Target and concept of a microplasma thruster

The first five microthrusters described in the preceding section — ion, Hall, colloid thrusters, FEEPs, and PPTs — produce low thrust and high specific impulse, while the others produce high thrust and low specific impulse, as shown in Fig. 1.2. Out of the five thrusters, FEEPs are extensively investigated for the mission of the laser interferometer space antenna (LISA). The goal of this mission is to detect low-frequency gravity waves by detecting the relative motion exerted by these waves on the spacecraft. Except such missions requiring low thrust with extremely precise thrust control, attitude control of

microspacecraft could be carried out only by magnetic torquers or reaction wheels.

Consider a station-keeping maneuver of satellites in geosynchronous Earth orbit (GEO). The dominant propulsive requirement for a GEO satellite is usually the so-called north-south station-keeping (NSSK) function. Most GEO satellites require positional accuracy to 0.05–0.1 degrees, which necessitates either occasional or near-continuous propulsive corrections amounting to Δv = 41–51 m s^{-1} year^{-1} [24]. Although the propellant mass required to compensate this Δv is only about 5 g for typical FEEPs producing a thrust of 10 μN and a specific impulse of 10,000 s, it takes such low-thrust thrusters 1.6 years even for 10 kg nanosatellites, and thus the NSSK can not be realized only by FEEPs. For thrust-oriented thrusters with a thrust of 1 mN and a specific impulse of 100 s, it takes only 5.6 days with a propellant mass of about 0.5 kg.

Compared to microthrusters with high specific impulse, there is little research on miniature plasma thrusters with high thrust. In this article, we propose a thrust-oriented miniature electrothermal thruster using microwave-excited microplasmas as shown in Fig. 1.3, which is an application of microplasma sources on which extensive research has recently been done [25–38]. The microthruster generates high-enthalpy plasmas in a cylindrical dielectric chamber 1–2 mm in diameter and 10 mm long at pressures of 10–100 kPa, exhausting them through a 1–1.4 mm long micronozzle into space, so that the thruster could produce the same thrust level of solid rocket array thrusters with higher specific impulse. The microwaves penetrate into the plasma chamber along the plasma-dielectric interfaces as surface waves even in the overdense mode, leading to power absorption in a thin skin-depth layer along the interfaces [39–41]. Such mechanism of power deposition is a great advantage in generating overdense plasmas in a very small space without magnetic-field confinement. These features would contribute to a simple structure and long-time operation, in comparison to other conventional thrusters such as ion thrusters, Hall thrusters and dc arcjet thrusters, because the present thruster requires no electrodes, neutralizers, or magnets. Moreover, the recent development of high-frequency microelectronics devices would also help to realize the microwave-excited microplasma thruster presented here. It should be noted that Ar is employed as a working gas throughout the present study for simplicity of analysis.

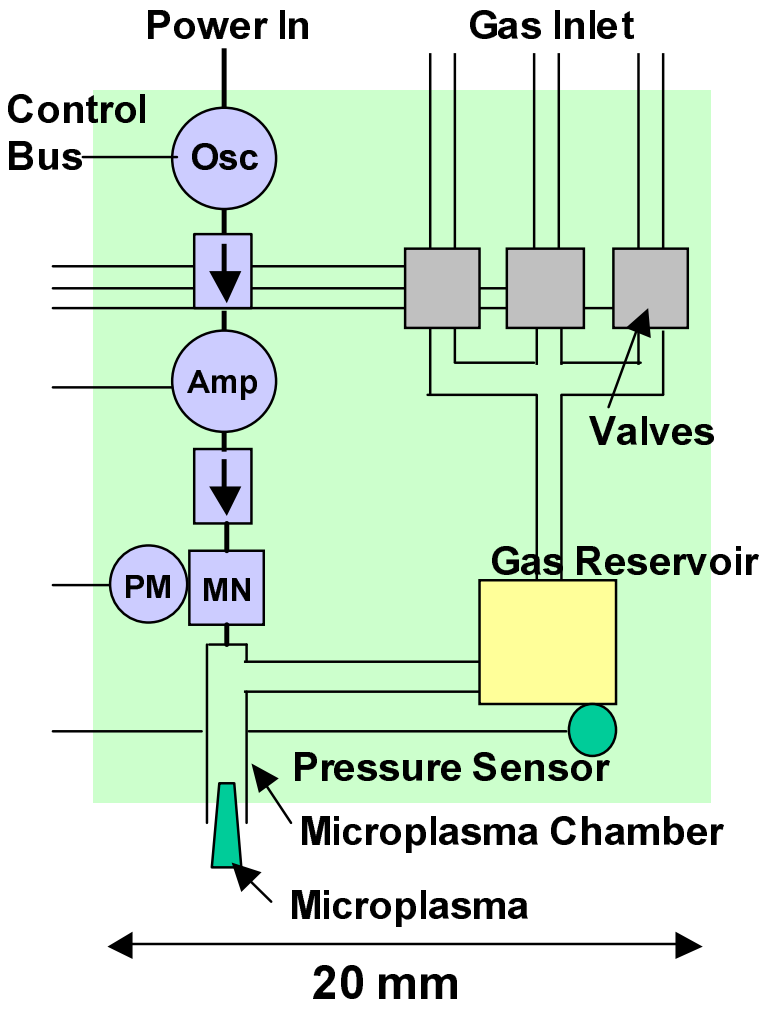

Figure 1.3: Concept of a one-chip propulsion system with a microplasma thruster. The abbreviations, Osc, Amp, PM, and MN, represent the oscillator, amplifier, power monitor, and matching network of the microwave circuits, respectively.

1.4 Constitution of the thesis

The outline of the thesis is as follows.

In Chap. 2, a numerical model consisting of three modules has been developed to estimate the thruster performance as design consideration for the microplasma thruster. Calculations are conducted separately for the microplasma source and micronozzle flow, with their characteristics being investigated, such as plasma parameters, structure of electromagnetic fields, and distribution of flow properties.

In Chap. 3, a miniature microwave-sustained plasma source has been fabricated and its plasma discharges have been demonstrated at microwave powers of interest ($\leq$ 10 W). Emissions of the Ar microplasma are also observed by means of optical emission spectroscopy to investigate its characteristics.

In Chap. 4, the miniature plasma source has been improved by employing a rod antenna structure for the microplasma source, and its optical and electrical diagnostics have been conducted to find an optimum operational condition for the microplasma thruster. Notice that the micronozzle is not attached to the plasma source at this stage.

In Chap. 5, a micronozzle has been fabricated using a micromachining process with a diamond drill, and joined to the microplasma source. The thrust performance has been measured by a combination of target and pendulum methods, being compared with numerical analysis.

Finally, Chap. 6 concludes the present study and makes some recommendations for future work.

2

Numerical design considerations

2.1 Introductory remarks

In this chapter, a numerical model has been developed to investigate plasma properties, nozzle flow characteristics, and thrust performances as a design consideration for the microplasma thruster presented. As is always the case with numerical analysis, we can not assess the accuracy and feasibility of the computational methods until the results obtained are found to be consistent with actual physical phenomena quantitatively. Nonetheless, computer simulations are useful and economical design tools for electric propulsion developments, and can produce reliable results at least qualitatively.

Figure 2.1 shows a schematic of the microwave-excited microplasma thruster, which consists of (i) a microplasma source and (ii) a micronozzle. The microplasma source is composed of a cylindrical dielectric tube, the outside of which is covered with a grounded metal. The inner radius and length of the tube are 1 and 10 mm, respectively. The micronozzle is a conical nozzle 1–2 mm long, having a converging and diverging section with a throat 0.1 mm in radius, to give supersonic flows at the nozzle exit. In the microplasma source, the propellant is ionized and heated up at around atmospheric pressures, by microwaves propagating through a coaxial cable into the plasma chamber as shown in the figure; in practice, the plasma source serves as a high-enthalpy reservoir. In the micronozzle, such high thermal energy is converted into kinetic energy to give

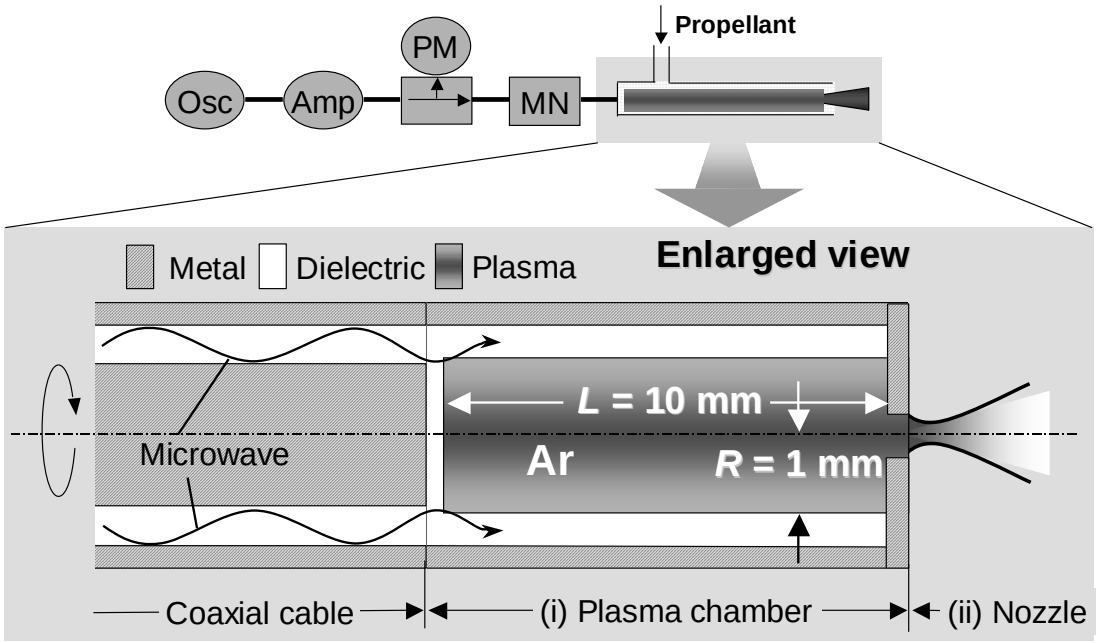

Figure 2.1: A schematic of the miniature plasma thruster using microwave-excited plasmas, which consists of an azimuthally symmetric microplasma source and a conical converging-diverging (Laval) micronozzle; the former gives high-temperature plasmas at around atmospheric pressures, and the latter converts their thermal energy into directional kinetic energy of the supersonic flow to achieve the thrust. Argon is employed as a working gas in this study. The abbreviations, Osc, Amp, PM, and MN, represent an oscillator, amplifier, power monitor, and matching network of the microwave circuits, respectively.

the thrust. We employ Ar as a working gas for simplicity.

The plasma of interest has different characteristics in the two sections, microplasma source and micronozzle. Thus, the present model for analysis consists of three modules: a volume-averaged global model (GM) module [42–47], which gives the plasma parameters such as electron density and temperature in the microplasma source; an electromagnetic model (EM) module [48, 49], which provides the electromagnetic field structures of microwaves in the microplasma source; and a fluid model (FM) module [50–52], which yields the flow properties inside the micronozzle. The GM and EM modules are combined for the analysis of the microplasma source, and the FM module is used for the analysis of micronozzle flows and thrust performances with boundary conditions at the nozzle inlet obtained from the GM module.

2.2 Model

2.2.1 Assumptions

The present model has the following general assumptions:

1. The plasma is treated as a continuum.

2. The plasma is treated by a two-temperature model; the plasma is taken to be a two-phase medium that consists of electrons and heavy particles (ions and neutrals), and the plasma is considered to be in local thermodynamic nonequilibrium with different temperatures of electrons T_e and heavy particles $T_\mathrm{h}(= T_\mathrm{i} = T_\mathrm{n})$.

3. The ionization-recombination reaction is taken into account: $\mathrm{Ar} + \mathrm{e} \leftrightarrow \mathrm{Ar}^+ + 2\mathrm{e}$.

4. The plasma is macroscopically neutral, i.e. the electron density n_e equals the ion density n_i.

5. The charged particles diffuse toward the walls according to the ambipolar diffusion theory.

6. The sheath structures are neglected at the plasma-wall interfaces.

7. In the microplasma source, the plasma parameters are treated in a volume-averaged or non-dimensional manner, while the electromagnetic fields of microwaves have axisymmetric structures in two dimensions.

8. The pressure gradients and the Lorentz force are neglected in calculating the electromagnetic fields.

9. The power of microwaves is absorbed only by electrons, and the energy absorbed is transferred to heavy particles through elastic collisions.

10. In the micronozzle, all species of particles have the same convective velocity, and the flow is laminar and axisymmetric.

2.2.2 Governing equations

Global model module

The volume-averaged GM module for the microplasma source consists of particle and energy balance equations [43]. The particle balance equations are:

$$\frac{d}{dt}n_{\mathrm{e}} = \dot{n}_{\mathrm{e}} - k_{\mathrm{diff}}, \tag{2.1}$$

$$\frac{d}{dt}n_{\mathrm{n}} = -\dot{n}_{\mathrm{e}} + k_{\mathrm{diff}} \pm S_{\mathrm{pump}}, \tag{2.2}$$

where n_{n} is the density of neutrals, $\dot{n}_{\mathrm{e}}$ is the electron source term in the bulk plasma (as will be detailed later in Sec. 2.2.3), and k_{diff} is the electron loss term through the interaction with chamber walls. Moreover, S_{pump} is a parameter to adjust the pressure p in the chamber.

In practice, solving the diffusion equations gives the density profiles of the cosine and 0th-order Bessel function forms along the axial and radial directions, respectively [42]. The ratio of the plasma density n_{s} at the sheath edge to the volume-averaged density n_{e} is given by [42, 43]

$$h_L = \left.\frac{n_{\mathrm{s}}}{n_{\mathrm{e}}}\right|_{\mathrm{axial}} = \frac{1}{0.64}\left[1 + \left(\frac{L}{\pi}\frac{u_{\mathrm{s}}}{D_{\mathrm{a}}}\right)^2\right]^{-1/2}, \tag{2.3}$$

$$h_R = \left.\frac{n_{\mathrm{s}}}{n_{\mathrm{e}}}\right|_{\mathrm{radial}} = \frac{1}{0.43}\frac{2.405 J_1(2.405)}{R}\frac{D_{\mathrm{a}}}{u_{\mathrm{s}}}, \tag{2.4}$$

where L and R are the length and radius of the chamber, D_{a} is the ambipolar diffusion coefficient, u_{s} is the reduced Bohm velocity, and J_1 is the 1st-order Bessel function.

The reduced Bohm velocity is expressed as [53]

$$u_{\mathrm{s}} = u_{\mathrm{B}} \left(1 + \frac{\pi \lambda_{\mathrm{De}}}{2\lambda_{\mathrm{i}}}\right)^{-1/2}, \tag{2.5}$$

where u_{B} is the Bohm velocity, λ_{i} is the ion mean free path, and λ_{De} is the electron Debye length. The loss term is then given by

$$k_{\mathrm{diff}} = n_{\mathrm{e}} u_{\mathrm{s}} \frac{A_{\mathrm{eff}}}{V}, \tag{2.6}$$

where $V = \pi R^2 L$ is the plasma volume and A_{eff} is the effective surface area of chamber walls given by

$$A_{\mathrm{eff}} = 2\pi R(Lh_R + Rh_L). \tag{2.7}$$

The energy balance equations are:

$$\frac{d}{dt}\left(\frac{3}{2} n_{\mathrm{e}} k_{\mathrm{B}} T_{\mathrm{e}}\right) = Q_{\mathrm{abs}} - Q_{\mathrm{iz}} - Q_{\mathrm{e}} - Q_{+} - Q_{\mathrm{elas}} - Q_{\mathrm{rad}}, \tag{2.8}$$

$$\frac{d}{dt}\left(\frac{3}{2} n_{\mathrm{h}} k_{\mathrm{B}} T_{\mathrm{h}}\right) = Q_{\mathrm{elas}} - Q_{\mathrm{diff}}, \tag{2.9}$$

where k_{B} is the Boltzmann constant, $n_{\mathrm{h}} = n_{\mathrm{n}} + n_{\mathrm{i}}$ is the density of heavy particles. Moreover, Q_{abs} denotes the absorbed power in the plasma, Q_{iz} the volumetric energy exchange due to the ionization and recombination, Q_{e} the kinetic energy loss of electrons to the walls, Q_{+} the kinetic energy loss of ions to the walls, Q_{elas} the volumetric energy exchange due to the elastic collision between electrons and heavy particles, Q_{rad} the volumetric radiative energy loss, and Q_{diff} the kinetic energy loss of heavy particles to the walls; all of them have the dimension of the power per unit volume (as will be detailed later in Sec. 2.2.3).

Electromagnetic model module

The EM module for the microplasma source is composed of Maxwell's equations for electromagnetic fields of microwaves and equations for plasma electrons [48, 49]:

$$\nabla \times \boldsymbol{E} = -\frac{\partial \boldsymbol{B}}{\partial t}, \tag{2.10}$$

$$\nabla \times \boldsymbol{B} = \mu_0 \left(\boldsymbol{j} + \varepsilon_{\mathrm{r}} \varepsilon_0 \frac{\partial \boldsymbol{E}}{\partial t}\right), \tag{2.11}$$

$$m_{\mathrm{e}} \frac{\partial \boldsymbol{u}_{\mathrm{e}}}{\partial t} = -e\boldsymbol{E} - m_{\mathrm{e}} \nu_{\mathrm{e}} \boldsymbol{u}_{\mathrm{e}}, \tag{2.12}$$

$$\boldsymbol{j} = -e n_{\mathrm{e}} \boldsymbol{u}_{\mathrm{e}}, \tag{2.13}$$

where $\boldsymbol{E}$ is the electric fields, $\boldsymbol{B}$ the magnetic fields, $\boldsymbol{j}$ the plasma current density, ε_0 the electric permittivity of vacuum, ε_r the relative permittivity, μ_0 the magnetic permeability of vacuum, e the electron charge, m_e the electron mass, $\boldsymbol{u}_\mathrm{e}$ the electron mean velocity driven by electromagnetic waves, and ν_e the momentum transfer collision frequency between electrons and heavy particles. Assuming the azimuthal symmetry of the configuration ($\partial/\partial\theta = 0$), only the transverse magnetic (TM) waves exist in the plasma chamber [54, 55].

Fluid model module

The FM module for the micronozzle consists of the two-temperature Navier-Stokes equations and the equation of state [50, 52]. The total mass continuity equation is described as

$$\frac{\partial}{\partial t}\rho + \nabla\cdot(\rho\boldsymbol{v}) = 0, \tag{2.14}$$

where $\boldsymbol{v}$ is the convective velocity and the total mass density is defined as

$$\rho = m_\mathrm{e}n_\mathrm{e} + m_\mathrm{h}n_\mathrm{h}. \tag{2.15}$$

The first term of the right hand side is negligibly small, so that the mass density can be described as $\rho = m_\mathrm{h}n_\mathrm{h}$, where $m_\mathrm{h}(= m_\mathrm{i} = m_\mathrm{n})$ is the mass of heavy particles.

The momentum conservation equation is described as

$$\frac{\partial}{\partial t}(\rho\boldsymbol{v}) + \nabla\cdot(\rho\boldsymbol{v}\boldsymbol{v}) = -\nabla p + \nabla\boldsymbol{\tau}, \tag{2.16}$$

where p is the pressure and $\boldsymbol{\tau}$ is the stress tensor expressed as

$$\tau_{ij} = \eta\left(\frac{\partial v_i}{\partial x_j} + \frac{\partial v_j}{\partial x_i}\right) - \frac{2}{3}\eta\delta_{ij}\frac{\partial v_k}{\partial x_k}, \tag{2.17}$$

with η the viscosity and the δ_{ij}, the Kronecker delta.

Moreover, the conservation equation for electrons is separately given by

$$\frac{\partial}{\partial t}n_\mathrm{e} + \nabla\cdot(n_\mathrm{e}\boldsymbol{v}) = \nabla\cdot(D_\mathrm{a}\nabla n_\mathrm{e}) + \dot{n}_\mathrm{e}, \tag{2.18}$$

where D_a is the ambipolar diffusion coefficient, and $\dot{n}_\mathrm{e}$ is the electron source term which is the same as that in Eqs. (2.1) and (2.2).

The energy equations of electrons and heavy particles are given by

$$\frac{\partial}{\partial t}\left(\frac{3}{2}n_{\mathrm{e}}k_{\mathrm{B}}T_{\mathrm{e}}\right)+\nabla\cdot\left(\frac{5}{2}n_{\mathrm{e}}k_{\mathrm{B}}T_{\mathrm{e}}\boldsymbol{v}\right)=(\boldsymbol{v}\cdot\nabla)\,p_{\mathrm{e}}-\nabla\cdot\boldsymbol{q}_{\mathrm{e}}-Q_{\mathrm{elas}}-Q_{\mathrm{iz}}-Q_{\mathrm{rad}}, \tag{2.19}$$

$$\frac{\partial}{\partial t}\left(\frac{3}{2}n_{\mathrm{h}}k_{\mathrm{B}}T_{\mathrm{h}}\right)+\nabla\cdot\left(\frac{5}{2}n_{\mathrm{h}}k_{\mathrm{B}}T_{\mathrm{h}}\boldsymbol{v}\right)=(\boldsymbol{v}\cdot\nabla)\,p_{\mathrm{h}}+\boldsymbol{\tau}:\nabla\boldsymbol{v}-\nabla\cdot\boldsymbol{q}_{\mathrm{h}}+Q_{\mathrm{elas}}, \tag{2.20}$$

where $p_s\,(s=\mathrm{e},\mathrm{h})$ is the pressure, $\boldsymbol{q}_s\,(s=\mathrm{e},\mathrm{h})$ is the heat flux defined as

$$\boldsymbol{q}_s=-\kappa_s\nabla T_s, \tag{2.21}$$

and the loss terms Q_{elas}, Q_{iz}, and Q_{rad} are the same as those in Eqs. (2.8) and (2.9). The thermal conductivity $\kappa_s\,(s=\mathrm{e},\mathrm{h})$ is taken from Ref. [56], and the viscosity is given by

$$\eta=\frac{4m_{\mathrm{h}}}{15k_{\mathrm{B}}}\kappa_{\mathrm{h}}. \tag{2.22}$$

It should be noted that the electron viscous dissipation $\boldsymbol{\tau}_{\mathrm{e}}:\nabla\boldsymbol{v}$ is neglected, because its effect is very small compared to the other terms in Eq. (2.19) [57].

Finally, the equation of state is written as

$$p=p_{\mathrm{e}}+p_{\mathrm{h}}=n_{\mathrm{e}}k_{\mathrm{B}}T_{\mathrm{e}}+n_{\mathrm{h}}k_{\mathrm{B}}T_{\mathrm{h}}=n_{\mathrm{e}}k_{\mathrm{B}}(T_{\mathrm{e}}+T_{\mathrm{h}})+n_{\mathrm{n}}k_{\mathrm{B}}T_{\mathrm{h}}. \tag{2.23}$$

2.2.3 Source terms

The volumetric ionization-recombination rate can be written as

$$\dot{n}_{\mathrm{e}}=k_{\mathrm{iz}}n_{\mathrm{n}}n_{\mathrm{e}}-k_{\mathrm{re}}n_{\mathrm{e}}^3, \tag{2.24}$$

where k_{iz}, k_{re} are the electron-impact ionization and three-body electron-ion recombination rate constants, respectively. The ionization rate constant k_{iz} is taken from Ref. [58], being expressed as

$$k_{\mathrm{iz}}=S_1\left[\frac{32}{\pi}\left(\frac{m_{\mathrm{e}}+m_{\mathrm{h}}}{m_{\mathrm{e}}m_{\mathrm{h}}}\right)\right]^{1/2}(k_{\mathrm{B}}T_{\mathrm{e}})^{3/2}\left(\frac{\epsilon_1}{2k_{\mathrm{B}}T_{\mathrm{e}}}+1\right)\exp\left(-\frac{\epsilon_1}{k_{\mathrm{B}}T_{\mathrm{e}}}\right), \tag{2.25}$$

where S_1 is the first excitation collision cross-section parameter, and ϵ_1 is the first excitation energy. The recombination rate constant k_{re} is determined from the principle of detailed balancing:

$$\frac{k_{\mathrm{iz}}}{k_{\mathrm{re}}}=\frac{2g_1}{g_0}\left(\frac{2\pi m_{\mathrm{e}}k_{\mathrm{B}}T_{\mathrm{e}}}{h_0^2}\right)^{3/2}\exp\left(-\frac{\epsilon_{\mathrm{iz}}}{k_{\mathrm{B}}T_{\mathrm{e}}}\right), \tag{2.26}$$

where h_0 is Planck's constant, ϵ_{iz} is the ionization energy, and g_0 and g_1 are the partition functions for the neutrals and ions, respectively. In this study, $S_1 = 4.369\times10^{-3}$ m^2 J^{-1}, $\epsilon_1 = 1.869 \times 10^{-18}$ J, $\epsilon_{\mathrm{iz}} = 2.525 \times 10^{-18}$ J, $g_0 = 1$, and $g_1 = 4 + 2\exp(-2059/T_{\mathrm{e}})$ with T_{e} in Kelvin are taken for Ar of interest [56, 59].

The absorbed power P_{abs} in the plasma is assumed to arise only from the classical ohmic heating, being given by

$$P_{\mathrm{abs}} = \frac{1}{t_{\mathrm{p}}}\int_{t_{\mathrm{p}}} dt \int_V \boldsymbol{j}\cdot\boldsymbol{E}\; dV, \tag{2.27}$$

where t_{p} is the period of the electromagnetic waves, and the absorbed power per unit volume is obtained from $Q_{\mathrm{abs}} = P_{\mathrm{abs}}/V$.

The volumetric ionization-recombination energy source term is described as

$$Q_{\mathrm{iz}} = \epsilon_{\mathrm{iz}}\dot{n}_{\mathrm{e}}. \tag{2.28}$$

The volumetric energy exchange due to the elastic collision between electrons and heavy particles is expressed as

$$Q_{\mathrm{elas}} = 3\frac{m_{\mathrm{e}}}{m_{\mathrm{h}}} n_{\mathrm{e}}\nu_{\mathrm{e}}k_{\mathrm{B}}(T_{\mathrm{e}} - T_{\mathrm{h}}), \tag{2.29}$$

where the momentum transfer collision frequency ν_{e} is the sum of the electron-ion ν_{ei} [57] and electron-neutral ν_{en} [56] collision frequencies. Similarly, the momentum transfer collision frequency ν_{i} is taken to be the sum of the ion-electron $\nu_{\mathrm{ie}} = \nu_{\mathrm{ei}}$ and ion-neutral ν_{in} [56] collision frequencies, which gives the ion mean free path $\lambda_{\mathrm{i}} = v_{\mathrm{th,i}}/\nu_{\mathrm{i}}$ in Eq. (2.5) with the ion thermal velocity $v_{\mathrm{th,i}}$.

The volumetric radiative energy loss is expressed as the sum of the electron-neutral free-free radiation, electron-ion free-free radiation, and line radiation [59]:

$$Q_{\mathrm{rad}} = 53.759\,\hat{n}_{\mathrm{e}}^{1.25}\hat{n}_{\mathrm{n}} + 910\,\hat{n}_{\mathrm{e}}^2 + 2.572\times10^4\,\hat{n}_{\mathrm{e}}^{1.57}, \tag{2.30}$$

where Q_{rad} is in W m^{-3}, and $\hat{n}_{\mathrm{e}} = n_{\mathrm{e}}/10^{20}$ and $\hat{n}_{\mathrm{n}} = n_{\mathrm{n}}/10^{24}$ are the dimensionless electron and neutral densities with n_{e} and n_{n} in m^{-3}.

A part of the input or absorbed power is lost through kinetic energy loss of charged particles to the walls [44, 45]:

$$Q_{\mathrm{e}} = 2k_{\mathrm{B}}T_{\mathrm{e}}\, n_{\mathrm{e}}u_{\mathrm{s}}\frac{A_{\mathrm{eff}}}{V}, \tag{2.31}$$

for electrons, and

$$Q_+ = \Delta\Phi\, n_\mathrm{e} u_\mathrm{s} \frac{A_\mathrm{eff}}{V}, \tag{2.32}$$

for ions. Here, $\Delta\Phi$ is the potential drop between the bulk plasma and the wall, which is divided into the pre-sheath drop $\Delta\Phi_\mathrm{p}$ and the sheath drop $\Delta\Phi_\mathrm{s}$ as follows [60]:

$$\Delta\Phi = \Delta\Phi_\mathrm{p} + \Delta\Phi_\mathrm{s}, \tag{2.33}$$

where

$$\Delta\Phi_\mathrm{p} = \frac{1}{2} m_\mathrm{h} u_\mathrm{s}^2, \tag{2.34}$$

$$\Delta\Phi_\mathrm{s} = k_\mathrm{B} T_\mathrm{e} \ln\left[\frac{1}{4\,u_\mathrm{s}}\left(\frac{8 k_\mathrm{B} T_\mathrm{e}}{\pi m_\mathrm{e}}\right)^{1/2}\right]. \tag{2.35}$$

The thermal energy of heavy particles is lost to chamber walls through heat transfer; according to Newton's law of cooling, the mechanism is simply expressed as [61]

$$Q_\mathrm{diff} = \alpha_\mathrm{diff}(T_\mathrm{h} - T_\mathrm{w})\frac{A}{V}, \tag{2.36}$$

where $A = 2\pi R(L + R)$ is the surface area of the plasma chamber, T_w is the wall temperature, and α_diff is the heat transfer coefficient which is an adjusted parameter of the order of 10 in W m^{-2} K^{-1} between solid and gas phases.

2.2.4 Numerical procedures

Coordinate system

Figure 2.2 shows a computational domain of the microplasma source in this study. The cylindrical coordinates $(x - r)$ are employed, with the xr origin being placed on the x axis at the left end of the coaxial cable. The plasma column, covered with 0.6 mm thick dielectrics (relative permittivity $\varepsilon_\mathrm{r} = \varepsilon_\mathrm{d}$), is 10 mm in length (between $x = 2$ and 12 mm) and 1 mm in radius. The transverse electromagnetic (TEM) waves are injected into the system at the excitation plane ($x = 0.8$ mm) of the coaxial cable, the insulator of which is made of teflon (relative permittivity $\varepsilon_\mathrm{r} = \varepsilon_\mathrm{i} = 2.1$). The area is divided into 600 cells in the axial direction and 80 cells in the radial direction at regular intervals using rectangular cells.

Figure 2.3 shows the cross-sectional view and computational grids for three types of micronozzles of interest: 10°-, 20°-, and 30°-half-angle conical nozzles to investigate

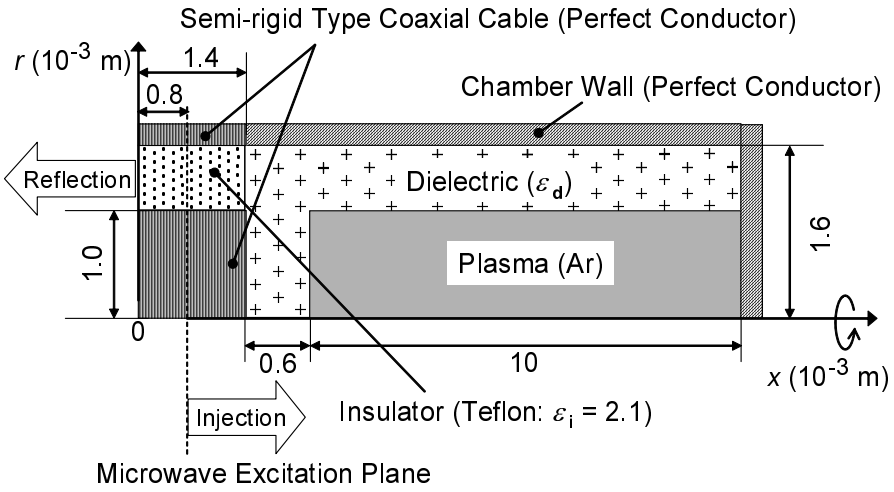

Figure 2.2: Simulation area for the microplasma source including the coaxial cable region for microwave injection. The cylindrical coordinates $(x - r)$ are employed, with the xr origin being placed on the x axis at the left end of the cable. The plasma column is 10 mm in length (between $x = 2$ and 12 mm) and 1 mm in radius, being covered with a cylindrical dielectric tube 0.6 mm in thickness and then with a metal grounded. The simulation area is divided into 600 cells in the axial direction and 80 cells in the radial direction.

the angle dependence. The inlet, throat, and exit radii of the three nozzles are all the same with 0.3, 0.1, and 0.4 mm, respectively, and the throat is located at $x = 0.3$ mm; however, the nozzle lengths and wall contours are taken to be different from one another. The simulation area of each nozzle is divided into 110 cells in the axial direction with the grid spacing being finer near the throat, and 30 cells in the radial direction at regular intervals.

Numerical scheme

In the GM module for microplasma sources, the set of ordinary differential Eqs. (2.1), (2.2), (2.8), and (2.9) are solved using the 4th-order Runge-Kutta method, to obtain the plasma parameters for given pressures p and absorbed power densities $Q_{\rm abs}$. In the EM module for microplasma sources, Eqs. (2.10)–(2.13) are solved using the finite-difference time-domain (FDTD) approximation [62], where the position of the electromagnetic properties defined at each cell is the same as that in Ref. [48], except that z is replaced by x in the present coordinate system.

In the FM module for micronozzle flows, Eqs. (2.14), (2.16), and (2.18)–(2.20)

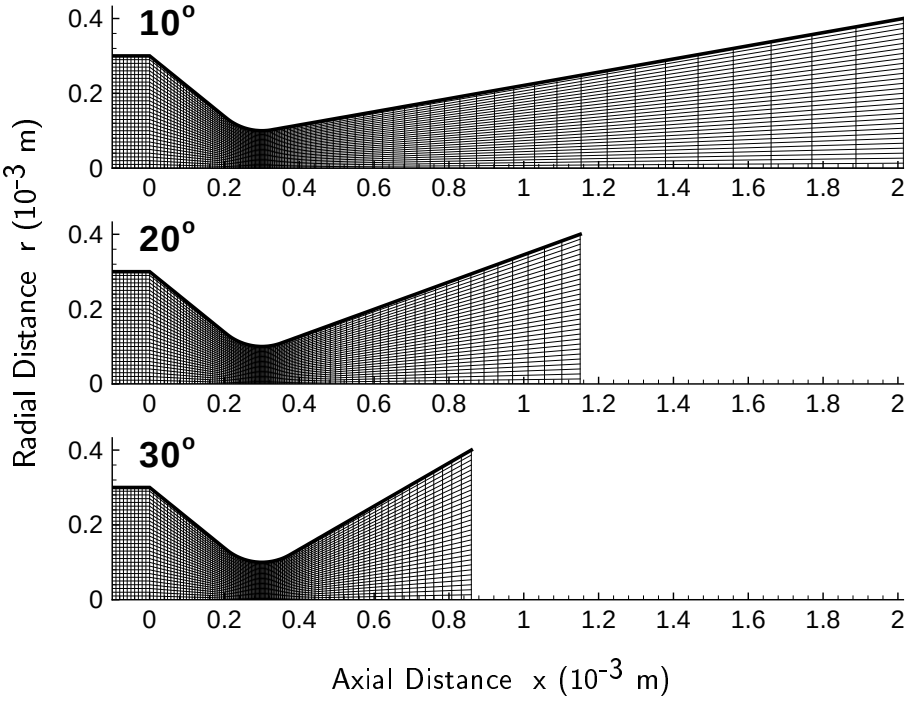

Figure 2.3: Cross-sectional view and computational grids for three types of micronozzles with a half-cone angle of 10°, 20°, and 30°. The radii of the nozzle inlet, throat, and exit are the same for the three, being 0.3, 0.1, and 0.4 mm, respectively. The nozzle throat is located at $x = 0.3$ mm; however, the nozzle lengths and wall contours are taken to be different from one another. The simulation area of each nozzle is divided into 110 cells in the axial direction and 30 cells in the radial direction.

are all discretized in a finite difference manner, and all flow properties are defined at the corners of each cell. The discretized equations are solved with the MacCormack method, which is one of the simplest schemes to solve the equations for flow fields [63]. However, coupling the electron energy equation (2.19) with the others causes the equation system to be extremely stiff and unstable; thus, we decouple Eq. (2.19) and solve it iteratively in a steady form with the line relaxation method [64]. Here, the values of T_e from Eq. (2.19) are used for the other terms which have transport properties, so that we solve Eq. (2.19) and the other Navier-Stokes equations alternately every several iterations and time steps, respectively [51].

Boundary conditions

In the GM module, the heat transfer coefficient is taken to be $\alpha_\mathrm{diff} = 10$ by comparison with the experimental and numerical analyses of plasma jets [65–68], and the wall temperature is to be $T_\mathrm{w} = 500$ K.

In the EM module, Mur's first-order absorbing boundary condition [69],

$$\frac{\partial E_r}{\partial x} - \frac{1}{c}\frac{\partial E_r}{\partial t} = 0, \tag{2.37}$$

is applied to the field component E_r at the left end of the coaxial cable ($x = 0$), so that the electromagnetic waves propagating from the chamber to the excitation plane leave the simulation area without any artificial reflection. Here, c denotes the speed of electromagnetic waves in the insulator of the cable. Since all metallic parts are treated as perfectly conducting materials, the electric field components normal to metal surfaces are set to be zero. At the centerline ($r = 0$), the cylindrical symmetry of the problem implies that $E_r = 0$ and $\partial E_x/\partial r = 0$. In the dielectric region, moreover, the current density is set to be zero ($\boldsymbol{j} = \boldsymbol{0}$) with a relative permittivity ε_r. From Eqs. (2.12) and (2.13), the plasma is treated as a dielectric material of relative permittivity

$$\varepsilon_\mathrm{r} = \varepsilon_\mathrm{p} = 1 - \frac{(\omega/\omega_\mathrm{pe})^{-2}}{1 - \mathrm{j}(\nu_\mathrm{e}/\omega)}, \tag{2.38}$$

where j is the square root of -1, ω is the angular frequency of electromagnetic waves, and $\omega_\mathrm{pe} = (n_\mathrm{e}e^2/m_\mathrm{e}\varepsilon_0)^{1/2}$ is the plasma electron frequency [42].

In the FM module, the following boundary conditions are employed: (i) At the inlet of the nozzle, we use the flow properties, such as pressure, temperature, and electron density, obtained from the GM module, and give the values in the radial direction

uniformly. The radial velocity is set to be zero, and the axial velocity is obtained by extrapolation from the downstream point adjacent to the inlet [50, 63, 70]. (ii) At the exit, all properties are extrapolated from the interior, although some portion of the exit flow near the nozzle wall is subsonic. The effect of ambient pressure is assumed to be very small as long as the pressure is sufficiently low, which is normally satisfied in space [70, 71]. (iii) On the axis of symmetry ($r = 0$), the radial velocity and the radial derivatives of the other flow properties are set to be zero. (iv) On the nozzle walls, the non-slip conditions are imposed for velocity, and the pressure and electron temperature gradients normal to the walls are set to be zero. The walls are assumed to be non-catalytic, so that the electron density gradient normal to the walls is also taken to be zero. For the heavy particle temperature, moreover, three types of boundary conditions are employed: (a) adiabatic, (b) radiative, and (c) isothermal walls. These conditions are expressed as

$$\text{(a)} \qquad \left.\frac{\partial T_\mathrm{h}}{\partial n}\right|_\mathrm{w} = 0, \tag{2.39}$$

$$\text{(b)} \qquad \lambda_\mathrm{h}\left.\frac{\partial T_\mathrm{h}}{\partial n}\right|_\mathrm{w} = \epsilon\sigma T_\mathrm{w}^4, \tag{2.40}$$

$$\text{(c)} \qquad T_\mathrm{h}|_\mathrm{w} = 500 \text{ K}, \tag{2.41}$$

where $\epsilon = 1.0$ and $\sigma = 5.67 \times 10^{-8}$ W m^{-2} K^{-4} are the emissivity and the Stefan-Boltzmann constant, respectively, $\partial/\partial n$ is the derivative normal to the walls, and the subscript 'w' represents the values thereat.

Method for calculation

Figure 2.4 shows a schematic of the method for calculation in this study. (i) In the EM module, given the microwave input power P_in, electron and neutral densities n_e, n_n, and electron and heavy particle temperatures T_e, T_h, the electromagnetic fields of microwaves injected are calculated with a time increment $\Delta t = 4.5 \times 10^{-14}$ s for a time span of typically several microwave periods. (ii) The absorbed power density Q_abs in the plasma is calculated at the end of the EM module calculation, which is an input parameter to the GM module. (iii) Then, the GM module provides the plasma parameters, which in turn are reflected in the momentum and current equations of the EM module. These procedures (i)–(iii) are repeated until the plasma properties converge.

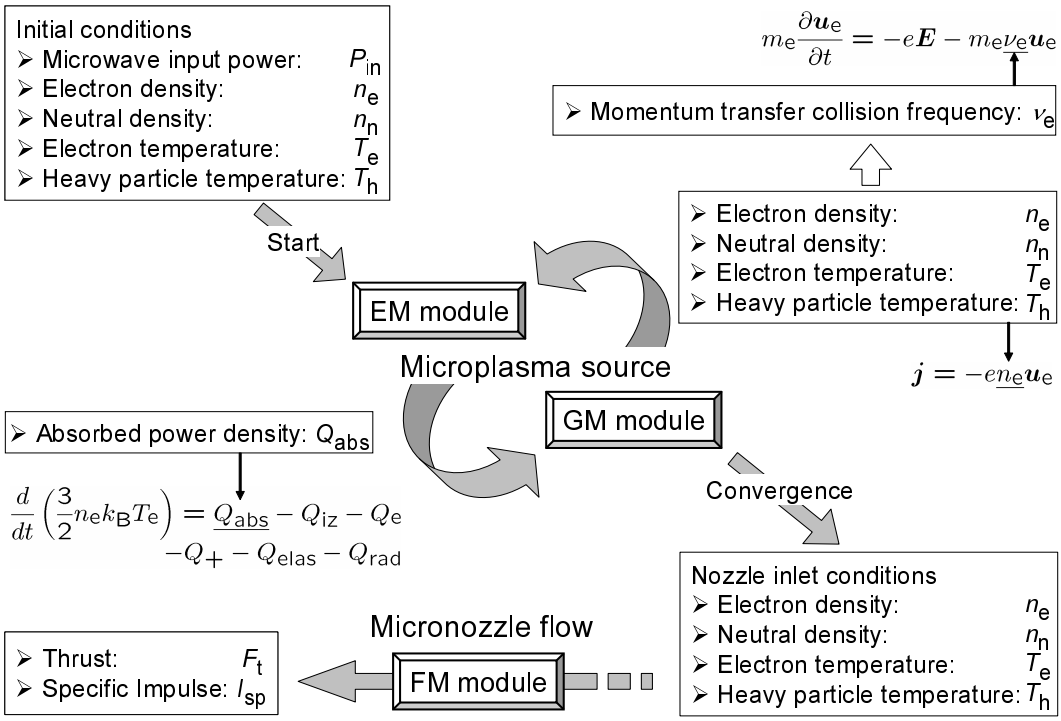

Figure 2.4: Numerical procedure of the present simulation for the microplasma thruster. The initial conditions are given to the electromagnetic model (EM) module. Both the EM and global model (GM) modules are calculated alternately until the steady state is obtained for microplasma properties. Then, using these results as the nozzle inlet conditions, the fluid model (FM) module is calculated to yield the micronozzle flow characteristics and thus the thrust performance.

(iv) The GM module gives the nozzle inlet conditions in the FM module, where the flow properties are calculated inside the nozzle to give the thrust performance.

2.3 Microplasma source

2.3.1 Plasma parameters

Figures 2.5(a) and (b) show the plasma parameters as a function of absorbed power density $Q_{\rm abs}$ at a pressure $p = 1.0 \times 10^5$ Pa, calculated with the GM module. The electron density $n_{\rm e}$ achieved is in the range 10^{19}–10^{22} m^{-3} ; $n_{\rm e}$ increases with increasing $Q_{\rm abs}$, which leads to an increase in the heavy particle temperature $T_{\rm h}$ because of a high rate of the energy exchange through elastic collisions between electrons and heavy particles. The increase in $T_{\rm h}$ naturally results in a decrease in the neutral density $n_{\rm n}$ at a fixed pressure p; and the ionization degree α increases with increasing $Q_{\rm abs}$ being

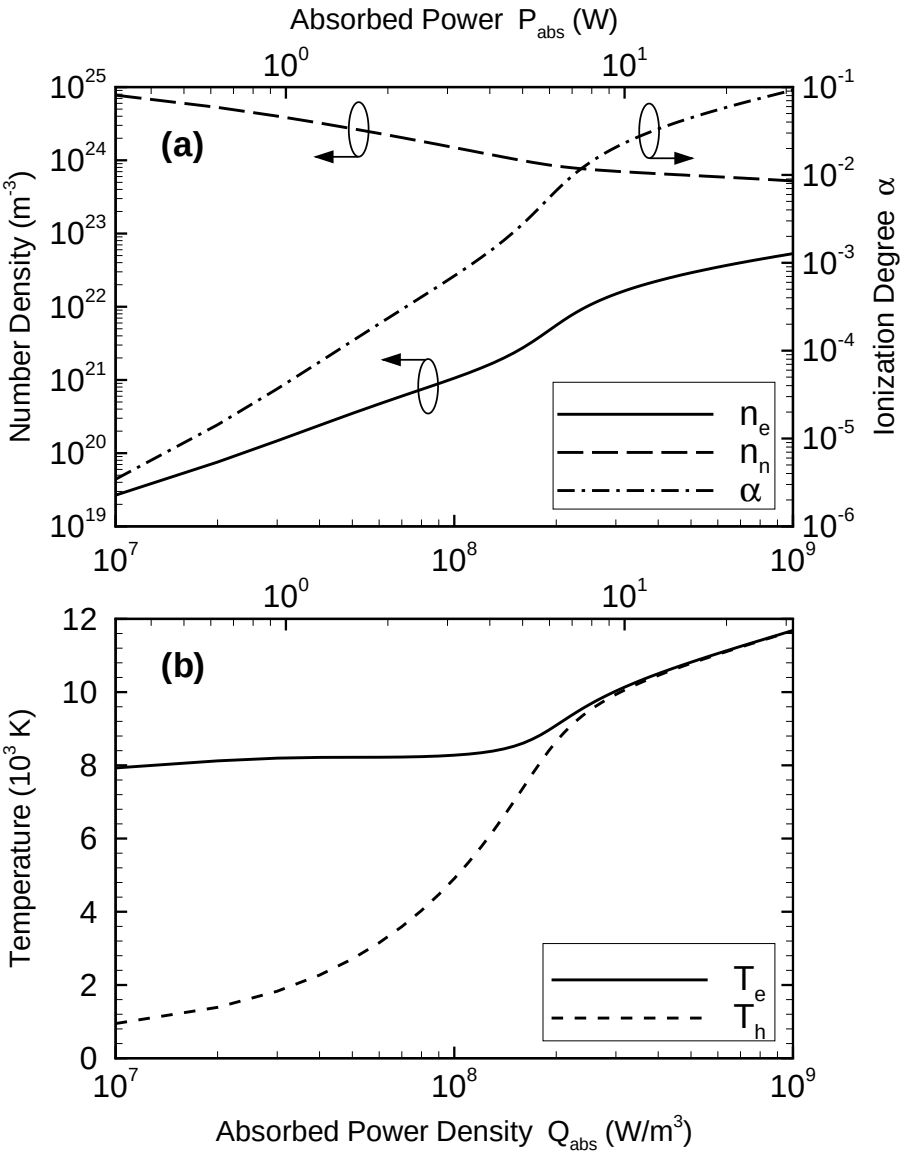

Figure 2.5: Plasma parameters in the microplasma source as a function of absorbed power density Q_{abs}, calculated at a pressure $p = 1.0 \times 10^5$ Pa. (a) Electron and neutral densities n_{e}, n_{n}, and ionization degree α; and (b) electron and heavy particle temperatures T_{e}, T_{h}. Note that the absorbed power $P_{\mathrm{abs}} = Q_{\mathrm{abs}}V$, where V is the plasma volume.

in the range 10^{-6}–10^{-1}. The electron temperature T_e remains almost constant below $Q_{abs} \approx 2.0 \times 10^8$ W/m^3 ($P_{abs} \approx 6.3$ W), while increases with increasing Q_{abs} above this value. Adequate electron density for thermal equilibrium is obtained even in a small space at a high power density of the order of $Q_{abs} \approx 10^8$ W/m^3 [72].

2.3.2 Power absorption

Calculations of the GM and EM modules were performed for different microwave frequencies f and relative permittivities ε_d of dielectrics with a microwave input power $P_{in} = 10$ W at a pressure $p = 1.0 \times 10^5$ Pa. Figures 2.6(a)–(c) show the absorbed power P_{abs} as a function of frequency f for $\varepsilon_d = 3.8$, 9.2, and 20, respectively, indicating that P_{abs} tends to increase with increasing f and ε_d with some local peaks. Note that the calculations did not converge under conditions of $f < 3$ GHz, $\varepsilon_d = 3.8$ and of $f < 2$ GHz, $\varepsilon_d = 9.2$, owing to low P_{abs}. The power which is not absorbed in the plasma is reflected and leaves the simulation area. Since the wavelength of electromagnetic fields decreases with increasing f and the propagation speed of the fields decreases with increasing ε_d, the microwaves have enough time to deposit their power into the plasma at higher f and ε_d, resulting in higher P_{abs}.

The local peaks of P_{abs} seem to occur periodically; e.g. in Fig. 2.6(c), the periodical rises and drops occur at every 3 GHz above $f = 4$ GHz, except at $f = 23$ GHz where the plasma absorbs most of the microwave input power. Figures 2.7(a)–(c) show the two-dimensional distribution of the average absorbed power density $W_{abs} = (1/t_p) \int_t^{t+t_p} \boldsymbol{j} \cdot \boldsymbol{E}\, dt$ in the plasma for $f = 1$, 4, and 23 GHz with $\varepsilon_d = 20$, where the electron densities achieved are 4.7×10^{19}, 6.1×10^{20}, and 4.6×10^{21} m^{-3}, respectively. Note that $P_{abs} = Q_{abs} V = \int_V W_{abs}\, dV$ from Eq. (2.27). These figures show that the power absorption occurs only near the inlet of the plasma chamber at a low $f = 1$ GHz, while it tends to occur axially along the plasma-dielectric interfaces as f increases. At a high $f = 23$ GHz, the distribution shows the electromagnetic waves that form a standing surface-wave pattern along the interfaces, where the microwaves penetrate deeply into the plasma chamber.

Figures 2.8(a) and (b) show typical snapshots of the two-dimensional distribution of the axial and radial electric field components E_x and E_r of Fig. 2.7(c), respectively, taken at the time when the electric fields reach the peak values in a microwave period. Corresponding enlarged views of the electric fields in the plasma near the plasma-

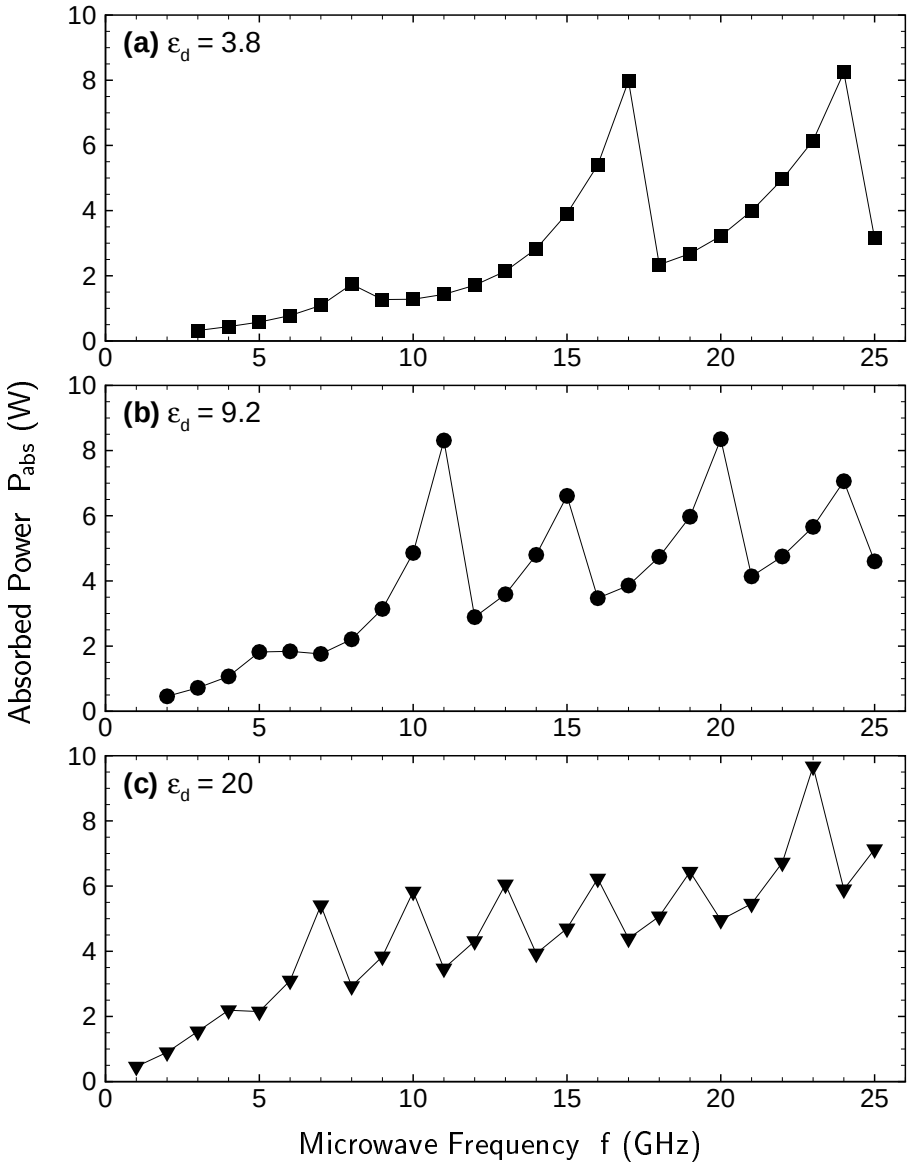

Figure 2.6: Absorbed power P_{abs} in the microplasma as a function of microwave frequency f for different relative permittivities ε_{d} = (a) 3.8, (b) 9.2, and (c) 20 of dielectrics, calculated at a pressure $p = 1.0 \times 10^5$ Pa with a microwave input power $P_{\mathrm{in}} = 10$ W. Note that the power which is not absorbed in the plasma is reflected and leaves the simulation area or the microplasma source.

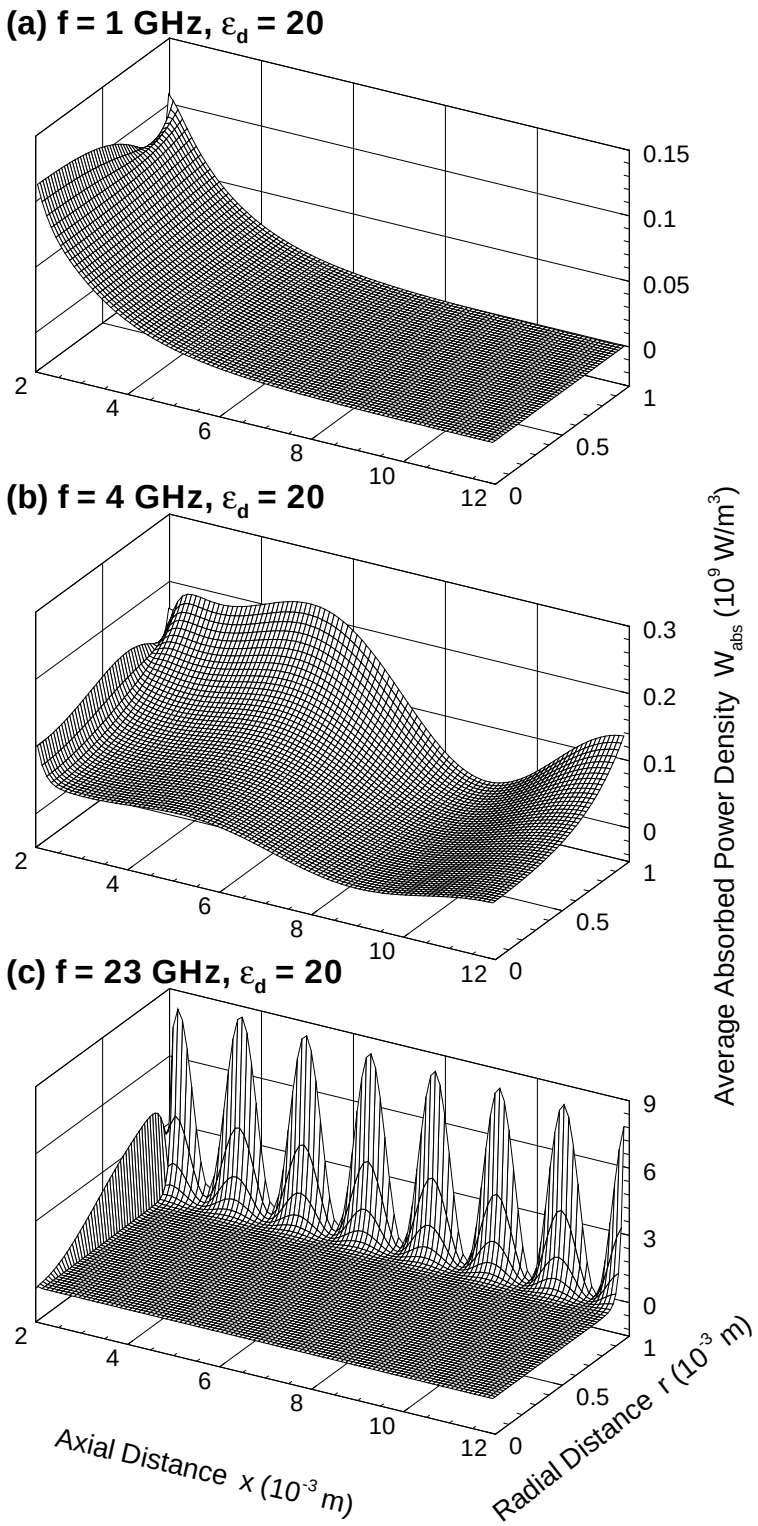

Figure 2.7: Two-dimensional distribution of the time-averaged absorbed power density $W_{\rm abs}$ in the microplasma source for different microwave frequencies f = (a) 1, (b) 4, and (c) 23 GHz with $\varepsilon_{\rm d} = 20$ of dielectrics. The calculation conditions are the same as those of Fig. 2.6(c). Note that $P_{\rm abs} = Q_{\rm abs}V = \int_V W_{\rm abs}\, dV$.

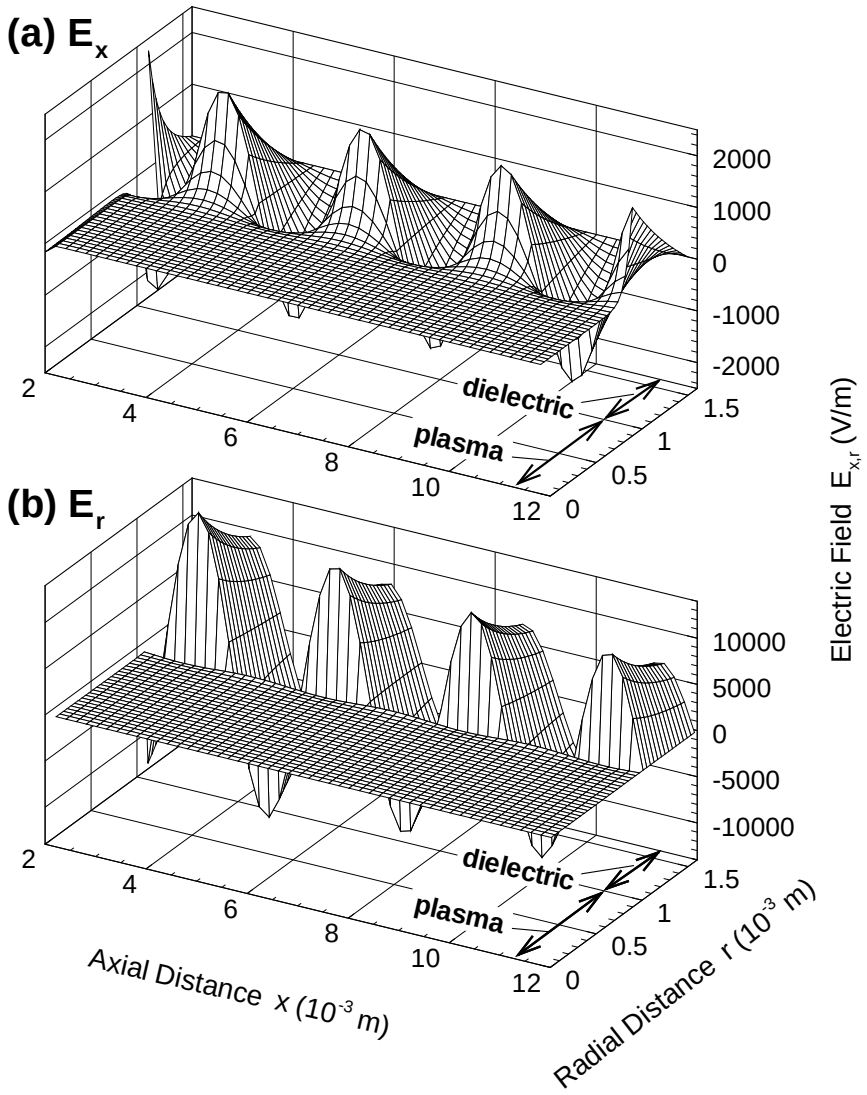

Figure 2.8: Typical snapshots of the two-dimensional distribution of the (a) axial and (b) radial electric field components of E_x and E_r in the plasma chamber, taken at the time when the electric fields reach the peak values in a microwave period. Here the calculation conditions are the same as those of Fig. 2.7(c).

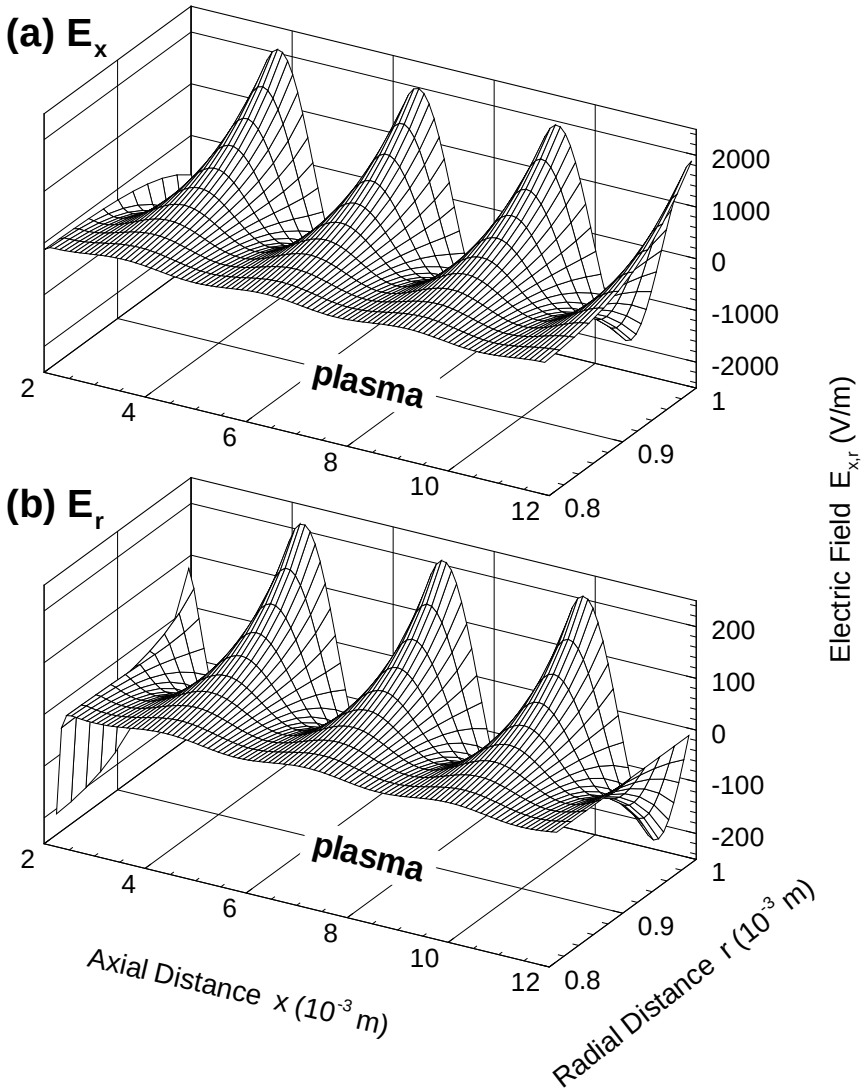

Figure 2.9: Enlarged views of the (a) axial and (b) radial electric fields in the plasma near the plasma-dielectric interfaces of Figs. 2.8(a) and (b), respectively.

dielectric interfaces (between $r = 0.8$ and 1.0 mm) are also shown in Figs. 2.9(a) and (b). These figures indicate that while the strength of E_r is about ten times larger than that of E_x in the dielectric, the former is less than one-tenth of the latter in the plasma. From Figs. 2.7(c) and 2.9 the peak positions of $W_{\rm abs}$ correspond to those of E_x, not E_r. These results infer that E_x is the major component of the electric field that contributes to $P_{\rm abs}$.

2.3.3 Theoretical analysis of the dispersion relation

To investigate the mechanism for the local absorption peaks in Fig. 2.6, we consider the wave propagation along an infinitely long plasma column [radius a, relative permittivity $\varepsilon_{\rm p}$ defined by Eq. (2.38)] inside a dielectric tube (inner radius a, outer radius b, relative permittivity $\varepsilon_{\rm d}$) covered with a metal; then, we derive a theoretical dispersion relation, as discussed in [48, 73, 74]. The adequate boundary conditions [$E_r = B_\theta = 0$ on the axis of symmetry ($r = 0$), E_x and B_θ continuities at the plasma-dielectric interfaces ($r = a$), $E_x = 0$ on the perfectly conducting walls ($r = b$)], give the following dispersion equation similar to equation (11) in Ref. [74]:

$$\frac{\varepsilon_{\rm p}}{k_{\rm p}} \cdot \frac{J_1(k_{\rm p}a)}{J_0(k_{\rm p}a)} = \frac{\varepsilon_{\rm d}}{k_{\rm d}} \cdot \frac{J_1(k_{\rm d}a)H_0^{(1)}(k_{\rm d}b) - J_0(k_{\rm d}b)H_1^{(1)}(k_{\rm d}a)}{J_0(k_{\rm d}a)H_0^{(1)}(k_{\rm d}b) - J_0(k_{\rm d}b)H_0^{(1)}(k_{\rm d}a)}, \tag{2.42}$$

where J_s and $H_s^{(1)}$ ($s = 0, 1$) are the sth-order Bessel and Hankel functions of the first kind, respectively, and $k_i^2 = k_\gamma^2 + \varepsilon_i k_0^2$ (i = p, d) with $k_0 = 2\pi/\lambda_0$ (λ_0: wavelength in vacuum). The complex propagation constant $k_\gamma = k_\alpha + {\rm j}k_\beta$ (k_α: damping rate, k_β: wave number) can be determined from the dispersion equation (2.42), which is a function of $\omega/\omega_{\rm pe}$, $\nu_{\rm e}/\omega$, and k_γ. In the following analysis, fixed parameters are $a =$ 1 mm, $b = 1.6$ mm, and $\varepsilon_{\rm d} = 20$, unless otherwise stated.

To determine k_α and k_β as a function of microwave frequency f, we set the parameters $\omega/\omega_{\rm pe}$ and $\nu_{\rm e}/\omega$ obtained from the absorbed power $P_{\rm abs}$ in Fig. 2.6(c) and the corresponding $n_{\rm e}$ and $T_{\rm e}$ in Fig. 2.5. The results are shown in Fig. 2.10, where the thick solid line represents the wave number k_0 in vacuum, and the dashed line corresponds to the value of 2π divided by 10 mm or the plasma column length. The condition under which k_β exceeds the dashed line indicates that there is at least one wavelength in the plasma chamber. The wave number k_β increases with increasing f, while the damping rate k_α decreases and then slightly increases with f. At $f = 1$ GHz, k_α is almost equal

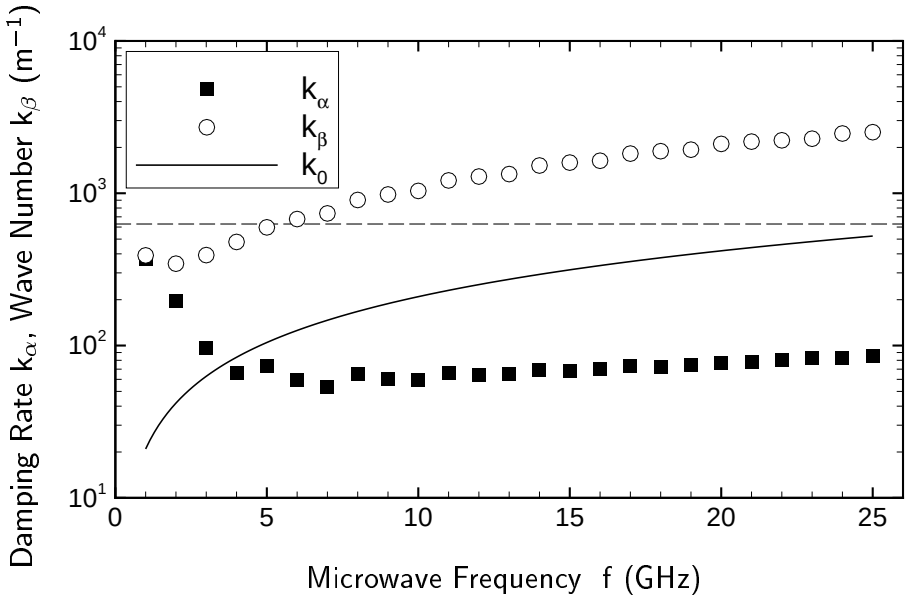

Figure 2.10: Damping rate k_α and wave number k_β as a function of microwave frequency f for $\varepsilon_\mathrm{d} = 20$ of dielectrics, derived from the theoretical dispersion equation with the absorbed power P_abs in Fig. 2.6(c) and the corresponding electron density n_e and temperature T_e in Fig. 2.5. Here, the thick solid line represents the wave number k_0 in vacuum, and the dashed line corresponds to the value of 2π divided by 10 mm or the microplasma column length.

Table 2.1: Relation between the absorbed power $P_{\rm abs}$ and the electromagnetic wavelength λ in the microplasma, for each combination of the microwave frequency f and the relative permittivity $\varepsilon_{\rm d}$ of dielectrics giving the peak absorbed power $P_{\rm abs}$ in Figs. 2.6(a)–(c). Here, the microwave input power was taken to be $P_{\rm in} = 10$ W, and the wavelength λ was derived from the theoretical dispersion relation. The integers n and m are the odd and even multiple numbers of the quarter wavelength $\lambda/4$, respectively. Notice that $\lambda/4 \times n$ falls between 10.3 and 10.6 mm.

$\varepsilon_{\rm d}$	f (GHz)	$P_{\rm abs}$ (W)	λ (mm)	n	$\lambda/4 \times n$ (mm)	m	$\lambda/4 \times m$ (mm)
3.8	17	8.0	8.46	5	10.6	4	8.46
3.8	24	8.2	6.03	7	10.6	6	9.05
9.2	11	8.3	8.34	5	10.4	4	8.34
9.2	15	6.6	6.08	7	10.6	6	9.12
9.2	20	8.3	4.64	9	10.4	8	9.28
9.2	24	7.1	3.84	11	10.6	10	9.60
20	7	5.4	8.52	5	10.6	4	8.52
20	10	5.8	6.06	7	10.6	6	9.10
20	13	6.0	4.70	9	10.6	8	9.40
20	16	6.2	3.84	11	10.6	10	9.61
20	19	6.4	3.25	13	10.6	12	9.75
20	23	9.7	2.75	15	10.3	14	9.63

to k_β, which is consistent with the distribution of $W_{\rm abs}$ in Fig. 2.7(a) showing that the electromagnetic fields are attenuated immediately as the waves enter the plasma chamber.

One might imagine one of the local peaks of $P_{\rm abs}$ at $f = 4$ GHz in Fig. 2.6(c), because of the periodical rises and drops of $P_{\rm abs}$ at higher frequencies. In Fig. 2.10, the cross point of the dashed line and the wave number curve of k_β is located between $f = 5$ and 6 GHz, where the wavelength of microwaves in the plasma is equal to the length of the plasma chamber; correspondingly, the wavelength in the plasma at $f = 4$ GHz is longer than the chamber length as shown in Fig. 2.7(b). Thus, $P_{\rm abs}$ decreases with decreasing f below this frequency without any absorption peaks.

We also derive the relation between the absorbed power $P_{\rm abs}$ and the electromagnetic wavelength $\lambda = 2\pi/k_\beta$ in the plasma with $\varepsilon_{\rm d} = 3.8$ and 9.2 in addition to $\varepsilon_{\rm d} = 20$, for each combination of f and $\varepsilon_{\rm d}$ giving the peak $P_{\rm abs}$ in Figs. 2.6(a)–(c). The results are summarized in Table 2.1, indicating that the quarter wavelength $\lambda/4$ multiplied by some odd numbers n falls between 10.3 and 10.6 mm while even numbers do not give

such relation.

In this analysis, the plasma is assumed to be infinitely long although there are dielectric and metal boundaries of the plasma chamber in the axial direction. Here, the dielectric at the chamber entrance (between $x = 1.4$ and 2.0 mm) particularly makes the analysis complicated because of the abrupt change in the electromagnetic field structure from TEM to TM waves. Thus, it is impossible to directly compare the dispersion relation obtained here with numerical results and then to simply explain the relation between the chamber length and the wavelength. Nonetheless, keeping the length $\lambda/4 \times n$ between the chamber length (10.6 mm) and the plasma length (10 mm) results in the peaks of power absorption, which is probably due to the kind of cavity resonance mechanism, and this would give some indication of how a microplasma sources is to be fabricated.

From these analyses, it is concluded that at least one wavelength is required to occur in the plasma column to effectively absorb the electromagnetic field energy of microwaves, and that the local peaks of the absorbed power are obtained when the quarter wavelength multiplied by some odd numbers is between the chamber length and the plasma length. These arise intrinsically from the matching of microwaves depending on the geometric structure of microplasma sources. In view of the weight, size, and power supply of microspacecraft which are strictly limited, a microplasma source without matching networks is desirable in a microthruster. Therefore, we should carefully choose a combination of the microwave frequency and the relative permittivity of dielectrics under given operational conditions.

Note finally that the plasma parameters are treated in a non-dimensional manner in this study for a design consideration. However, the absorption of the microwave power is localized in the plasma as shown in Fig. 2.7; this would lead to non-uniform density and temperature profiles. Such non-uniform profiles at the sheath region in close proximity to the radial boundary of the plasma column, which is less than a few μm thick in the present study, are especially important because the plasma resonance occurs at $\omega_{\rm pe} = \omega$ resulting in a strong inhomogeneous electron heating [55, 75]. Moreover, filament and microarc formation is a major problem in atmospheric pressure Ar discharges [35, 76, 77]. To consider these problems, a new model at least in two dimensions will have to be developed in future work.

2.4 Micronozzle flow

Flows through small nozzles have been investigated by several authors both numerically and experimentally [70, 78, 79]. Most of these studies were targeted for flows in a cold-gas, resistojet, etc., and thus the flows were treated as a one-temperature model. While a micro-arcjet thruster has recently been presented [20], the flows were not treated as plasmas in the numerical study. The following sections give some results of high-temperature plasma flows through micronozzles, which include the effect of wall boundary conditions. It should be noted that the validity of the numerical solution was checked by comparing the rate of mass inflow across the nozzle inlet plane with that of mass outflow across the exit plane to confirm conservation of mass [63]. For all of the results calculated below, the difference between mass flow rate at the inlet and exit was less than one per cent.

2.4.1 Flow properties

Calculations of the FM module for the micronozzle flow were performed using the inlet condition obtained from the GM module at an absorbed power $P_{\rm abs} = 5.0$ W and a pressure $p = 1.0 \times 10^5$ Pa, giving an electron density $n_{\rm e} = 2.8 \times 10^{21}$ m^{-3}, electron temperature $T_{\rm e} = 8.6 \times 10^3$ K, and heavy particle temperature $T_{\rm h} = 7.4 \times 10^3$ K in the microplasma source. The 20$^{\rm o}$-half-cone-angle nozzle was employed in the simulation. Figures 2.11(a)–(c) show the contour of the Mach number $Ma = |\boldsymbol{v}|(\gamma k_{\rm B} T_{\rm h}/m_{\rm h})^{-1/2}$ [80] in the micronozzle for three wall boundary conditions: adiabatic, radiative, and isothermal walls, respectively. Here, $\gamma = 5/3$ is the specific heat ratio for monatomic gases. Under the adiabatic condition, the boundary layer is very thick, covering the entire flow region inside the micronozzle. The flow is subsonic over the entire cross section at the exit, and the maximum Ma is obtained at the position close to the throat. Under the radiative condition, a thick boundary layer still occurs. However, the supersonic region tends to dominate over the subsonic region at the exit, and the maximum Ma is located near the exit inside the nozzle. Moreover, under the isothermal condition, the boundary layer is relatively thin. The flow seems to expand smoothly, and the maximum Ma is obtained at the nozzle exit, which is the highest among all the nozzle conditions investigated.

Figures 2.12(a)–(c) show the contour of the heavy particle temperature $T_{\rm h}$ in the

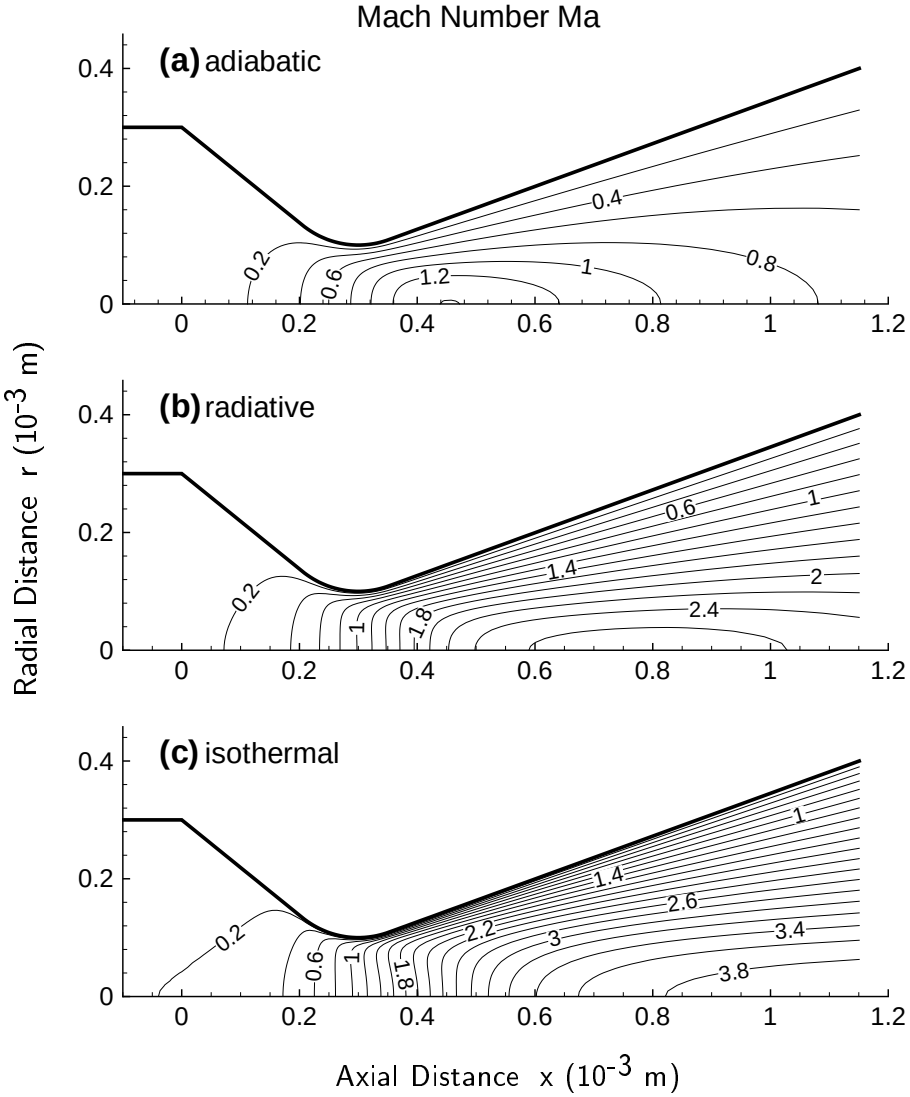

Figure 2.11: Contour of the Mach number *Ma* in the micronozzle for three wall boundary conditions: (a) adiabatic, (b) radiative, and (c) isothermal walls of the 20°-half-cone-angle micronozzle. Here, the inlet conditions are: $p = 1.0 \times 10^5$ Pa, $n_e = 2.8 \times 10^{21}$ m^{-3}, $T_e = 8.6 \times 10^3$ K, and $T_h = 7.4 \times 10^3$ K, calculated at an absorbed power $P_{abs} = 5.0$ W in the microplasma source.

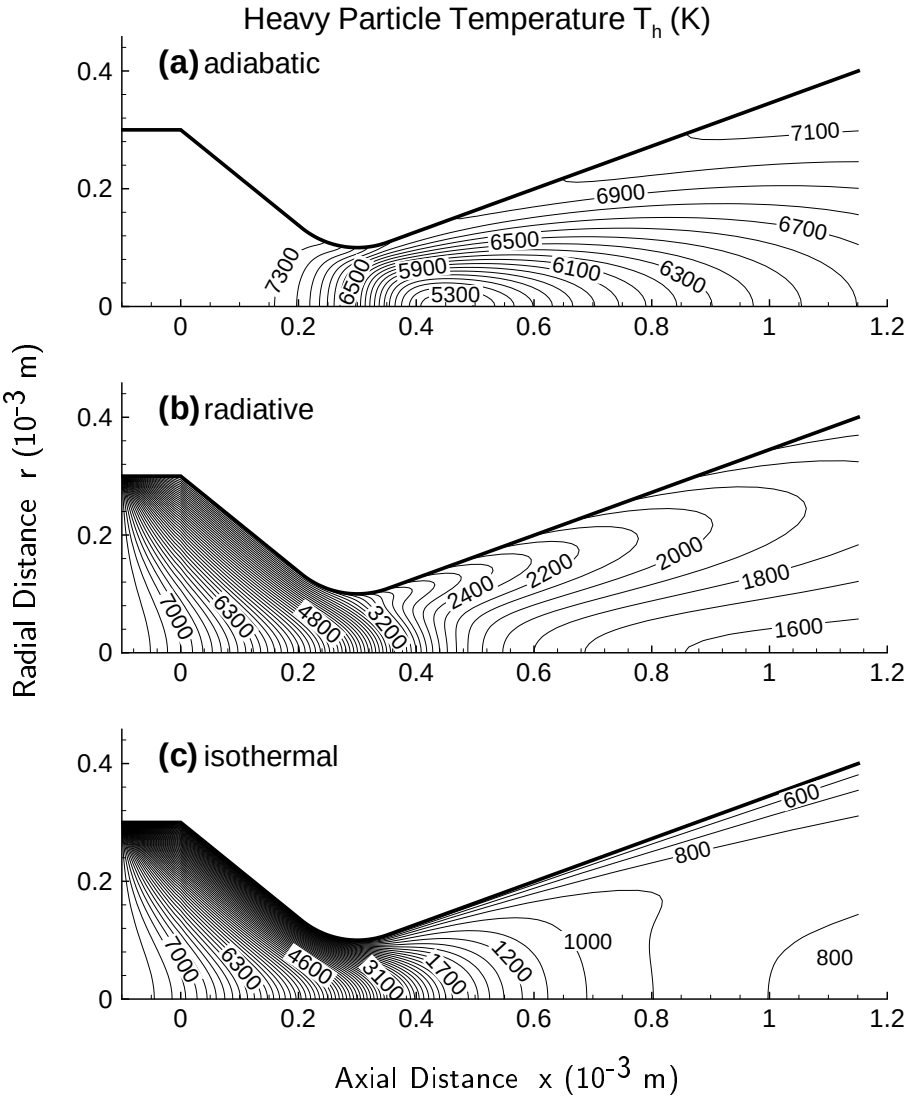

Figure 2.12: Contour of the heavy particle temperature T_h in the micronozzle for three boundary conditions: (a) adiabatic, (b) radiative, and (c) isothermal walls. Other calculation conditions are the same as those in Fig. 2.11.

micronozzle for the three wall boundary conditions. Under the adiabatic condition, temperature T_h is very high even at the exit, being higher near the wall than near the centre axis; these results indicate that high viscous heating occurs in the very thick boundary layer, the effect of which is larger than that of cooling through the flow expansion. The minimum T_h is obtained at the position close to where the maximum *Ma* is obtained in Fig. 2.11(a). This kind of viscous heating was also confirmed in Ref. [70], and its effect observed here is much larger because of higher temperatures of heavy particles at the nozzle inlet as well as smaller dimensions of the micronozzle. Under the radiative condition, the temperature T_h on the axis decreases monotonically in the axial direction, resulting in the minimum T_h at the exit, because of the cooled walls and the flow expansion. However, owing to a thick boundary layer as in Fig. 2.11(b), viscous heating also occurs between the wall and axis where the cooling effect is reduced. Moreover, under the isothermal condition, the temperature T_h decreases significantly through the throat because of the enhanced cooling of walls and the flow expansion, leading to the minimum T_h at the nozzle exit which is the lowest among all the nozzle conditions investigated.

Figures 2.13(a)–(c) show the contour of the electron temperature T_e in the micronozzle for the three wall boundary conditions. The distribution of T_e is significantly different from that of T_h, while showing the similar behavior among the three conditions, because the viscous dissipation is not included in the electron energy equation (2.19). The heavy particle temperature T_h at the nozzle exit is lowered in order of the adiabatic, radiative, and isothermal walls. This tendency is also observed for T_e, showing a difference of about 1.0×10^3 K at the exit among the three. Note that the distribution of other properties such as n_e did not show a distinct difference among the three wall conditions.

It is concluded that the wall boundary conditions have a large effect on the thickness of boundary layers associated with viscosity, and thus on flow properties in the micronozzle. In practice, the viscosity is a function of T_h, becoming larger as T_h increases; the increase in viscosity, in turn, leads to high viscous dissipation, and thus to much higher T_h. Hence, in the micronozzle, the thickness of boundary layers tends to be thick, being comparable to the nozzle radius, under conditions where the nozzle walls retain viscous heat inside the nozzle. In effect, there is no energy loss through the wall under the adiabatic wall condition, which in turn leads to a high viscous energy

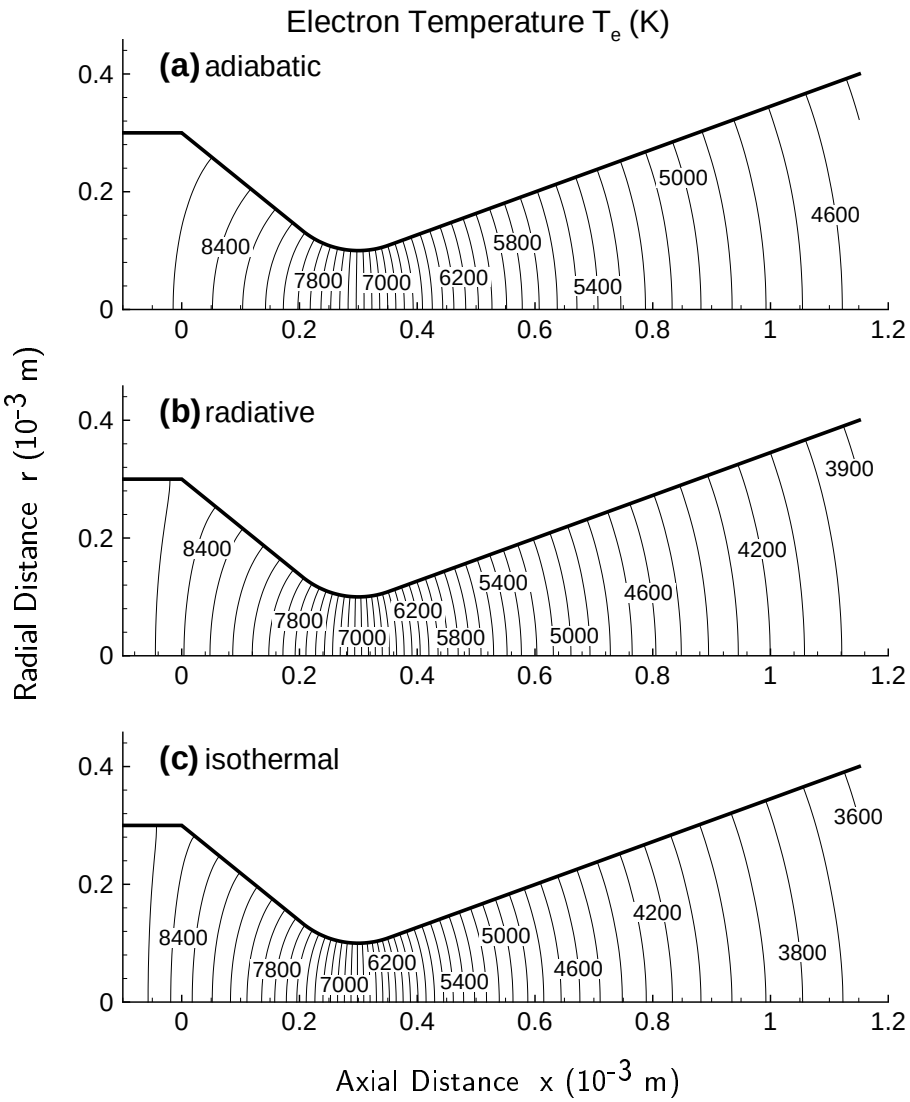

Figure 2.13: Contour of the electron temperature T_e in the micronozzle for three boundary conditions: (a) adiabatic, (b) radiative, and (c) isothermal walls. Other calculation conditions are the same as those in Fig. 2.11.

loss or a high viscous heating in the thick boundary layer of micronozzle flows.

2.4.2 Thrust performance

We have discussed the micronozzle flow properties for three different wall conditions with a fixed pressure at the nozzle inlet. Then, we will discuss the thrust performance under the radiative wall condition with a fixed mass flow rate $\dot{m} = 2.0$ mg/s, because the mass flow rate is a practically controllable parameter compared to the chamber pressure for thrusters in space; moreover, the actual wall condition is considered close to radiative walls, lying between adiabatic and isothermal wall conditions.

To fix the mass flow rate, we have to modify the inlet boundary conditions. Since the flow is subsonic at the nozzle inlet, all the flow properties are impossible to fix simultaneously, and thus at least one of them is extrapolated from the interior points [50]. We first obtain the density ρ by dividing the mass flow rate $\dot{m}$ by the axial velocity at the inlet. The density is then given to the GM module, which provides the electron density n_e, electron temperature T_e, and heavy particle temperature T_h at a given absorbed power P_abs. These variables are used as new inlet conditions in the FM module, and then a new axial velocity is obtained from the extrapolation. Once the axial velocity is determined, we obtain the density in the same way. The calculation cycle is repeated until the variables reach a steady state. Note that the pressure p at the inlet is dependent on $\dot{m}$ and P_abs in this case.

As discussed in the preceding section, the flow inside the micronozzle does not expand sufficiently even at the exit owing to highly viscous flows therein. Thus, to take into account the pressure effect on the thrust performance, we employ two types of the thrust defined at the nozzle exit:

$$F_\mathrm{t} = 2\pi \int_0^{r_\mathrm{ex}} (\rho u^2 + p)\, r dr, \tag{2.43}$$

$$F'_\mathrm{t} = 2\pi \int_0^{r_\mathrm{ex}} \rho u^2\, r dr, \tag{2.44}$$

where r_ex and u are the radius of the nozzle exit and the velocity in the axial direction, respectively. Note that F_t consists of the momentum and pressure thrust, whereas F'_t is the momentum thrust only. The specific impulse I_sp and I'_sp are derived from the thrust F_t and F'_t, respectively, being divided by the product of the mass flow rate and

the gravitational constant g; e.g.,

$$I_{\rm sp} = F_{\rm t} \left(g\, 2\pi \int_0^{r_{\rm ex}} \rho u\, r dr \right)^{-1}. \tag{2.45}$$

Figure 2.14(a) shows the thrust $F_{\rm t}$, $F'_{\rm t}$ and specific impulse $I_{\rm sp}$, $I'_{\rm sp}$ as a function of absorbed power $P_{\rm abs}$ in the microplasma source for the 20°-half-cone-angle micronozzle with a mass flow rate $\dot{m} = 2.0$ mg/s. As $P_{\rm abs}$ increases, the thrust performance ($F_{\rm t}$, $I_{\rm sp}$, $F'_{\rm t}$, $I'_{\rm sp}$) increases and then tends to saturate, being attributed to reduced increasing rates of p and $T_{\rm h}$ at higher $P_{\rm abs}$ as shown in Fig. 2.14(b). In addition, the increasing rates of $F'_{\rm t}$ and $I'_{\rm sp}$ appear to be slightly small, compared to those of $F_{\rm t}$ and $I_{\rm sp}$, implying that the pressure thrust is larger at higher $P_{\rm abs}$, or the flow inside the nozzle does not fully expand even at the exit.

Figures 2.15(a)–(c) show the contour of the Mach number Ma in the micronozzle for different absorbed powers $P_{\rm abs} = 1.3$, 5.0, and 9.7 W in Fig. 2.14, and the corresponding contours of the heavy particle temperature $T_{\rm h}$ are also shown in figures 2.16(a)–(c). The maximum Ma decreases with increasing $P_{\rm abs}$, the position of which moves from the exit to inside the nozzle close to the throat; the boundary layer thickness in the micronozzle becomes larger at higher $P_{\rm abs}$ as clearly seen in Fig. 2.16, where a smaller core of expanding flows is observed near the exit at higher $P_{\rm abs}$. These results imply that at higher $P_{\rm abs}$, the thermal energy obtained in the microplasma source is not effectively converted into kinetic energy through the micronozzle, owing to a high viscous loss or heating in the thick boundary layer; this leads to an increase in $T_{\rm h}$ and thus pressure p, so that the pressure thrust attains larger fractions of the total thrust at higher $P_{\rm abs}$ as in Fig. 2.14(a).

Figure 2.17 shows the thrust $F_{\rm t}$, $F'_{\rm t}$ and specific impulse $I_{\rm sp}$, $I'_{\rm sp}$ as a function of half-cone angle of the micronozzle shown in Fig. 2.3, at an absorbed power $P_{\rm abs} = 5.0$ W in the microplasma source. The thrust performance increases with increasing angle, and the increasing rates of $F'_{\rm t}$ and $I'_{\rm sp}$ are relatively large compared to those of $F_{\rm t}$ and $I_{\rm sp}$ in contrast to the power dependence shown in Fig. 2.14. This implies that the pressure thrust dominates for a micronozzle of smaller half-cone angles.

Figures 2.18(a)–(c) show the contour of the Mach number Ma in the micronozzle for different half-cone angles of 10°, 20°, and 30° in Fig. 2.17, and the corresponding contours of the heavy particle temperature $T_{\rm h}$ are also shown in Figs. 2.19(a)–(c). A significant increase in the maximum Ma is obtained as the angle is increased, while

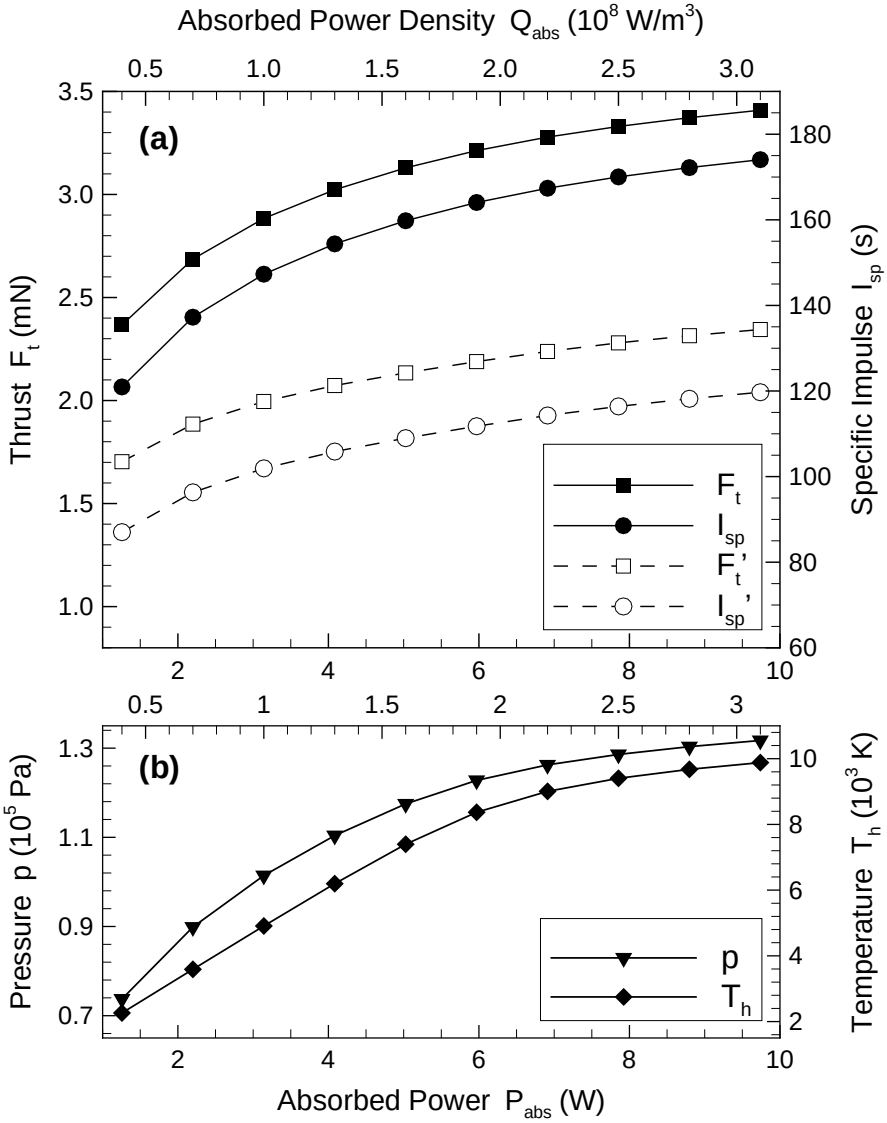

Figure 2.14: (a) Thrust F_t, F_t' and specific impulse I_sp, I_sp' as a function of absorbed power P_abs in the microplasma source, calculated with a mass flow rate $\dot{m} = 2.0$ mg/s under radiative wall conditions of the 20°-half-cone-angle micronozzle. Here, F_t' and I_sp' are the component of momentum thrust only. Also shown are the (b) pressure p and heavy particle temperature T_h at the nozzle inlet in this situation.

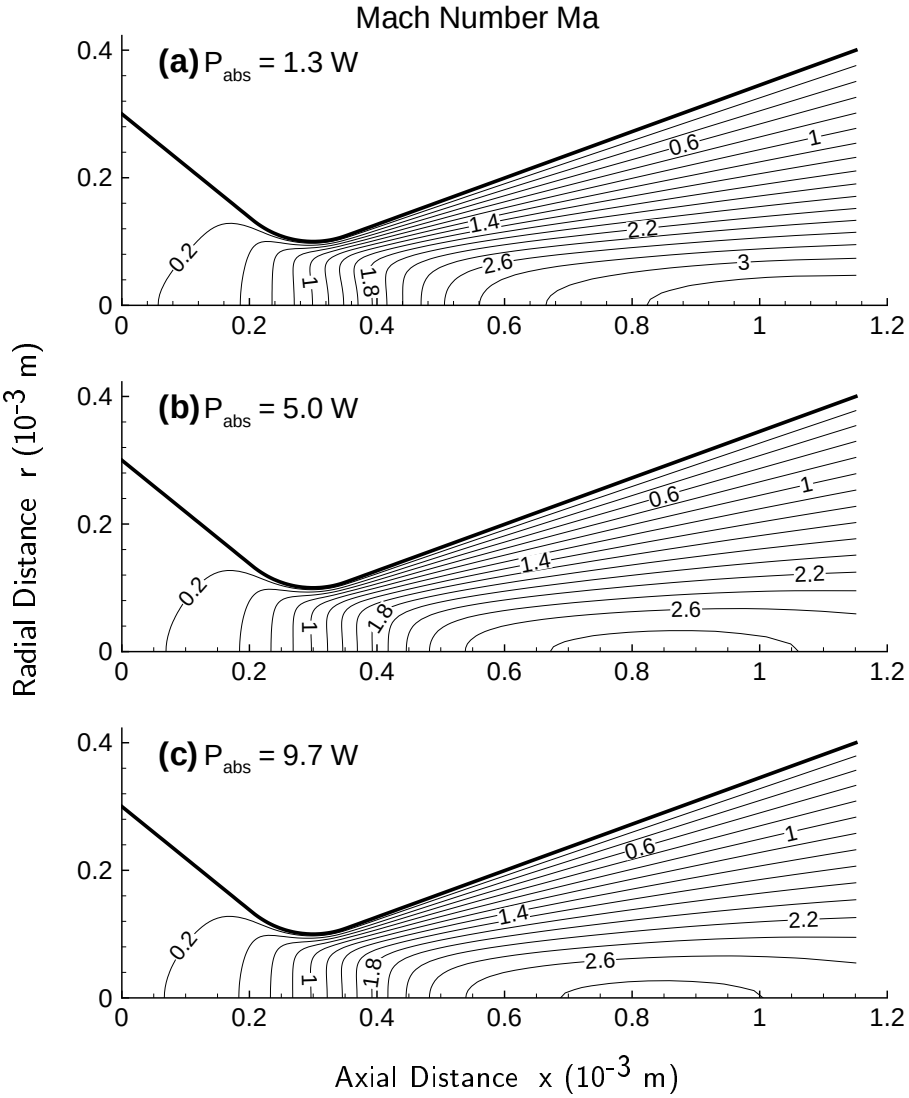

Figure 2.15: Contour of the Mach number Ma in the micronozzle for different absorbed powers P_{abs} = (a) 1.3, (b) 5.0, and (c) 9.7 W in Fig. 2.14.

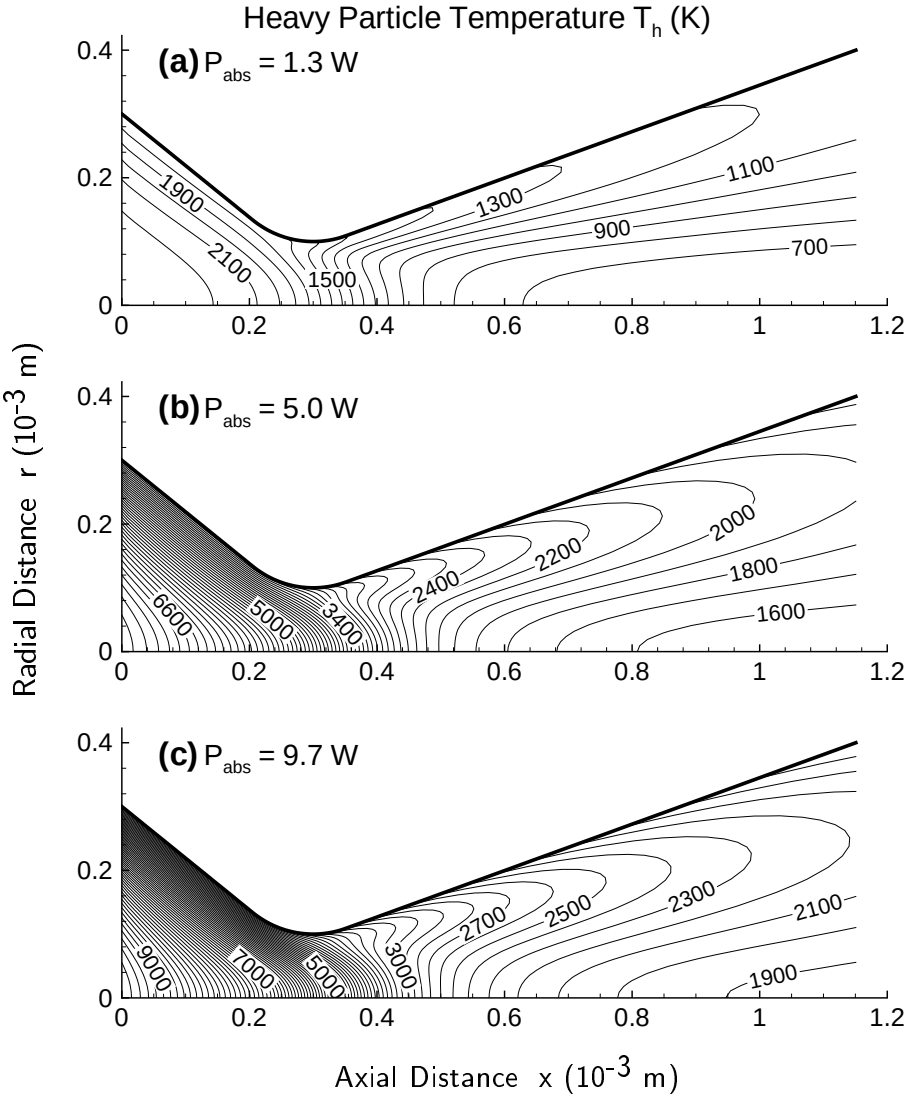

Figure 2.16: Contour of the heavy particle temperature T_h in the micronozzle for different absorbed powers P_abs = (a) 1.3, (b) 5.0, and (c) 9.7 W in Fig. 2.14.

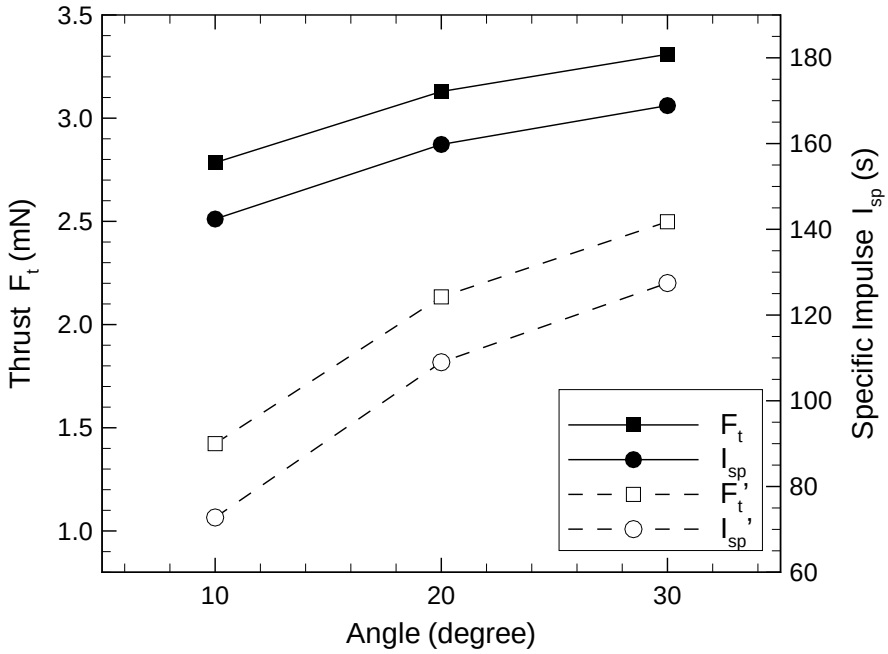

Figure 2.17: Thrust F_t, F_t' and specific impulse I_sp, I_sp' as a function of half-cone angle of the micronozzle shown in Fig. 2.3, calculated at an absorbed power $P_\mathrm{abs} = 5.0$ W in the microplasma source with a mass flow rate $\dot{m} = 2.0$ mg/s under radiative wall conditions of the micronozzle.

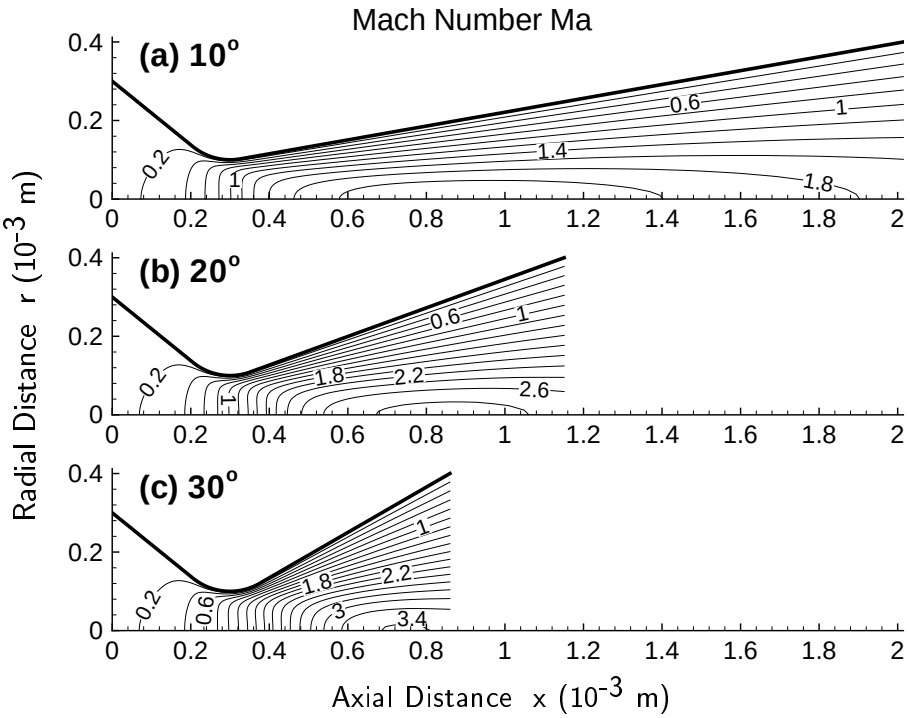

Figure 2.18: Contour of the Mach number *Ma* in the micronozzle for different half-cone angles of (a) 10°, (b) 20°, and (c) 30° in Fig. 2.17.

its position seems to be independent of the angle; in practice, the position is around $x \approx 1.0$ mm for 10° and $x \approx 0.8$ mm for 30°. Since the smaller angle has a longer nozzle length, the flow for the angle of 10° is heavily affected by boundary layers, and the entire region near the nozzle exit is covered with highly viscous flows. These results imply that in the micronozzle, the viscous loss in the boundary layer is much larger than the divergence loss of the nozzle flow.

It is generally appreciated that for nozzle flows, a large half-cone angle leads to a high divergence loss because of large radial velocity components at the nozzle exit and there is relatively small viscous loss owing to thin boundary layers [81]. For micronozzle flows, larger radial velocity components are also obtained with increasing half-cone angle, as shown in Fig. 2.20, which is the radial distribution of the axial velocity u and radial velocity v at the nozzle exit. However, the axial velocity becomes larger with increasing angle, and the difference of u between 10° and 30° is much larger than that of v. Thus, increasing the half-cone angle by shortening the nozzle length significantly contributes to improvement in the thrust performance. While this effect was not clearly

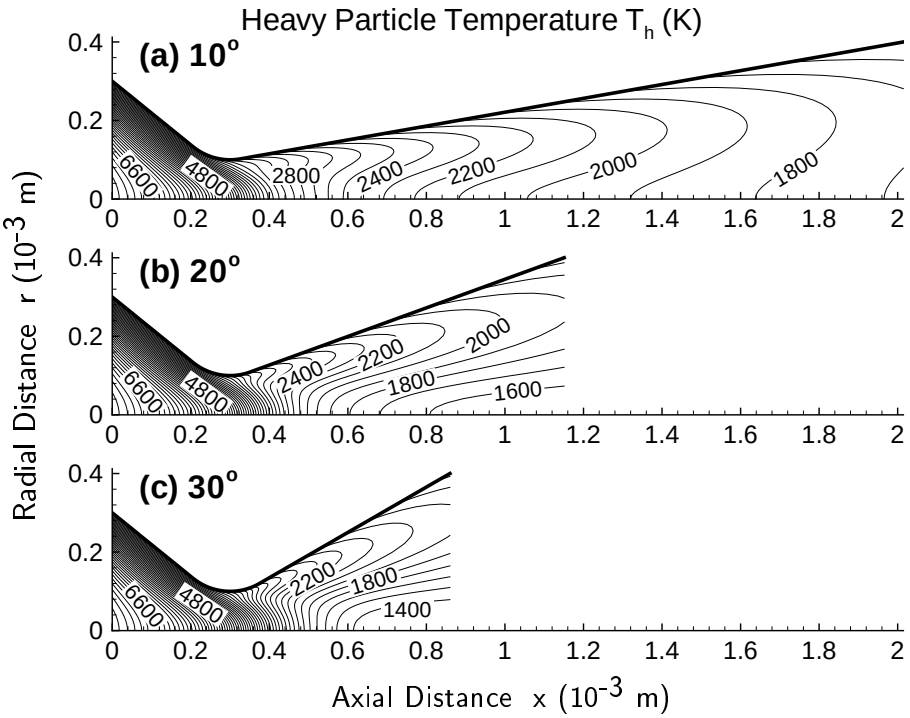

Figure 2.19: Contour of the heavy particle temperature T_h in the micronozzle for different half-cone angles of (a) 10°, (b) 20°, and (c) 30° in Fig. 2.17.

seen in Ref. [70] because of the relatively large dimension of the nozzle, similar results have recently been obtained experimentally in Ref. [20], where the dimension of the micronozzle is almost the same as that discussed here. It is then clear that the thrust performance of the microplasma thruster strongly depends on nozzle geometry.

It is concluded from these analyses that to improve the thrust performance of interest, it is better to employ a large-divergence, short-length nozzle than to provide as much power as possible, because the viscous loss is significant in the micronozzle flow. Regarding the thrust and specific impulse shown in Figs. 2.14(a) and 2.17, the thruster presented here provides a thrust of 2.5–3.5 mN and a specific impulse of 130–180 s in the power range of interest. This implies that the present microplasma thruster is much better than a cold gas thruster and could be used for a station-keeping maneuver of microspacecraft [2].

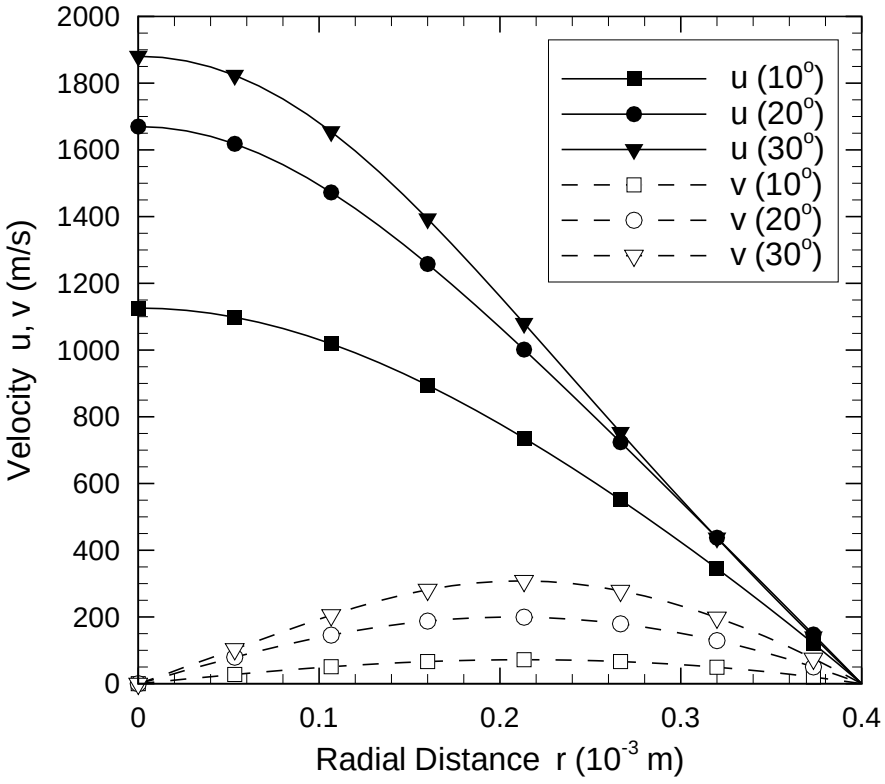

Figure 2.20: Radial distribution of the axial velocity u and radial velocity v at the nozzle exit, for different half-cone angles of (a) 10°, (b) 20°, and (c) 30° in Fig. 2.17.

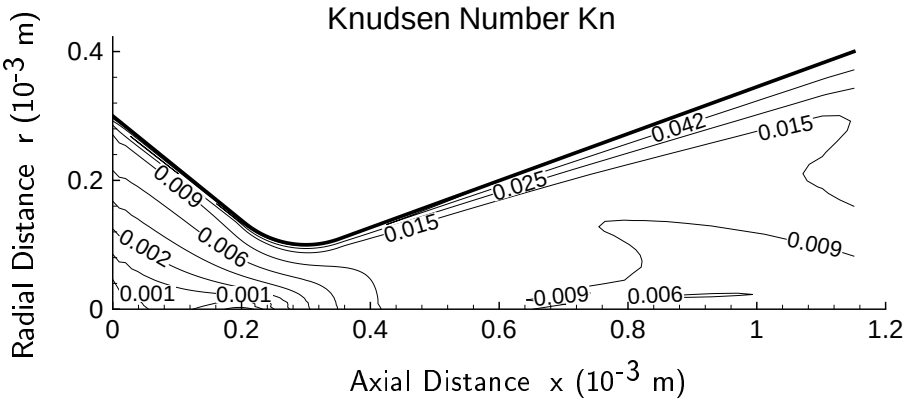

Figure 2.21: Distribution of the Knudsen number Kn in the micronozzle under isothermal wall conditions of the 20°-half-cone-angle micronozzle, calculated at an absorbed power $P_{\rm abs} = 5.0$ W and a pressure $p = 1.0 \times 10^5$ Pa in the microplasma source. Here, the inlet conditions are the same as those in Fig. 2.11.

Table 2.2: Thrust F_t, F'_t and specific impulse I_sp, I'_sp of the isothermal-wall, 20°-half-cone-angle micronozzle for three wall boundary conditions: non-slip, and slip with a tangential-momentum-accommodation coefficient of $\sigma_\mathrm{v} = 0.8$ and 0.2. These were calculated at an absorbed power $P_\mathrm{abs} = 5.0$ W and a pressure $p = 1.0 \times 10^5$ Pa in the microplasma source.

Condition	F_t (mN)	I_sp (s)	F'_t (mN)	I'_sp (s)
Non-slip	3.3	130	2.7	110
$\sigma_\mathrm{v} = 0.8$	3.2	130	2.8	110
$\sigma_\mathrm{v} = 0.2$	3.9	160	3.7	150

2.4.3 Rarefaction

Miniaturizing the nozzle poses a problem of flow rarefaction. The degree of rarefaction is usually expressed by the Knudsen number: $Kn = l/L$, where l is the mean free path and L is the characteristic length of the flow [82, 83]. Figure 2.21 shows a typical example of the distribution of Kn in the micronozzle under isothermal wall conditions of the 20°-half-cone-angle micronozzle, calculated at an absorbed power $P_\mathrm{abs} = 5.0$ W and a pressure $p = 1.0 \times 10^5$ Pa in the microplasma source. Here, the other inlet conditions are the same as those in Fig. 2.11. As in the figure, the Knudsen number is in the range of $10^{-3} \leq Kn < 10^{-1}$, and so we may use the Navier-Stokes equations with slip boundary conditions [82].

To investigate a slip-flow effect on the thrust performance, we employ the following simple slip condition for isothermal walls without a jump in the temperature on the nozzle walls [82]:

$$u_\mathrm{w} = \frac{2 - \sigma_\mathrm{v}}{\sigma_\mathrm{v}}\, l \left.\frac{\partial u}{\partial n}\right|_\mathrm{w}, \tag{2.46}$$

where u_w is the tangential velocity component on the walls, $\partial/\partial n$ is the derivative normal to the walls, and the tangential-momentum-accommodation coefficient σ_v is defined as the fraction of molecules reflected diffusively. The coefficient σ_v is determined experimentally to be between 0.2 and 0.8; the lower limit is for exceptionally smooth surfaces, while the upper limit is typical of most practical surfaces.

Table 2.2 lists the thrust performance (F_t, I_sp, F'_t, I'_sp) of the isothermal-wall, 20°-half-cone-angle micronozzle for three different boundary conditions, calculated at an absorbed power $P_\mathrm{abs} = 5.0$ W and a pressure $p = 1.0 \times 10^5$ Pa in the microplasma source: non-slip, and slip with $\sigma_\mathrm{v} = 0.8$ and 0.2. The respective contours of Mach

number *Ma* in the micronozzle are shown in Figs. 2.22(a)–(c). The thrust performance with non-slip conditions is found to be almost the same as that with slip conditions of $\sigma_v = 0.8$, which is consistent with the fact that little difference in the *Ma* distribution is demonstrated in Figs. 2.22(a) and (b). On the other hand, Fig. 2.22(c) shows a significant difference of the *Ma* distribution compared to the other conditions, because the large tangential velocity due to the slip condition of $\sigma_v = 0.2$ contributes to the flow expansion with less viscous loss in the boundary layer. While the thrust performance is improved using the nozzle with exceptionally smooth surfaces as can be seen in Table 2.2, the nozzle walls have most practical surfaces in practice. It is further noted that the distribution of other flow properties except the axial and radial velocity showed little difference among the different slip conditions of the micronozzle wall. Thus, we can conclude that the calculations conducted here with non-slip conditions are enough for estimation of the thrust performance because the rarefaction has almost no effect on the results obtained.

2.5 Conclusions

A miniature electrothermal thruster using azimuthally symmetric microwave-excited microplasmas has been numerically investigated for design consideration. The microthruster consists of a microplasma source and a micronozzle. The microplasma source is made of a dielectric chamber 1 mm in radius and 10 mm long covered with a metal grounded, producing high temperature plasmas through microwave power input in Ar at around atmospheric pressures. The micronozzle has a throat 0.2 mm in diameter, converting high thermal energy of the plasma into directional kinetic energy of supersonic flows to obtain the thrust required. The numerical model developed consists of three modules: a volume-averaged global model for microplasmas, an electromagnetic model for microwaves based on the finite difference time-domain approximation, and a two-temperature fluid model for micronozzle flows. The simulation is conducted separately for the plasma source and for the nozzle flow.

The microplasma source analysis has been made for three relative permittivities $\varepsilon_d = 3.8$, 9.2, and 20 of dielectrics at a microwave input power of ≤ 10 W in the frequency range from $f = 1$ to 25 GHz. The numerical results indicate that the microwave power absorbed in plasmas increases with increasing frequency f and relative permittivity ε_d,

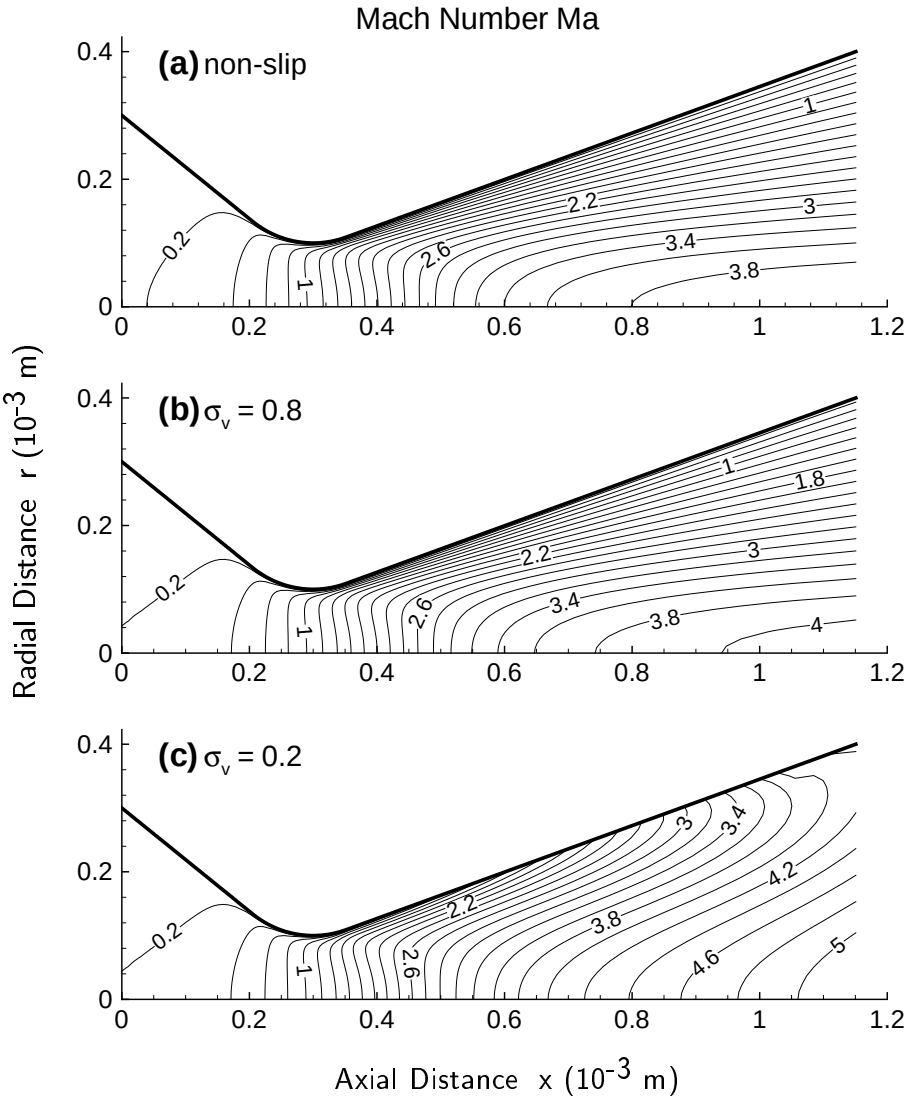

Figure 2.22: Contour of the Mach number *Ma* in the micronozzle for three wall boundary conditions: (a) non-slip, and slip with a tangential-momentum-accommodation coefficient of $\sigma_{\mathrm{v}} =$ (b) 0.8 and (c) 0.2. The situation corresponds to the calculation in Table 2.2.

to achieve the plasma density in the range 2.7×10^{19}–1.7×10^{22} m^{-3}, electron temperature in the range 7.9×10^{3}–1.0×10^{4} K, and heavy particle temperature in the range 9.5×10^{2}–1.0×10^{4} K; in practice, surface waves tend to be established in the microplasma source at higher frequencies and permittivities. Note that a certain combination of the frequency and permittivity significantly enhances the power absorption, exhibiting local peaks where almost all microwave input powers are absorbed in the plasma, owing to the matching of microwaves depending on the geometric structure of microplasma sources. A comparison with the theoretical dispersion relation indicates that to absorb the microwave power effectively, at least one wavelength is required to occur in the plasma chamber; the absorbed power reaches local peaks, as long as the quarter wavelength multiplied by some odd numbers is between the chamber length and the plasma length of interest.

The micronozzle flow analysis has been made to investigate the effects of wall conditions (adiabatic, radiative, and isothermal), the thrust performance depending on the power absorbed in the plasma and on the nozzle half-cone angles, and also the effects of flow rarefaction. The numerical results indicate that the micronozzle flow is very lossy because of high viscosity in thick boundary layers, resulting in the deceleration of supersonic flows in the diverging section of the nozzle; the effect is less significant under wall conditions in order of adiabatic, radiative, and isothermal, or in order of decreasing wall and flow temperatures. It is found to be better to make a short length nozzle by increasing the half-cone angle than to provide as much power as possible, to suppress the effects of viscous loss and thus to enhance the thrust. The thrust performances calculated assuming a mass flow rate of 2.0 mg/s are: a thrust of 2.5–3.5 mN and a specific impulse of 130–180 s for a microwave power of interest (< 10 W), which is applicable to a station-keeping maneuver for microspacecraft less than 10 kg. The numerical results also demonstrates that the flow rarefaction has little effect on the thrust performance of the micronozzle with practical surfaces.

Further studies should be done to fabricate a microplasma source and a micronozzle based on the present simulations. Diagnostics of the microplasma source and micronozzle flow together with measurements of the thrust performance are described in the following chapters.

3

Fabrication of a microplasma source

3.1 Introductory remarks

The numerical model developed in Chap. 2 has predicted that the microplasma thruster proposed could produce adequate thrust performances. In this chapter, we have fabricated only a microplasma source based on the concept design shown in Fig. 2.1 as a preliminary experiment, observing plasma discharges and their emission spectra by means of optical emission spectroscopy (OES). Some results are shown in the following sections.

3.2 Experimental setup

A schematic diagram of the experimental setup and a cross-sectional view of the microplasma source are shown in Fig. 3.1. A commercially available Synthesized RF Signal Generator, 9 kHz - 4000 MHz (Agilent Technologies, 8648D) is employed as a 4-GHz microwave oscillator. Microwaves, amplified with a specially fabricated 4-stage semiconductor amplifier (Micro Denshi, MRF-4G-2), are injected through a semi-rigid type coaxial cable (RG-405/U) into the plasma source. Here, the reflection of the microwave power is suppressed by adjusting the cable length. The plasma source, connected to the stainless-steel pipe through which the working medium, Ar is introduced, is inserted into a stainless-steal chamber with 40 cm in diameter and 40 cm in

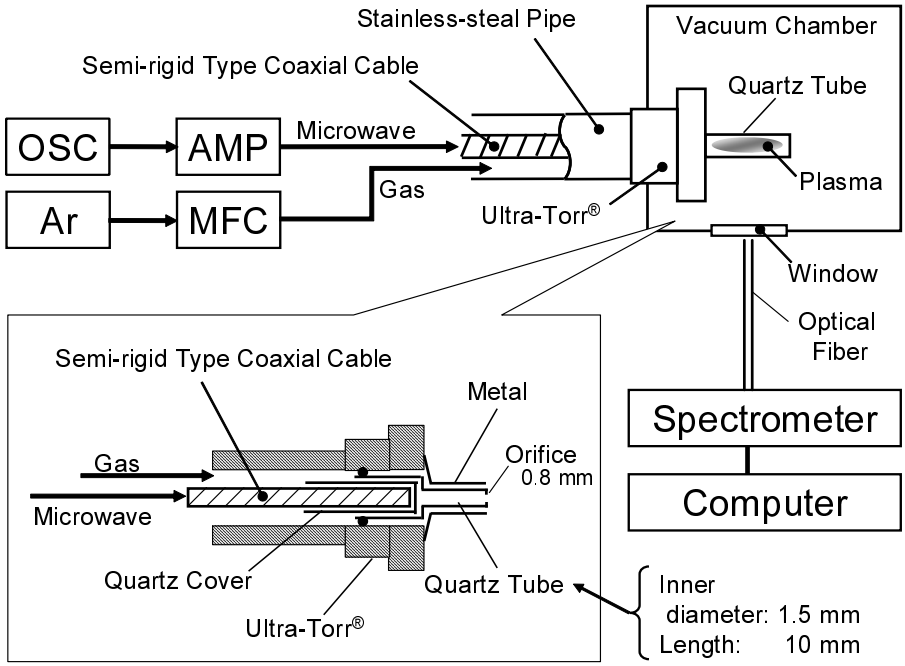

Figure 3.1: A schematic diagram of the experimental setup and a cross-sectional view of the microplasma source (shown in the box). The abbreviations, OSC, AMP, and MFC, represent an oscillator, amplifier, and mass flow controller, respectively.

height, which is evacuated by a mechanical booster dry pump. The stainless-steal pipe is equipped with a Bourdon tube pressure gauge upstream of the plasma chamber to measure the feed gas pressure, which is assumed to be the pressure inside the plasma source. Another gauge with the vacuum chamber measures the ambient pressure of the plasmas source.

The plasma source is composed of a microwave cable and a plasma chamber. The end of the cable is covered with quartz to protect the electrodes from erosion by plasmas. The chamber is made of a straight quartz tube 10 mm in length and 1.5 mm in inner diameter. The one end of the tube is pinched and has an orifice of 0.8 mm in diameter at the exit to vacuum, and the other end is weld to another quartz tube 6.3 mm in outer diameter, inserted into a stainless steel Ultra-Torr vacuum fitting (Swagelok, SS-4-UT-A-6BT, 1/4 in. tube outer diameter). The orifice structure results in a small conductance to keep the pressure inside the plasma chamber much higher than that in the vacuum chamber without a micronozzle. The outside of the quartz tube is covered with metallic mesh instead of metallic pipe for the observation of Ar plasma emission. The emission intensities are measured with a spectrometer

(Ocean Optics, HR2000CG-UV-NIR) through a quartz optical fiber, the head of which is directly positioned in front of the window of the vacuum chamber without a lens.

3.3 Results and discussion

Figure 3.2 shows the emission spectra and photograph images of Ar plasma discharges at the total microwave power P_t of (a) 6 W and (b) 10 W, where the microwave frequency was 4 GHz, the Ar gas flow rate was 100 sccm, the feed pressure was 10 kPa, and the ambient pressure was 16 Pa. Note that the power P_t is not the net absorbed power in plasmas, but the incident power from the amplifier. The plasma was not found to self-ignite in the current setup, and therefore the plasma was generated with the help of an igniter. As shown in the figure, the plasma was maintained only inside the quartz tube at $P_t = 6$ W, while the plasma was blown out to the chamber as a free jet at $P_t = 10$ W. The color of the plasma was dim and purplish red at 6 W, whereas it became bright and whitish pink at 10 W; the emission intensities show this difference. When we focus on the strongest emission line, 763.5 nm ($1s_5$-$2p_6$ transition), and the second strongest, 811.5 nm ($1s_5$-$2p_9$ transition), the ratio of the two spectra intensities I differs slightly ($I_{763.5}/I_{811.5} = 1.47$ at $P_t = 6$ W, $I_{763.5}/I_{811.5} = 1.13$ at $P_t = 10$ W), reflecting the change in the state of the plasma. This change suddenly occurred as P_t increased. Once the shift happened, the increase in emission intensities was imperceptible despite the power rise.

Figure 3.3 shows the dependence of emission intensities of Ar I line (811.5 nm) (a) and of reflective coefficients (b) on the total microwave power P_t, where the other experimental conditions were the same as those in Fig. 3.2, and the reflective coefficient was defined as the ratio of the reflective power to the total microwave power. The figure shows that, with increase in P_t, the Ar I line intensity increases slightly, rises sharply at $P_t = 9$ W, and then increases gradually again. As P_t decreases, the intensity decreases and then drops steeply at $P_t = 6.5$ W. The reflective coefficient drops or rises drastically at the same power where the significant change of intensity occurs. These results were found to be reproducible, implying that a mode change occurred at incident powers between 6 W and 10 W.

The mechanism of this intensity transition would be due to the difference of the way microwaves propagate in the plasma. In the low-intensity mode, microwaves were

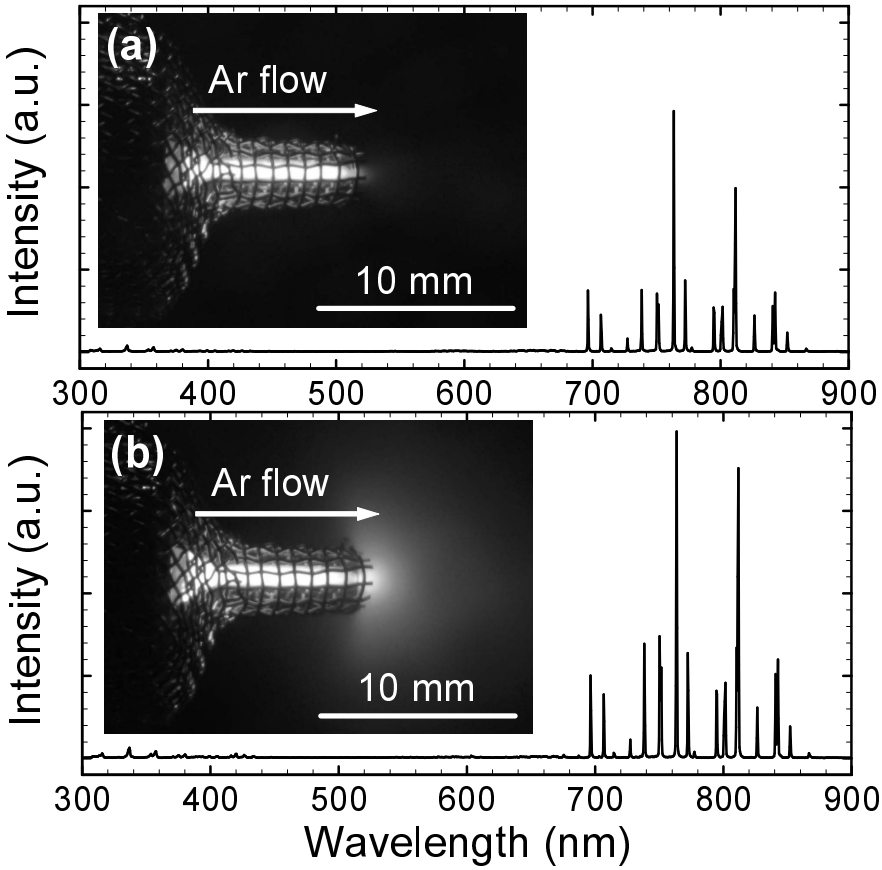

Figure 3.2: Emission spectra and photograph images of Ar plasma discharges at the total microwave power P_t of (a) 6 W and (b) 10 W. Microwave frequency $f = 4$ GHz, Ar gas flow rate = 100 sccm, feed gas pressure = 10 kPa, ambient pressure = 16 Pa.

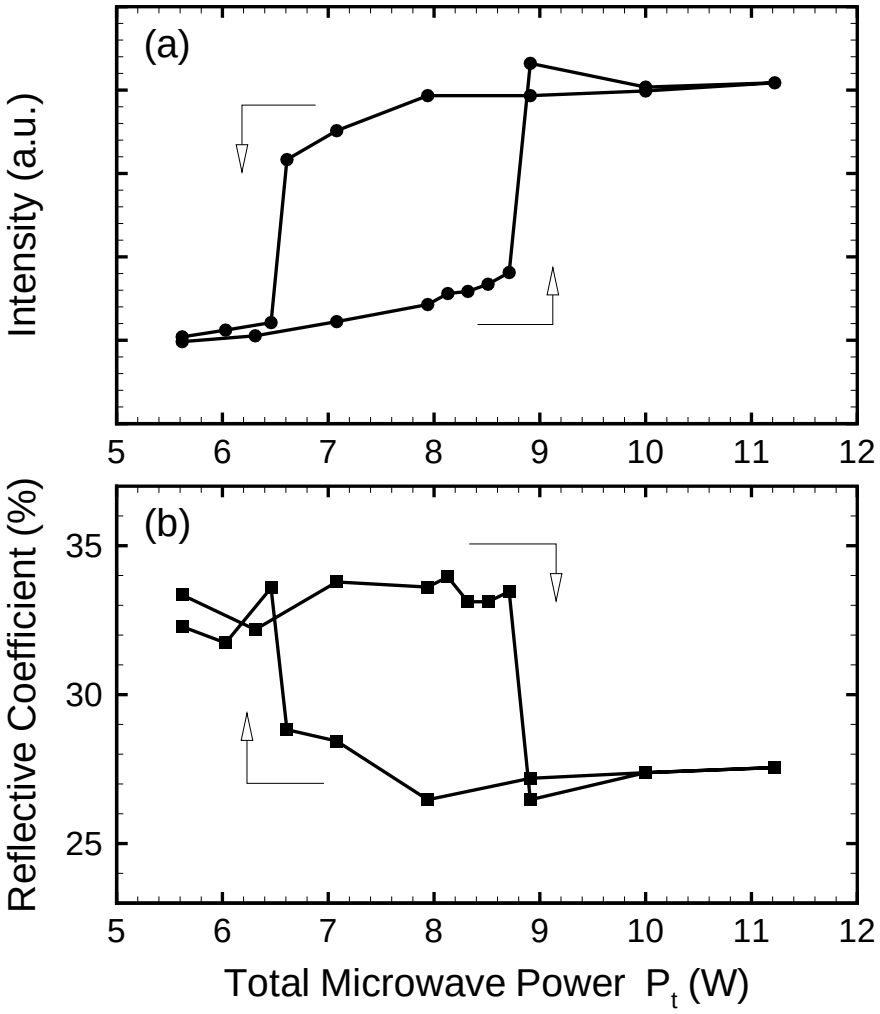

Figure 3.3: (a) Emission intensities of Ar I line (811.5 nm) and (b) reflective coefficients as a function of total microwave power P_{t}. The other conditions are the same as those in Fig. 3.2.

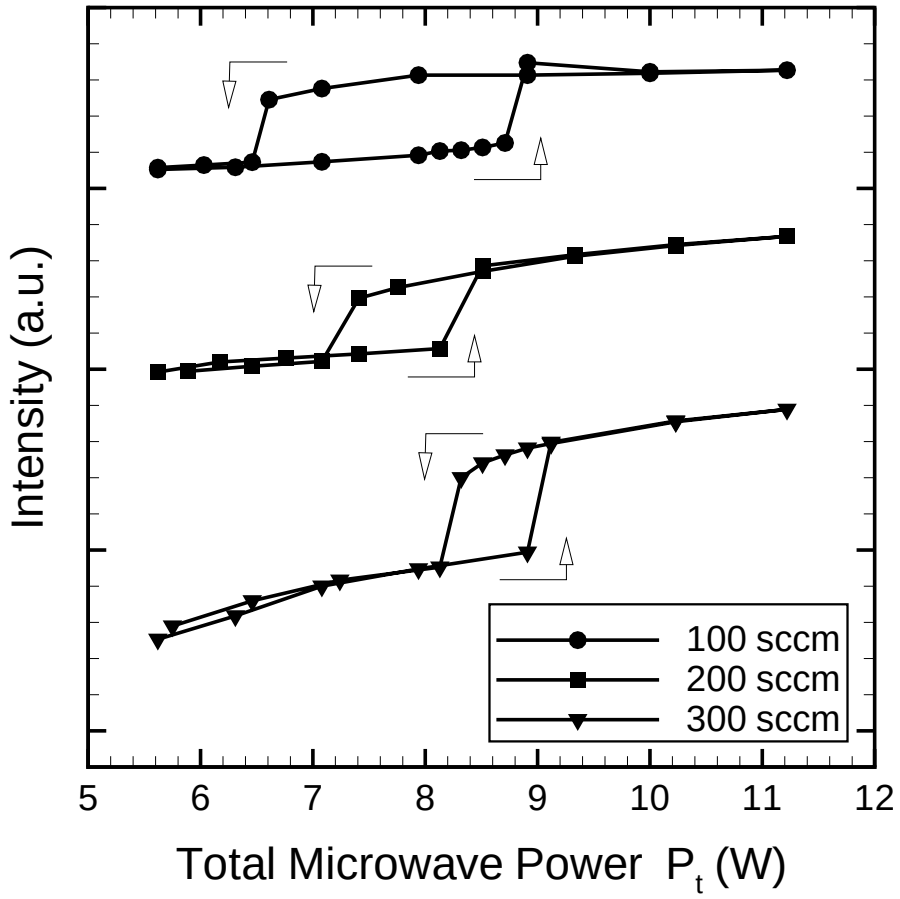

Figure 3.4: Emission intensities of Ar I line (811.5 nm) as a function of total microwave power P_{t} for three Ar flow rates: 100 sccm; 200 sccm; and 300 sccm. Corresponding feed gas pressures and ambient pressures: 10 kPa, 16 Pa; 15 kPa, 23 Pa; and 20 kPa, 29 Pa. Microwave frequency $f = 4$ GHz.

attenuated upon entering the plasma chamber from the end of the coaxial cable, while in the high-intensity mode, propagated along the plasma-dielectric interface, so that the plasma was sustained even outside in the vicinity of the chamber exit. Since higher electron densities are expected at higher intensities and larger microwaves power, we would ascribe this difference to whether or not the electron density exceeds the surface-wave resonance density n_{SW}, where $n_{\mathrm{SW}} = 9.5 \times 10^{17}$ m^{-3} at the microwave frequency $f = 4$ GHz and dielectric constant of the plasma chamber $\varepsilon_{\mathrm{d}} = 3.8$. To confirm this, further optical and electrical diagnostics are required.

Finally, to investigate the effect of flow on plasma discharges, experiments have been conducted for various flow rates. Figure 3.4 shows emission intensities of Ar I

line (811.5 nm) as a function of total microwave power P_t for three Ar flow rates: 100 sccm; 200 sccm; and 300 sccm, where corresponding feed pressures and ambient pressures were 10 kPa, 16 Pa; 15 kPa, 23 Pa; and 20 kPa, 29 Pa, respectively, and the microwave frequency was 4 GHz. Notice that the values of reflective coefficient at the flow rates of 200 and 300 sccm were between 0.25 and 0.35, showing little difference from those in Fig. 3.3(b). As shown in the figure, the power range where the hysteresis occurs has a tendency to become smaller with increasing flow rate, whereas at lower or higher powers the power dependence of intensities appears to become larger as the flow rate increases. These results indicate that the flow had an effect on plasma discharges.

In view of the fact that the power supply and the propellant storage are strictly limited for microspacecraft, it is obviously desirable to minimize power consumption and flow rates. The results of the optical emission spectrometry show that the plasma source in the high-intensity mode absorbs the microwave power more effectively, expected to produce a high kinetic energy through a micronozzle if it is provided; furthermore, once the mode is raised up to the high-intensity mode, the lower flow rate can sustain it at lower microwave powers. This means that the plasma source obtained here is likely to prove useful for the microthruster.

3.4 Conclusions

A miniature microwave-sustained plasma source has been fabricated. The plasma source consists of a quartz plasma chamber 10 mm in length and 1.5 mm in inner diameter covered with a metallic mesh for observation, where the one end of the tube is pinched and has an orifice of 0.8 mm in diameter at the exit to vacuum. The Ar plasma is excited and sustained by 4-GHz microwaves at powers of < 12 W, being observed by optical emission spectroscopy.

At an Ar gas flow rate of 100 sccm, the emission intensity increases slightly with increase in microwave power, rises sharply at a power of 9 W, and then increases gradually again, while the intensity decreases as the power decreases, involving a steep drop at a power of 6.5 W. The reflective power also drops or rises drastically at the same power where the significant change of intensity occurs, showing a slight hysteresis. The power range where the hysteresis occurs tends to be smaller with increasing gas flow rate. Moreover, the plasma is maintained only inside the quartz tube at lower intensities

while the plasma is blown out to the chamber as a free jet at higher intensities. The color and spectra of the plasma are also found to be changed.

This implies that plasma discharges involve a mode change depending on the microwave power and Ar gas flow rate. This change would be ascribed to whether the electron density exceeds the surface-wave resonance density or to forming different patterns of standing waves in the plasma source. Since at lower flow rates the plasma can easily be maintain as a high-intensity mode with lower applied powers, the plasma source would be useful for the microthruster in view of the fact that the power supply and the propellant storage are strictly limited for microspacecraft. However, the reflected power is unfavorably large and should be reduced for the effective use of microwave powers, which is left for future work.

4

Plasma diagnostics and thrust performance estimation

4.1 Introductory remarks

The microplasma source developed in Chap. 3 could not suppress the reflective power below about 30 % owing to a relatively low microwave frequency of 4 GHz for the microplasma thruster as indicated in Chap. 2. In this chapter, the microplasma source has been improved to reduce the reflective microwave power and then plasma diagnostics have been conducted without a micronozzle. The diagnostics consists of optical emission spectroscopy (OES) and an electrostatic probe measurement. The objective of this study is to investigate the plasma characteristics of the microplasma source developed and to find an optimum operational condition for the microplasma thruster at microwave input powers below 10 W. The following sections give some of the results.

4.2 Experimental setup and procedure

4.2.1 Setup

Figure 4.1 shows a schematic diagram of the experimental setup for optical and electrical diagnostics. Microwave signals of 2 and 4 GHz generated by an oscillator (Agilent Technologies, 8648D) are amplified with respective 4-stage semiconductor amplifiers

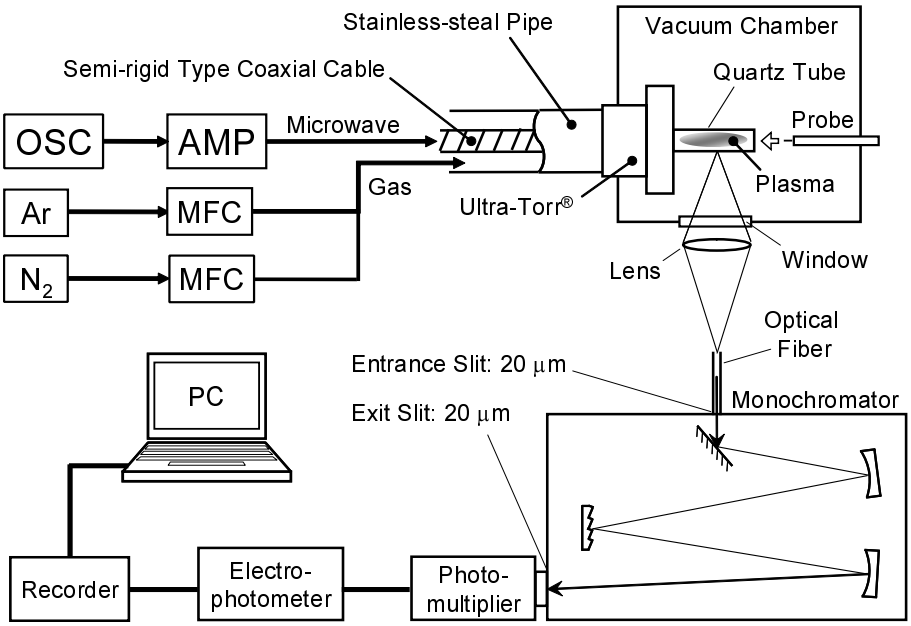

Figure 4.1: Schematic of the experimental setup for optical and electrical diagnostics.

(Micro Denshi, MRF-2G-1 and MRF-4G-2), and then fed through a semi-rigid coaxial cable (RG-405/U) into a plasma chamber made of a straight quartz tube, to generate and sustain plasma discharges therein. Here, the reflection of the microwave power is suppressed by adjusting the cable length. The quartz tube is connected to a stainless-steel pipe through which a working gas is introduced, and then inserted into a stainless-steal chamber evacuated by a dry and turbo-molecular pump, where Ar is mainly employed and N_2 is used only for the measurement of the rotational temperature. The stainless-steal pipe is equipped with a Bourdon tube pressure gauge upstream of the plasma chamber to measure the feed gas pressure. This feed gas pressure is assumed to be equal to the plasma chamber pressure in this study.

4.2.2 Microplasma source

Figure 4.2 shows an assembly of the microplasma source presently fabricated, which is based on the concept of the large scale microwave plasma source developed by Tuda *et al.* [84, 85]. The center conductor of the semi-rigid coaxial cable, protruding 10 mm beyond the insulator and outer conductor, is covered with a ceramic tube; two types of ceramics, mullite (relative permittivity $\varepsilon_d = 6$) and zirconia ($\varepsilon_d = 12$–25), are employed to investigate its dependence on dielectric constants. The outer conductor is

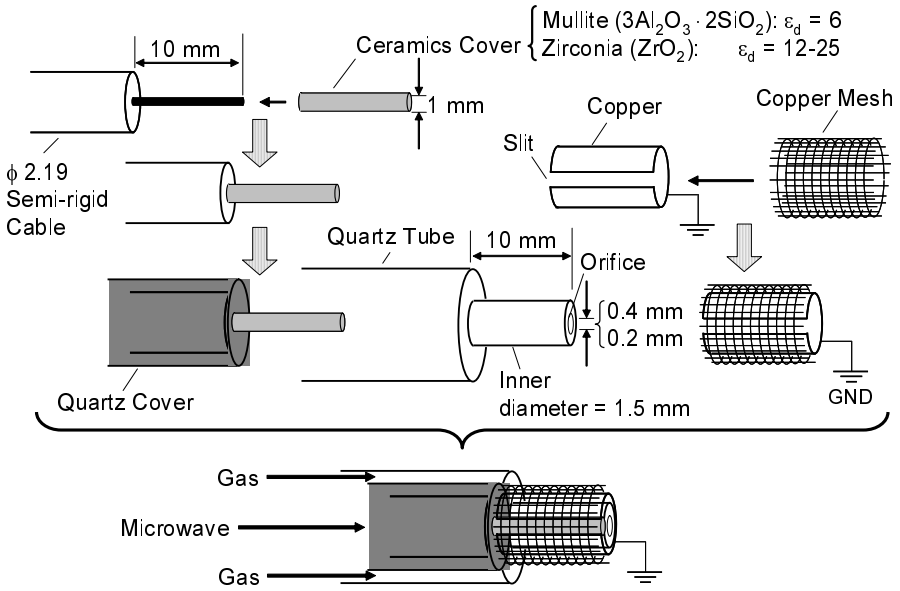

Figure 4.2: Assembly of the microplasma source presently developed, which has an orifice at the exit to vacuum. The slit of the copper envelope is for optical diagnostics.

also covered with a quartz tube for the protection against electrodes erosion. Here, the ceramic tube and the quartz tube are joined to a ceramic adhesive. The plasma chamber, made of a quartz tube 10 mm in length and 1.5 mm in inner diameter, has an orifice 0.4 and 0.2 mm in diameter at the exit to vacuum. (In plasma diagnostics, the 0.4-mm orifice was mainly employed.) This structure results in a small conductance to keep the pressure inside the plasma chamber much higher than that in the vacuum chamber. The outside of the plasma chamber is covered with a copper grounded which has a single slit for optical diagnostics. Moreover, a copper mesh prevents microwaves from leaking through the slit.

4.2.3 Optical diagnostics

For optical diagnostics, firstly emission intensities are measured with a spectrometer (Ocean Optics, HR2000CG-UV-NIR) through a quartz optical fiber, the head of which is directly connected to a window of the vacuum chamber without a lens as shown in Fig. 3.1 of Chap. 3. Here, the spectrometer has a 10-cm focal length and a 300 grooves/mm grating plate. In the case of precise diagnostics, the emissions are collected by a lens and transmitted to a 25-cm focal length monochromator (Nikon, P250) with a 1200 grooves/mm grating plate. The light emerging from the fiber is focused onto an

entrance slit of the monochromator and detected by a photomultiplier (Hamamatsu, R1509) as shown in Fig. 4.1. Both the entrance and exit slits are set at 20 μm.

4.2.4 Electrical diagnostics

For electrical diagnostics, a cylindrical Langmuir probe is positioned at an immediate downstream of the orifice to determine the electron density thereat as shown in Fig. 4.3. The probe tip is made of a tungsten wire 0.05 mm in diameter and 0.5 mm long. Here, the wire except the probe tip is thinly coated with a ceramic bond, the diameter of which is kept less than about 0.2 mm to minimize perturbation due to the probe measurement. The plasma electron density was determined from an electron saturation current of the probe with the electron temperature obtained and compensation derived from the collisional effect [86]. A typical example of probe current-voltage characteristics is also shown in Fig. 4.3.

4.3 Plasma diagnostics

4.3.1 Reflective coefficient

Figure 4.4 shows reflective coefficient as a function of total microwave power P_t for different $f = 2$ and 4 GHz and different $\varepsilon_\mathrm{d} = 6$ and 12–25, measured at an Ar flow rate of 50 sccm. Here, the reflective coefficient is defined as the ratio of the reflected power to the total microwave power. While the reflective coefficient of 2 GHz is not less than 30 %, that of 4 GHz is suppressed below 15 % and even below 5 % for the zirconia tube. The plasma source currently developed indicates that more effective use of microwave power can be realized compared to that previously developed in Chap. 3.

4.3.2 Power dependence of intensity

Figure 4.5 shows photograph images of the emission of microplasma discharges, taken for a total microwave power P_t = (a) 3.5, (b) 5.0, and (c) 7.0 W with a microwave frequency $f = 4$ GHz and a mullite tube ($\varepsilon_\mathrm{d} = 6$), measured at an Ar flow rate of 50 sccm. The plasma was maintained only inside the microplasma chamber at $P_\mathrm{t} > 0.3$ W [Fig. 4.5(a)], the plasma at $P_\mathrm{t} > 4$ W was found to flow out into vacuum through the orifice at the end of the plasma chamber, forming a supersonic free jet [Fig. 4.5(b)], and at $P_\mathrm{t} > 6$ W the exhausted plasma was sustained around the end of

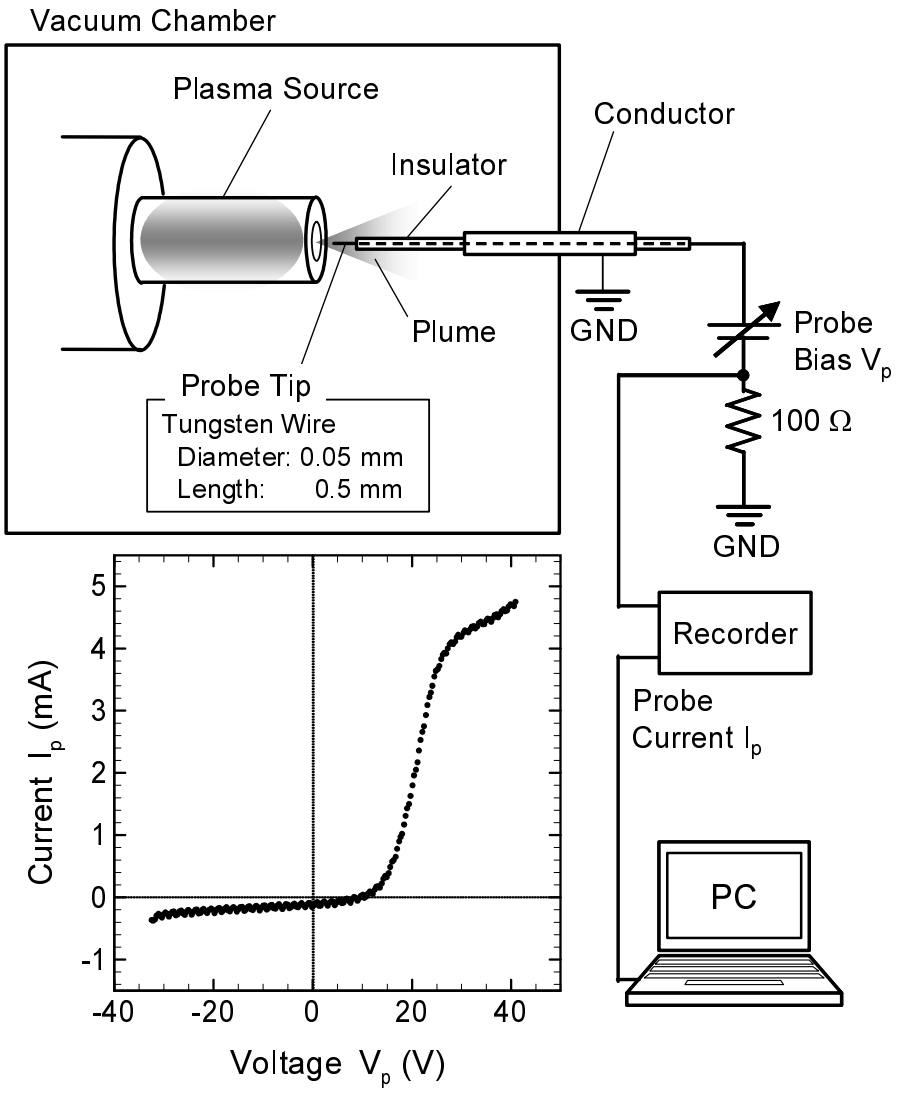

Figure 4.3: Schematic of an electrical circuit for measuring the probe current I_p and a typical example of probe I-V characteristics.

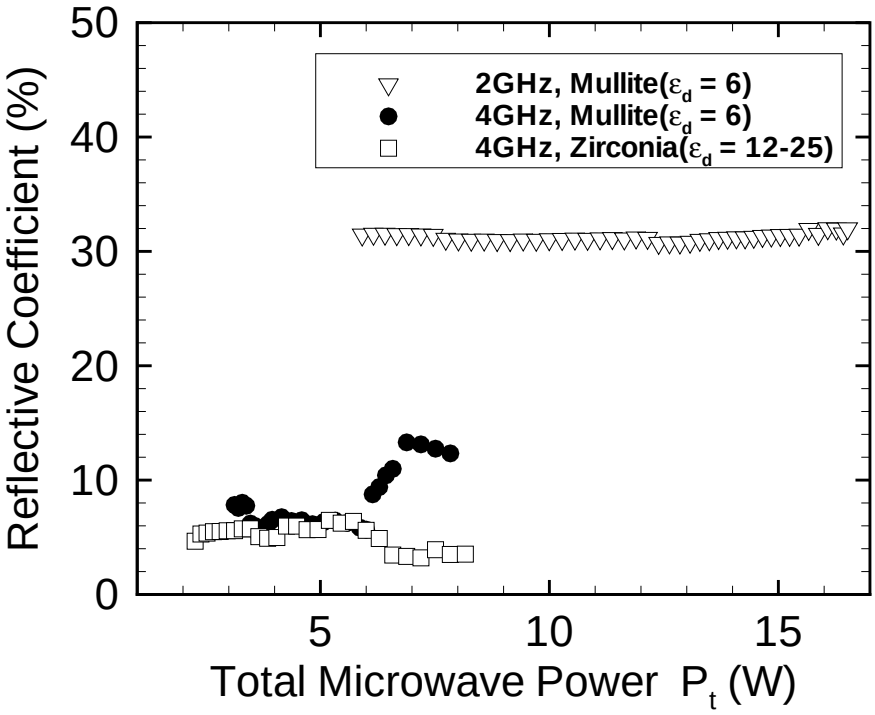

Figure 4.4: Reflective coefficient as a function of total microwave power P_{t} for different $f = 2$ and 4 GHz and different $\varepsilon_{\mathrm{d}} = 6$ and 12–25, measured at an Ar flow rate of 50 sccm.

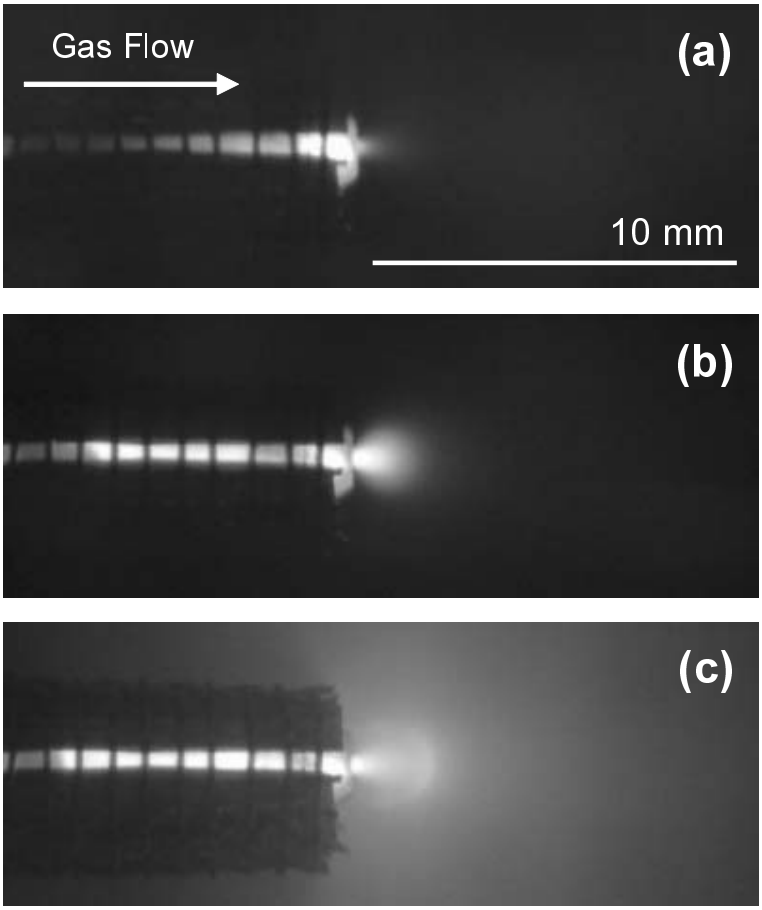

Figure 4.5: Photograph images of the emission of microplasma discharges, taken for a total microwave power P_t = (a) 3.5, (b) 5.0, and (c) 7.0 W with a microwave frequency $f = 4$ GHz and a mullite tube ($\varepsilon_d = 6$), measured at an Ar flow rate of 50 sccm. Here, the plasma chamber pressure varied from 5 to 12 kPa with increasing P_t in the range from 0 to 12 W.

the plasma source [Fig. 4.5(c)]. Here, the plasma chamber pressure varied from 5 to 12 kPa with increasing P_t in the range from 0 to 12 W, owing to an increase in gas temperature.

Figure 4.6 shows the emission intensity (Ar I 763.5 nm) as a function of incident microwave power $P_{in} = P_t - P_{rf}$ for different $f = 2$ and 4 GHz, where P_{rf} is a reflected microwave power, so that P_{in} is assumed to be a net power absorbed in the plasma. Other experimental conditions are the same as in Fig. 4.5. The emission intensity increases with increasing P_{in}, involving sudden intensity jumps among the regions labeled (a), (b), and (c) in the figure, where these labels correspond to those in Fig. 4.5. As shown in the figure, higher intensities are observed for the higher microwave frequency

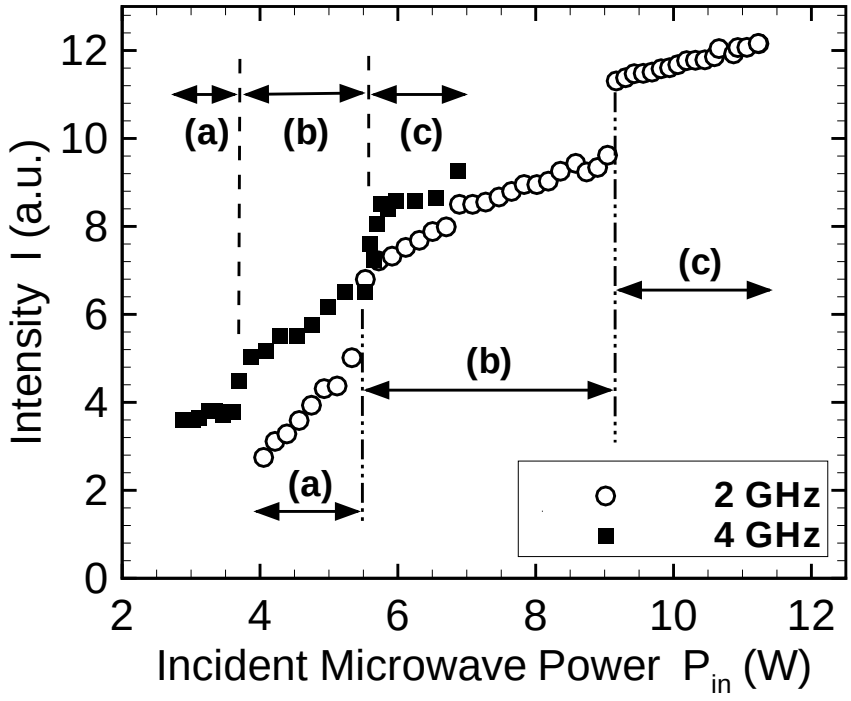

Figure 4.6: Emission intensity (Ar I 763.5 nm) as a function of incident microwave power $P_{\rm in} = P_{\rm t} - P_{\rm rf}$ for different microwave frequencies $f = 2$ and 4 GHz, otherwise measured under the same conditions as in Fig. 4.5.

at the same incident microwave power; more incident microwave power is required to yield jumps for $f = 2$ GHz.

Figure 4.7 shows the emission intensity (Ar I 763.5 nm) as a function of incident microwave power $P_{\rm in}$ for different ceramic tubes of $\varepsilon_{\rm d} = 6$ and 12–25, where other experimental conditions are the same as in Fig. 4.5. The emission intensity increases with increasing $P_{\rm in}$, involving sudden jumps among the regions labeled (a), (b), and (c), like the result in Fig. 4.6. Higher intensities are observed for $\varepsilon_{\rm d} = 12$–25 at the same incident microwave power. From the results in Figs. 4.6 and 4.7, the higher microwave frequency and dielectric constant would be useful to maintain the plasma discharges in the microplasma source developed here.

Note that the emission intensities were measured with the spectrometer without light condensing here, so that the sudden increase in emission intensity was mainly due to the increase in area of the plasma discharges sustained.

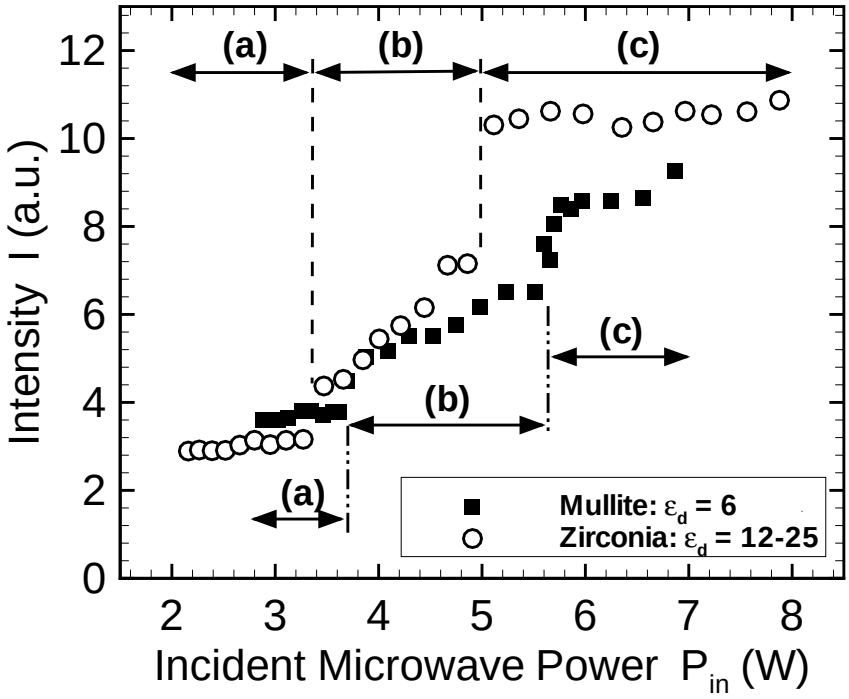

Figure 4.7: Emission intensity (Ar I 763.5 nm) as a function of incident microwave power $P_{\mathrm{in}} = P_{\mathrm{t}} - P_{\mathrm{rf}}$ for different dielectric constants $\varepsilon_{\mathrm{d}} = 6$ and 12–25, otherwise measured under the same conditions as in Fig. 4.5.

4.3.3 Electron density

The results of the intensity measurement imply that higher microwave frequencies and dielectric constants lead to higher electron densities in the microplasma source. Figure 4.8 shows the electron density n_e as a function of incident microwave power P_{in} for different $f = 2$ and 4 GHz and different $\varepsilon_d = 6$ and 12–25. The other conditions are the same as in Fig. 4.5. The electron density increases as P_{in} increases; the higher microwave frequency and dielectric constant result in higher electron densities, which is especially clear at higher P_{in}, although the n_e for $f = 2$ GHz and $\varepsilon_d = 6$ does not decrease with decreasing P_{in} at lower P_{in} compared to that for $f = 4$ GHz. This result would be derived from disturbance due to the probe measurement at $f = 2$ GHz. As shown in Fig. 4.2, the plasma source has an electrically open end at the exit, where ideally, all of the electric fields is reflected. In reality, some radiation occurs and then the radiated fields are attenuated immediately near the exit. The region such electric fields have effect on is larger at $f = 2$ GHz than that at $f = 4$ GHz because of the longer wavelength, and thus the radiated electric fields would interact with the probe. Taking the disturbance into account, we could conclude that the electron density tends to become higher at higher microwave frequencies and dielectric constants.

4.3.4 Rotational temperature

In order to estimate the gas temperature, which is one of the critical parameters for the thrust performance [87], a small amount of N_2 was added to the Ar plasma and its rotational spectra were observed. Since the monochromator employed in this paper does not resolve the rotational structure, we fitted the experimental data with theoretical calculations by using the transition band of N_2 $C^3\Pi_u$-$B^3\Pi_g$ at 380.49 nm (second positive band) [88–90], and then obtained the rotational temperature. Figure 4.9(a) shows an experimentally observed spectrum for the second positive system of N_2 and Fig. 4.9(b) shows a typical numerical fit and an experimentally observed spectrum.

Figure 4.10 shows the rotational temperature T_{rot} at the exit of the plasma chamber, i.e., orifice as a function of incident microwave power P_{in} for different $f = 2$ and 4 GHz and different $\varepsilon_d = 6$ and 12–25, measured at an Ar flow rate of 50 sccm and a N_2 flow rate of 0.5 sccm. The rotational temperature increases with increasing P_{in}, where the temperature clearly tends to be higher at the higher microwave frequency and dielectric

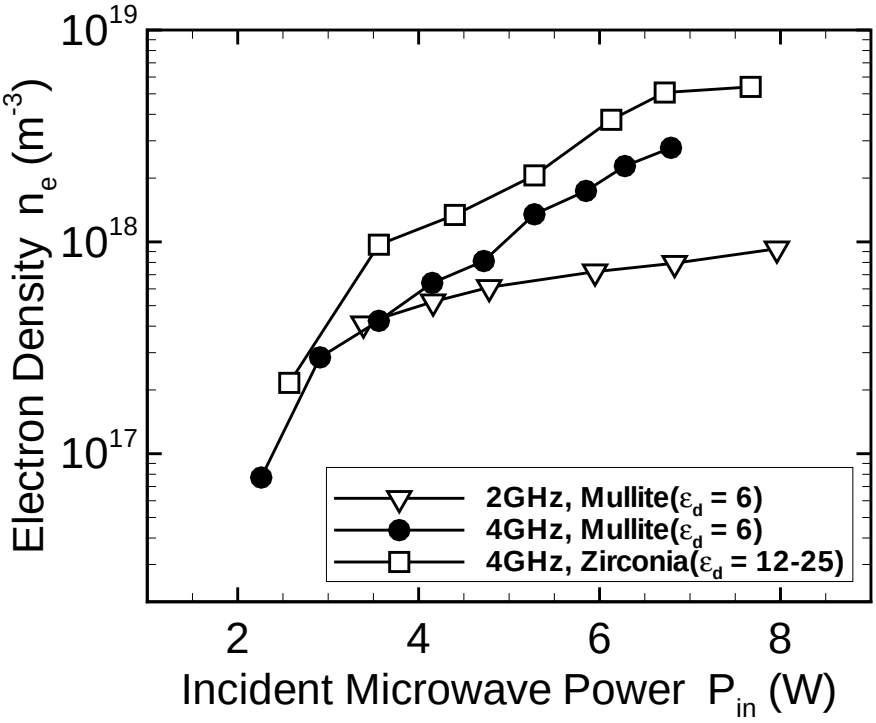

Figure 4.8: Electron density n_e as a function of incident microwave power P_{in} for different $f = 2$ and 4 GHz and different $\varepsilon_d = 6$ and 12–25, otherwise measured under the same conditions as in Fig. 4.5. Here, the Langmuir probe was located at an immediate downstream from the orifice as in Fig. 4.1; thus, the n_e may be larger about an order of magnitude in the microplasma chamber.

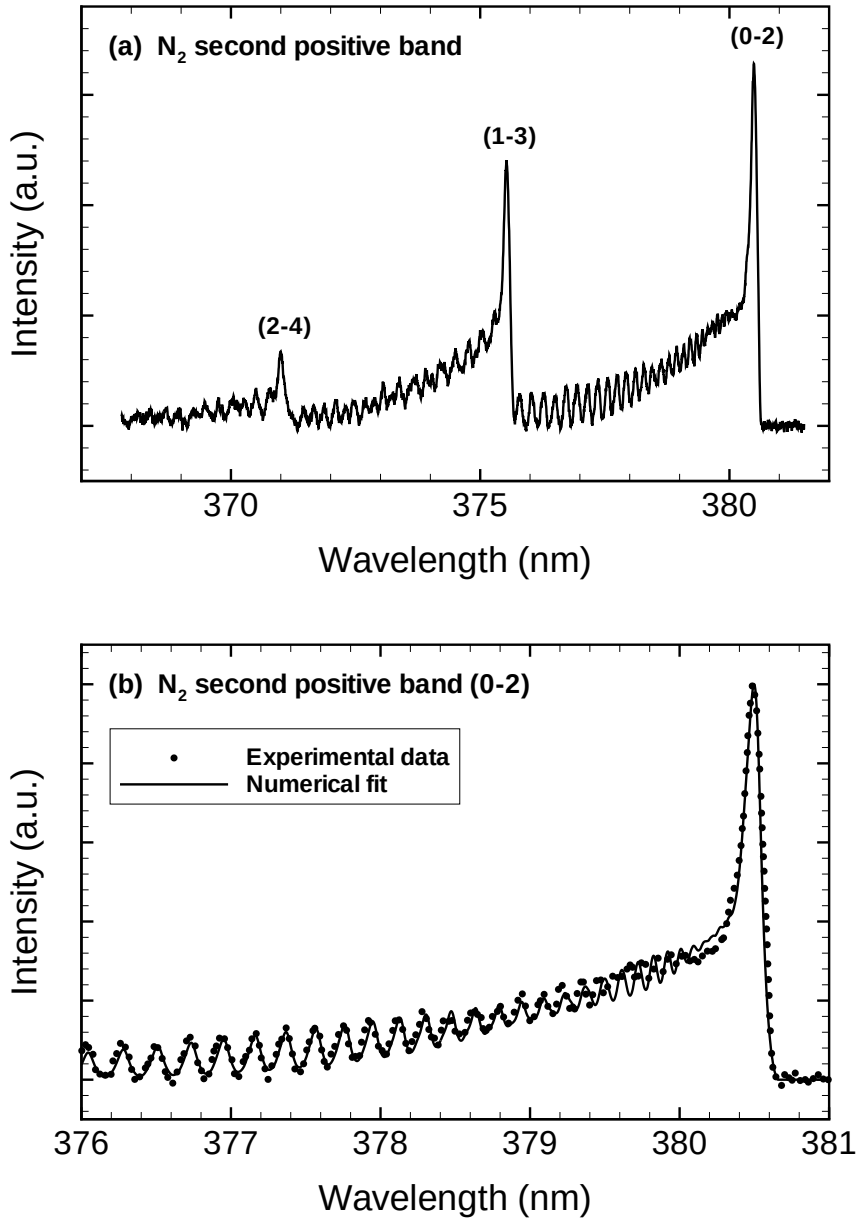

Figure 4.9: (a) Experimentally observed spectrum for the second positive system of N_2 and (b) a typical numerical fit and an experimentally observed spectrum.

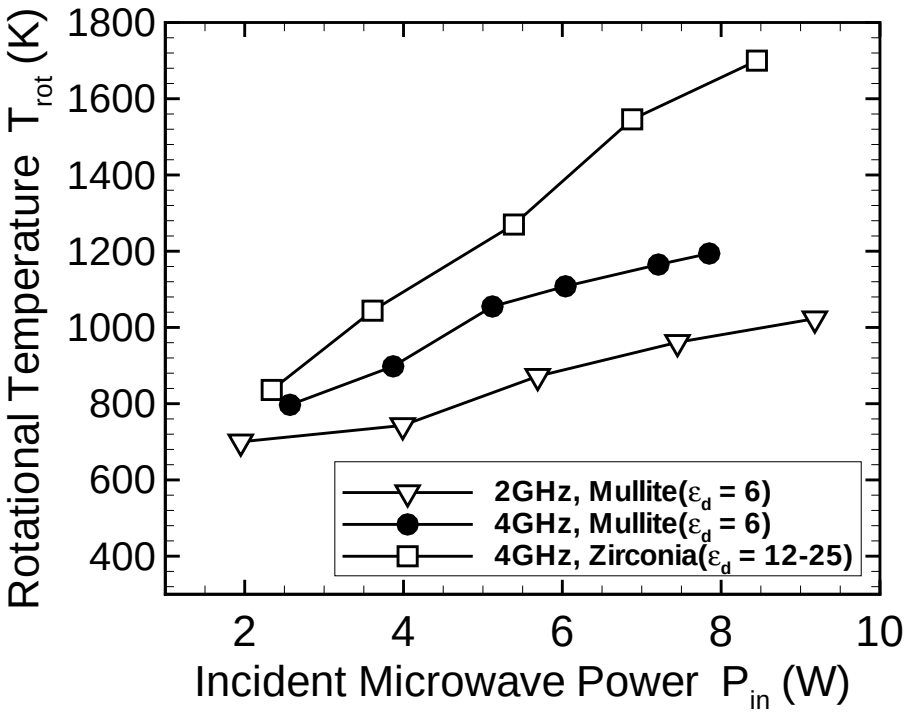

Figure 4.10: Rotational temperature $T_{\rm rot}$ (N_2) at the orifice as a function of incident microwave power $P_{\rm in}$ for different f = 2 and 4 GHz and different $\varepsilon_{\rm d}$ = 6 and 12–25, measured at an Ar flow rate of 50 sccm and a N_2 flow rate of 0.5 sccm. Here, the plasma chamber pressure varied from 5 to 12 kPa with increasing $P_{\rm in}$ in the range from 0 to 10 W.

constant as in the case of the emission intensity and electron density. Note that the plasma chamber pressure also increases from 5 to 12 kPa as $P_{\rm in}$ increases in the range from 0 to 10 W, resulting from the increase in $T_{\rm rot}$.

The discussion so far indicates that high microwave frequencies and dielectric constants are useful for the microplasma thruster because of high electron densities and rotational temperatures in the microplasma source. As the microwave frequency and dielectric constant increase, the wavelength of electromagnetic fields becomes shorter, so that effective confinement of microwave fields could be obtained in the microplasma source. Moreover, the reflected microwave power $P_{\rm rf}$ of 2 GHz could not be suppressed less than 30 % during the measurement, whereas that of 4 GHz was kept to be below 15 % as shown in Fig. 4.4. In view of effective use of microwave power, the best combination of the microwave frequency and dielectric tube is 4 GHz and a zirconia tube in this study.

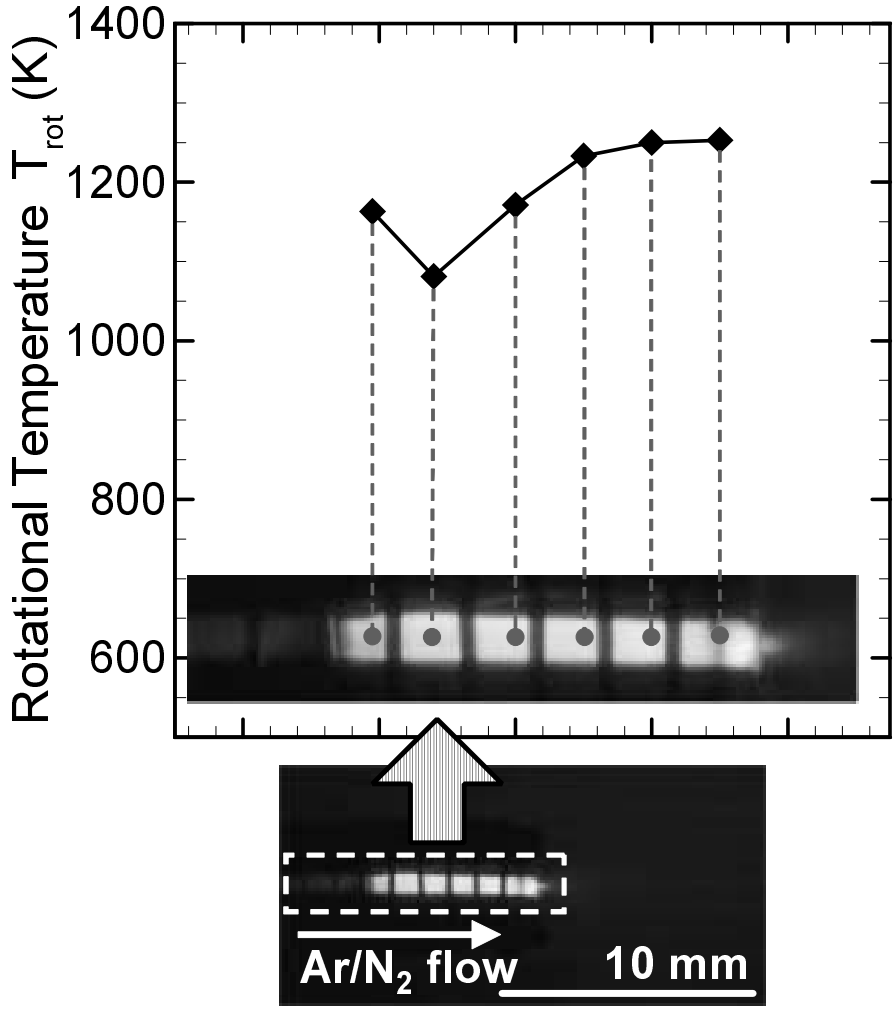

Figure 4.11: Rotational temperature T_{rot} (N_2) as a function of position of the plasma discharge (top) and photograph image of the emission (bottom), taken for an incident microwave power $P_{\mathrm{in}} = 5$ W with a microwave frequency $f = 4$ GHz and a zirconia tube ($\varepsilon_{\mathrm{d}} = 12$–$25$), measured under the same Ar/N_2 flow rates as in Fig. 4.10, where the plasma chamber pressure was 10 kPa.

Figure 4.11 shows the rotational temperature T_{rot} as a function of position of the plasma discharge for a microwave frequency $f = 4$ GHz and a zirconia tube ($\varepsilon_{\mathrm{d}} = 12$–$25$), with a photograph image of the emission taken for an incident microwave power $P_{\mathrm{in}} = 5$ W, measured at an Ar flow rate of 50 sccm, N_2 flow rate of 0.5 sccm, and the plasma chamber pressure of 10 kPa. The rotational temperature increases from upstream toward downstream before the exit of the plasma chamber. The structure of the plasma source allows the maximum electric field at the orifice because of the electrically open end thereat. The distribution of the rotational temperature showing the maximum temperature at the orifice is consistent with this fact.

Notice that it is important to increase the temperature at the exit of the plasma chamber where a micronozzle is equipped, because the plasma thermal energy should be effectively converted into kinetic energy without any undesirable energy loss in the plasma chamber before the micronozzle. Thus, the temperature distribution obtained also indicates that the microplasma source is desirable in the miniature thruster presented here.

4.4 Thrust performance estimation

4.4.1 Orifice diameter dependence

In addition to the gas temperature, the plasma chamber pressure is another critical parameter for the thrust performance [87, 91]. The chamber pressure can be controlled by gas flow rates or orifice diameters, i.e., flow conductance. In this section, two types of orifice diameters were employed to investigate its dependence of the gas temperature and the plasma chamber pressure with the same gas flow rates.

Figure 4.12 shows the rotational temperature T_{rot} (N_2) as a function of incident microwave power P_{in} for different orifice diameters $\phi = 0.2$ and 0.4 mm with a microwave frequency $f = 4$ GHz and a zirconia tube ($\varepsilon_{\mathrm{d}} = 12$–$25$), measured at an Ar flow rate of 50 sccm and N_2 flow rate of 0.5 sccm. While the plasma chamber pressure varied from 18 to 41 kPa at $\phi = 0.2$ mm and from 5 to 12 kPa at $\phi = 0.4$ mm with increasing P_{in}, no significant difference of the rotational temperature between the two types of diameters is shown in the figure, so that relatively high gas temperatures were obtained even at high plasma chamber pressures.

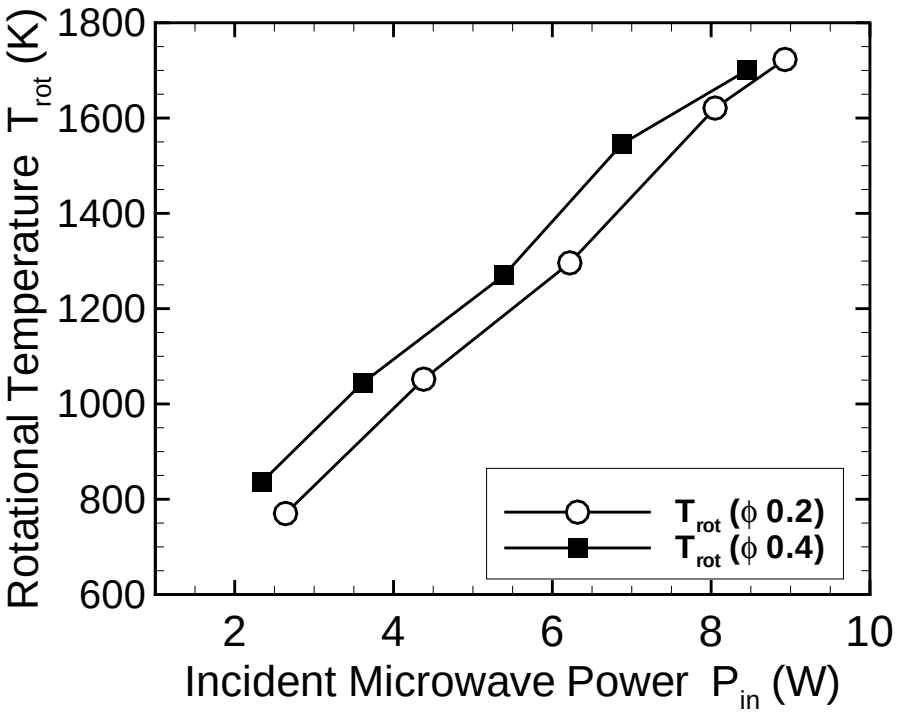

Figure 4.12: Rotational temperature $T_{\rm rot}$ (N_2) at the orifice as a function of incident microwave power $P_{\rm in}$ for different orifice diameters $\phi = 0.2$ and 0.4 mm with a microwave frequency $f = 4$ GHz and a zirconia tube ($\varepsilon_{\rm d} = 12$–25), measured under the same Ar/N_2 flow rates as in Fig. 4.10. Here, the plasma chamber pressure varied from 18 to 41 kPa at $\phi = 0.2$ mm and from 5 to 12 kPa at $\phi = 0.4$ mm with increasing $P_{\rm in}$ in the range from 0 to 10 W.

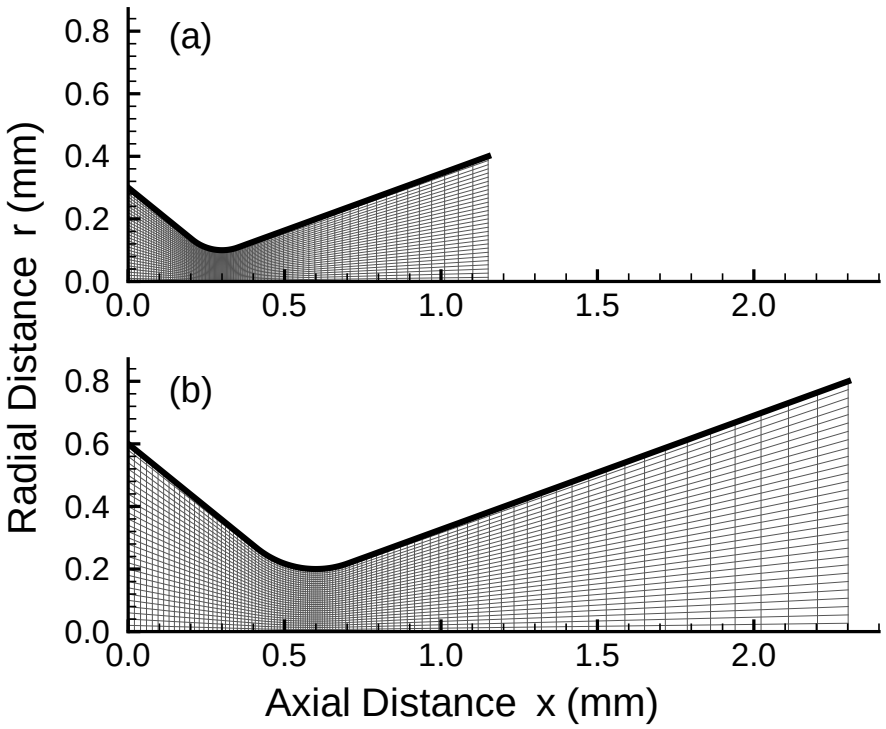

Figure 4.13: Cross-sectional view and computational grid for micronozzles with a 20°-half-cone-angle isothermal wall ($T_{\rm wall}$ = 300 K). The radii of the nozzle inlet, throat, and exit are set at 0.3, 0.1, and 0.4 mm, respectively, in (a), while the twice of them with the same aspect ratio in (b). The computational domain of both nozzles is divided into 100 cells in the axial direction and 30 cells in the radial direction.

4.4.2 Numerical estimation

Assuming that the rotational temperature $T_{\rm rot}$ equals the gas temperature $T_{\rm gas}$, we estimated the thrust performance by using the results of plasma diagnostics obtained above and the numerical model developed in Ref. [87].

Since the plasma source has an orifice of 0.2 and 0.4 mm in diameter at the exit to vacuum, a micronozzle with a throat 0.2 and 0.4 mm in diameter is assumed to be equipped with each plasma chamber in order to calculate the thrust performance. A cross-sectional view and computational grid for two micronozzles are shown in Fig. 4.13. Here, the aspect ratio of both nozzles is the same, so that the same thrust performance is obtained with the same nozzle inlet conditions for ideal fluid [80]. At the nozzle wall, an isothermal-wall ($T_{\rm wall}$ = 300 K) and non-slip conditions were employed.

The thrust performance was evaluated by calculating the thrust $F_{\rm t}$, reaction force

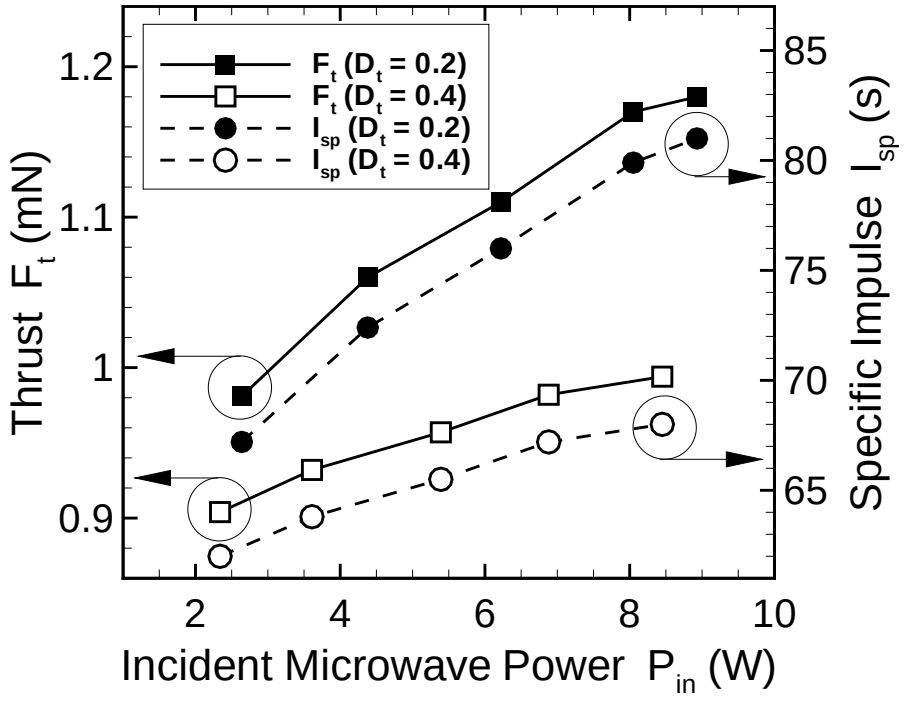

Figure 4.14: Thrust performance as a function of incident microwave power $P_{\rm in}$ for different throat diameters $D_{\rm t} = 0.2$ and 0.4 mm, calculated at a Ar flow rate of 50 sccm (1.5 mg/s). The nozzle inlet conditions, such as the gas temperature, were taken from Fig. 4.12.

to propel spacecraft, and the specific impulse $I_{\rm sp}$, fuel efficiency of thrusters, defined as

$$F_{\rm t} = 2\pi \int_0^{r_{\rm ex}} (\rho u^2 + p)\, r dr, \tag{4.1}$$

$$I_{\rm sp} = F_{\rm t} \left(g\, 2\pi \int_0^{r_{\rm ex}} \rho u\, r dr \right)^{-1} = \frac{F_{\rm t}}{\dot{m} g}, \tag{4.2}$$

where $r_{\rm ex}$ is the exit radius of the nozzle, ρ is the mass density, u is the exhaust velocity in the axial direction, p is the pressure, $\dot{m}$ is the mass flow rate, and g is the gravitational constant [70]. Note that $F_{\rm t}$ consists of the momentum and pressure thrust. The pressure thrust is usually neglected owing to its less contribution to the total thrust. However, reducing the size of nozzles results in under-expanded gas flows inside nozzles, so that the pressure thrust should also be included as shown in Eq. (4.1) [87].

Figure 4.14 shows the thrust performance as a function of incident microwave

power $P_{\rm in}$ for different throat diameters $D_{\rm t}$ = 0.2 and 0.4 mm, calculated at a Ar flow rate of 50 sccm (1.5 mg/s). Here, the nozzle inlet conditions were taken from Fig. 4.12. Both the thrust $F_{\rm t}$ and specific impulse $I_{\rm sp}$ are higher at $D_{\rm t}$ = 0.2 mm than those at $D_{\rm t}$ = 0.4 mm; the difference becomes larger with increasing $P_{\rm in}$. As shown in Fig. 4.12, while almost the same rotational temperature, i.e., gas temperature was obtained for the two types of orifice diameters, the plasma chamber pressure at ϕ = 0.2 mm was much higher than that at ϕ = 0.4 mm. This result leads to a high Reynolds number of 417 at $D_{\rm t}$ = 0.2 mm compared to that of 209 at $D_{\rm t}$ = 0.4 mm for cold-gas flows, i.e., non-plasma flows. As discussed in Ref. [87], low-Reynolds number flows prevent smooth flow expansion, leading to significant viscous loss in the boundary layer inside the micronozzle. Moreover, such a loss becomes larger with increasing inlet gas temperature, suppressing the thrust performance, so that the increasing rate of the thrust performance at $D_{\rm t}$ = 0.4 mm is smaller than that at $D_{\rm t}$ = 0.2 mm. To obtain higher thrust performances, it is desirable to make a throat small and to keep high gas temperatures at high gas pressures for a given input microwave power.

4.5 Conclusions

An improved microwave-excited microplasma source has been fabricated, where the plasma source consists of a quartz tube and a microwave rod antenna. The quartz tube 10 mm in length and 1.5 mm in inner diameter has an orifice of 0.4 and 0.2 mm in diameter at the exit to vacuum, the outside of which is covered with a grounded copper having a single slit for optical diagnostics. The rod antenna 10 mm long, covered with two types of ceramic tubes 1.0 mm in diameter, is inserted into the quartz tube. Here, the two ceramic tubes are made of mullite (relative permittivity $\varepsilon_{\rm d}$ = 6) and zirconia ($\varepsilon_{\rm d}$ = 12–25). The Ar plasmas are generated by 2 or 4 GHz microwaves in the pressure range from 5 to 40 kPa, producing high temperature gases.

After it is found that the reflected power of microwaves can be suppressed less than 5 %, the microplasma source is investigated by optical emission spectroscopy and an electrostatic probe measurement. The emission intensity increases with increasing incident microwave power, microwave frequency, and dielectric constant, leading to higher electron densities. To estimate the gas temperature, a small amount of N_2 is added to the Ar plasma and its rotational spectra are observed. The rotational tempera-

ture also increases at higher microwave power, frequency, and dielectric constant. The distribution of the rotational temperature inside the microplasma chamber indicates that the microplasma source is desirable in the microthruster, because the temperature increases toward the exit of the plasma chamber where a micronozzle will be equipped. In the range of microwave powers 2–10 W and at an Ar gas flow rate of 50 sccm, the electron densities and rotational temperatures obtained are 10^{17}–10^{19} m^{-3} and 700–1800 K, respectively.

Numerical analysis based on the plasma diagnostics indicates that because of the maintenance of high gas temperatures at high plasma chamber pressures, smaller throat diameters of micronozzles could produce better thrust performances, having thrusts of 0.98–1.2 mN and specific impulses of 67–81 s.

The difference of the values obtained here and those obtained in Chap. 2 would attribute to the energy loss of microwaves: radiation from the open end of the plasma source, and the thermal loss of inside the coaxial cable and the plasma chamber, which are an intrinsic nature of high-frequency microwaves and thus unavoidable. Fabricating a micronozzle and measuring the thrust performance are now in progress to demonstrate the feasibility of the microplasma thruster.

5

Performance testing of a microthruster

5.1 Introductory remarks

The plasma diagnostics conducted in Chap. 4 have shown that the emission intensity, electron density, and rotational temperature increase with increasing microwave frequency and dielectric constant, so that the best combination of the microwave frequency and dielectric tube is 4 GHz and a zirconia tube. However, in view of the fact that the long-time operation is required for microspacecraft missions with microthrusters, ceramic tubes have a serious problem; ceramics are vulnerable to a heat shock. In some cases, the ceramic cover used was found to crack after the long-time plasma diagnostics as shown in Fig. 5.1. To avoid this problem, a quartz tube is employed for the rod antenna cover because of its much lower coefficient of thermal expansion (5×10^{-7} K^{-1}) compared to mullite (5×10^{-6} K^{-1}) and zirconia (1×10^{-5} K^{-1}), and we have confirmed that it is durable under the long-time operation even at high microwave powers.

In this chapter, a micronozzle is fabricated, being connected to a microplasma source to measure the thrust performance of a microplasma thruster developed. In order to measure the thrust, thrust stands are required. Although several methods of thrust measurement have been proposed, they are roughly divided into two categories. The one is to measure displacement of a target hit by the exhaust plume from thrusters

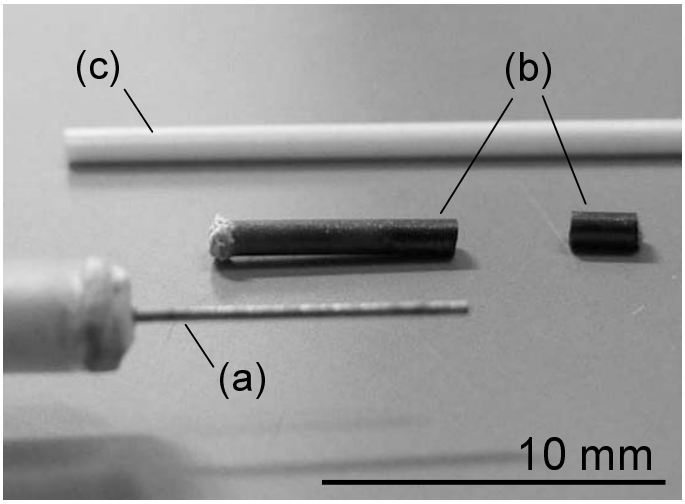

Figure 5.1: Photograph images of (a) microwave antenna without a ceramic cover, (b) a failed zirconia cover the color of which was turned into black after the long-time plasma diagnostics, and (c) a zirconia tube before plasma diagnostics.

which are tightly fixed, and the other is to measure displacement caused by a reaction force of thrusters which are mounted on movable structure, where the former is referred to as the target method [92, 93]. Depending on moving directions, the latter is further divided into two types. The one is that thrusters are mounded on one end of a rigid long arm rotating vertically around a fulcrum without frictions like a pendulum, where a restoring force is produced by the gravity, elastic members, or springs, so that this method is referred to as the pendulum method [94–97]. The other is a torsional type thrust stand that oscillates horizontally, where a thruster is installed on the torsional balance, which is supported by flexure pivots providing a restoring force by a spring, and the counter weight is on the other side [98–101]. Since this torsional type thrust stand is developed for the characterization of micronewton thrusters, the target and pendulum methods are employed in the thrust measurement here.

5.2 Experimental setup and procedure

5.2.1 Microthruster

Figure 5.2(a) shows a cross-sectional view of the microplasma thruster. The plasma source of the microthruster is made of a straight quartz tube 10 mm in length, 1.5 mm in inner diameter, and 3.0 mm in outer diameter. A micronozzle is joined to one end

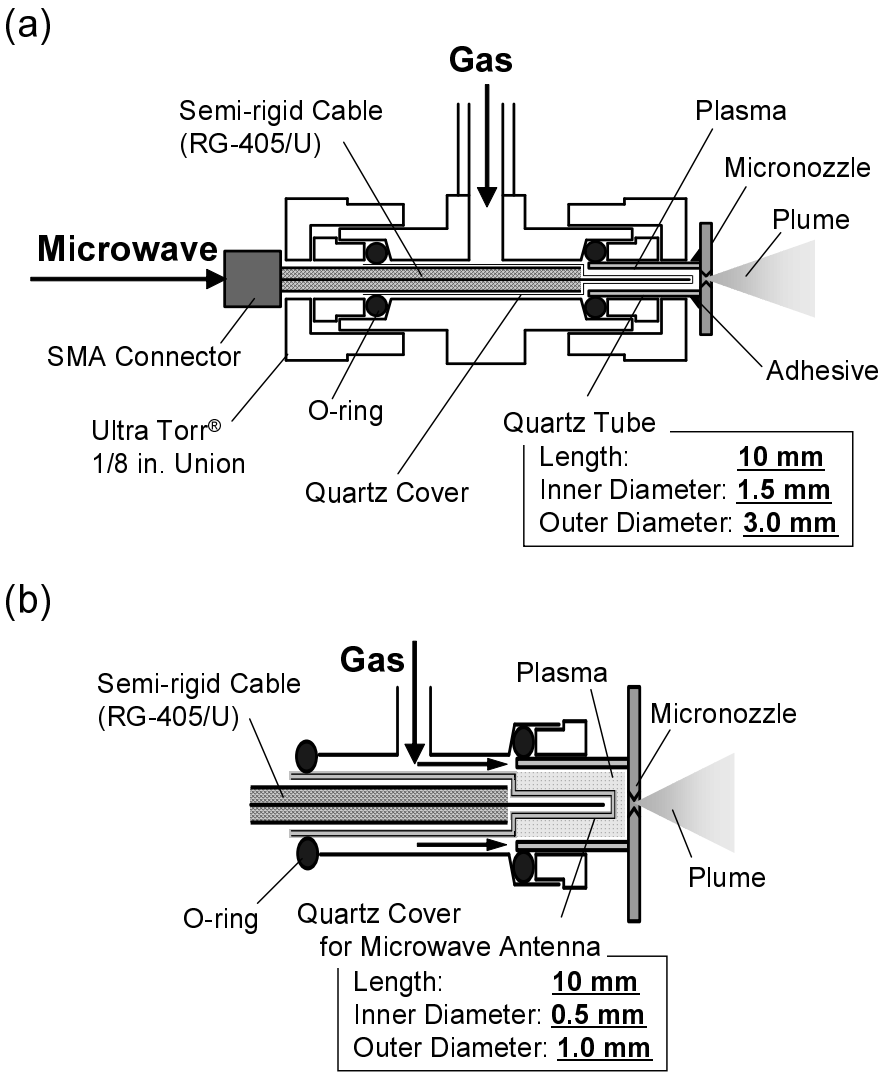

Figure 5.2: (a) Cross-sectional view of a microplasma thruster presently developed and (b) its radially enlarged view describing feed mechanism of working gases.

of the tube with a ceramic adhesive. As a microwave antenna, the center conductor of a semi-rigid coaxial cable (RG-405/U), protruding 10 mm beyond the insulator and outer conductor, is covered with a quartz tube and inserted into the plasma source to maintain the plasma, where the quartz tube is 10 mm in length, 0.5 mm in inner diameter, and 1.0 mm in outer diameter. Both the plasma source and antenna are inserted into a stainless steel Ultra-Torr vacuum fitting (Swagelok, SS-2-UT-6BT, 1/8 in. tube outer diameter), which has a single hole on its side for gas feeding. As shown in Fig. 5.2(b), both the quartz cover for the microwave antenna and the quartz tube of the plasma source are sealed with O-rings, and propellant gases flow into the plasma source through the gap between the antenna and vacuum fitting.

5.2.2 Micronozzle

The micronozzle is fabricated using a micromachining process with a diamond drill. Figures 5.3(a)–(d) show a typical example of a conical micronozzle fabricated in a quartz plate and cross-sectional and top views of three types of micronozzles taken through an optical microscope. Three micronozzles have different throat diameters and nozzle lengths with the same inlet and exit diameters to investigate dependence of its geometric difference. Here, we refer to the nozzle shown in Fig. 5.3(b) as 'ϕ200', the nozzle shown in Fig. 5.3(c) as 'ϕ120t=1', and the nozzle shown in Fig. 5.3(d) as 'ϕ120t=1.4' based on respective dimensions. ('ϕ200' has a throat diameter of 0.2 mm and a nozzle length of 1.0 mm, 'ϕ120t=1' has a throat diameter of 0.12 mm and a nozzle length of 1.0 mm, and 'ϕ120t=1.4' has a throat diameter of 0.12 mm and a nozzle length of 1.4 mm.) It should be noted that the minimum diameter of the diamond drill is 0.12 mm, so that the actual throat size of ϕ120t=1 and ϕ120t=1.4 is larger than 0.12 mm with an error of a few μm.

5.2.3 Thrust stand

Figure 5.4 shows a schematic diagram of the experimental setup for measurement of the thrust performance. Microwave signals of 4 GHz generated by an oscillator (Agilent Technologies, 8648D) are amplified through a 4-stage semiconductor amplifier, and then fed through the semi-rigid coaxial cable into the microthruster at microwave input powers of < 10 W. Working gases of Ar are also supplied to the thruster through a mass flow controller, where the plasma is generated with the help of an igniter.

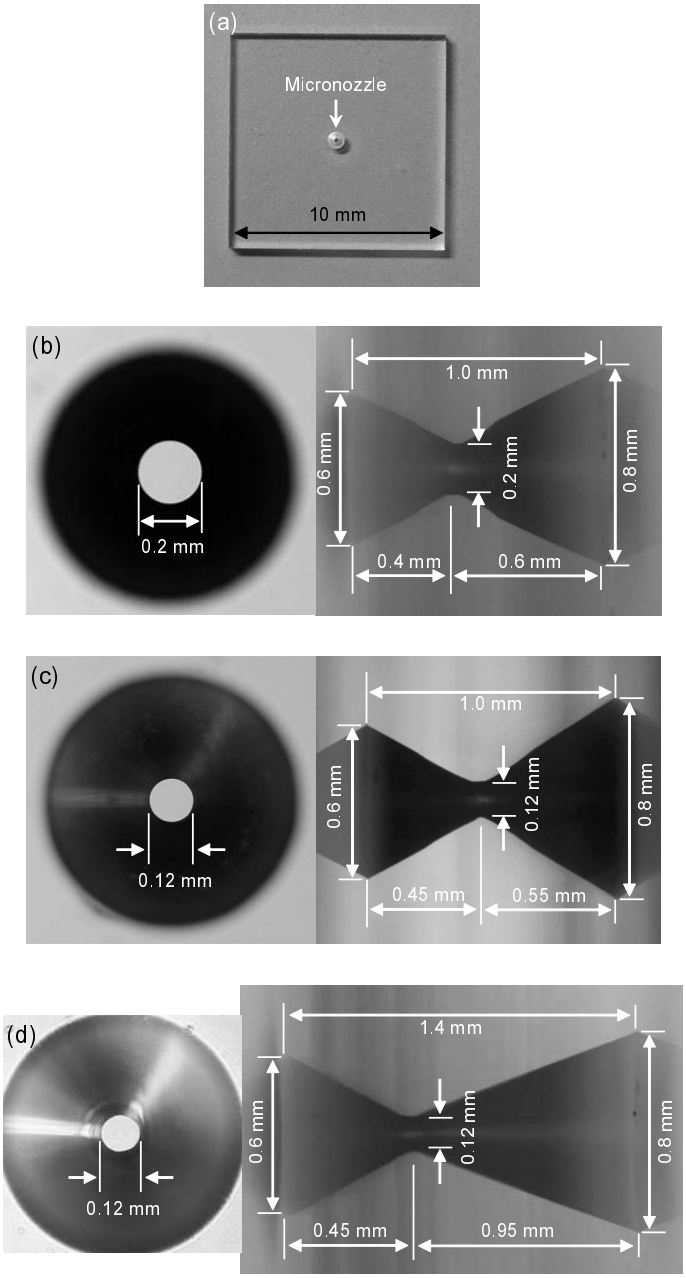

Figure 5.3: Photograph images of (a) a conical micronozzle fabricated in a quartz plate and cross-sectional and top views of three types of micronozzles: (b) throat diameter = 0.2 mm and nozzle length = 1.0 mm [ϕ200]; (c) throat diameter = 0.12 mm and nozzle length = 1.0 mm [ϕ120t=1]; and (d) throat diameter = 0.12 mm and nozzle length = 1.4 mm [ϕ120t=1.4].

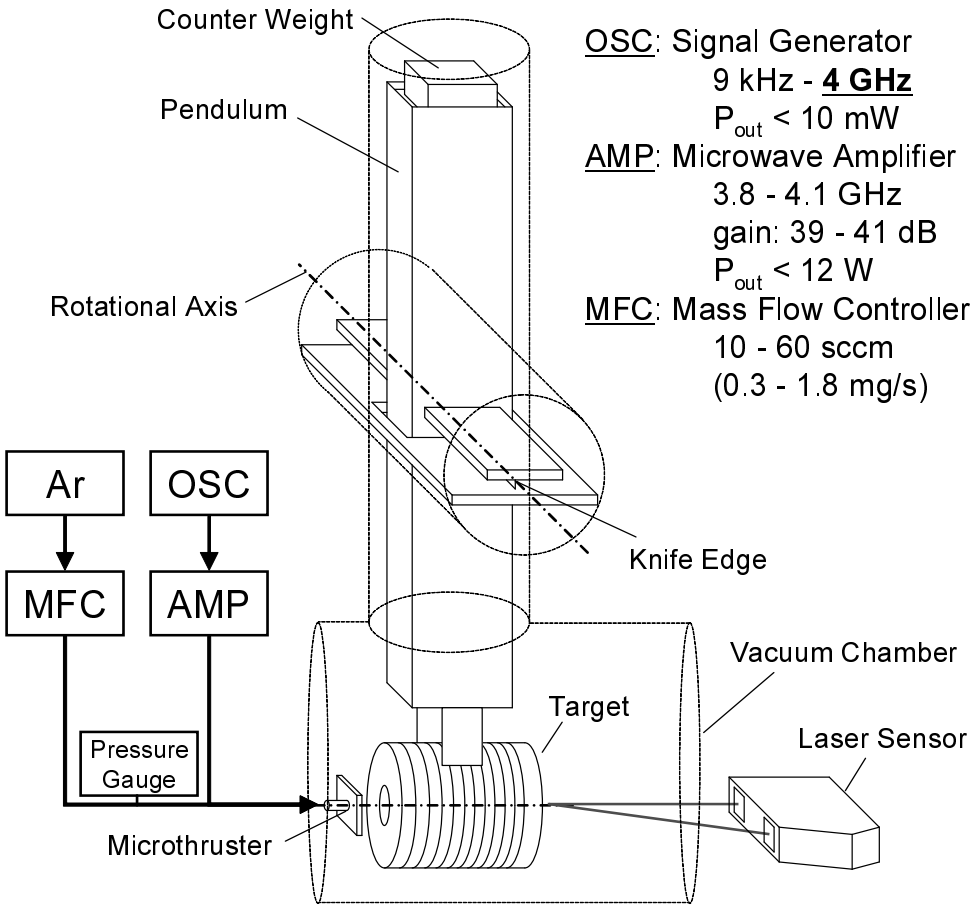

Figure 5.4: Schematic diagram of the experimental setup for thrust measurement.

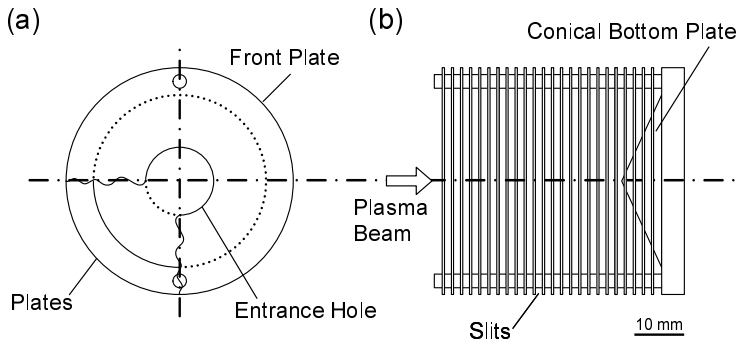

Figure 5.5: (a) Front and (b) side views of the cylindrical target. Here, the target is made of Teflon.

Here, the reflection of microwaves power is simply suppressed by adjusting the cable length. The plasma plume ejected from the thruster hits a cylindrical target. The target is mounted on one end of a pendulum while some weights are on the other end of it for balance. The pendulum rotates around fulcrums of two knife edges without friction. The displacement of the pendulum is detected by a laser sensor (KEYENCE, LK-G85), where the resolution is about $\pm$ 0.2 μm. The microthruster and pendulum are installed in a stainless-steal vacuum chamber evacuated by a rotary and turbo-molecular pump. A Bourdon tube pressure gauge, positioned between the mass flow controller and microthruster, is used for measurement of the feed gas pressure, which is assumed to be the pressure inside the microplasma source, i.e., the inlet pressure of micronozzles.

Figures 5.5(a) and (b) show front and side views of the cylindrical target, similar to the one made by Yanagi and Kimura [93]. The plasma beam comes into the target made of Teflon, through the entrance hole on the front plate. The bottom plate of the target is conically shaped, and most rebounding gas particles from the bottom plate leave radially from the target through many slits on the side of the cylinder, since the total opening area normal to the side is much larger compared to the area of the entrance hole. Thus it is expected that the effect of rebounding particles on thrust measurement is negligible with this target.

5.2.4 Method of thrust measurement

To measure the thrust performance, firstly the microthruster is mounted on the pendulum instead of the target, and then the displacement of the thruster in cold-gas operation is obtained as a function of mass flow rate with the laser sensor. The relation between the displacement and force is calibrated in advance by hanging some small weights with a thin wire of 10 μm in diameter. The weights are in the range from 12.3 to 23.5 mg. Then, the thrust in cold-gas operation is determined as a function of mass flow rate by the pendulum method. Secondly, the cylindrical target is mounted on the pendulum as shown in Fig. 5.4, and then the displacement of the target is measured as a function of mass flow rate with the laser sensor in cold-gas operation. The calibration is also carried out in a similar manner to the pendulum method, and thus the thrust in cold-gas operation is determined as a function of mass flow rate by the target method. To confirm the accuracy of the thrust measurement by the target method, we compare

the thrust obtained by the pendulum method with that obtained by the target method. After the difference between the thrust performances measured by the two methods is found to be negligible, the thrust in plasma-discharging operation is obtained by the target method.

One might imagine that it is much easier and more accurate to measure the thrust by the pendulum method in plasma-discharging operation. However, microwaves are injected into the thruster through semi-rigid or flexible coaxial cables, which are much thicker and more rigid than those for dc or rf circuits. In addition, microwaves energy is easily converted into thermal energy during propagation through coaxial cables, and thus thermal expansion of cables significantly degrades the S/N ratio during the thrust measurement.

Once the thrust F_{t} is measured, the specific impulse I_{sp} is determined using the mass flow rate $\dot{m}$ and the standard acceleration of gravity g as

$$I_{\mathrm{sp}} = \frac{F_{\mathrm{t}}}{\dot{m}g}. \tag{5.1}$$

In plasma-discharging operation, the thrust efficiency η is estimated from [102]

$$\eta = \frac{F_{\mathrm{t}}^2}{2\dot{m}P + F_0^2}, \tag{5.2}$$

where F_{t} is the thrust in plasma-discharging operation, F_0 is the thrust in cold-gas operation, and P is the microwave power absorbed in the thruster.

The thrust measurement was conducted at least five times for each experimental condition. The symbols and error bars in the figures shown below represent the average and maximum/minimum values for measurements, respectively. Notice that the error bars of the specific impulse have a tendency to become larger with decreasing mass flow rate because the relative error of the mass flow rate resulting from the accuracy of the mass flow controller is larger at lower gas flow rates.

5.2.5 Optical diagnostics

To estimate the gas temperature of the microplasma source, i.e., the reservoir temperature of the microthruster, a small amount of N_2 is added to the Ar plasma and its rotational spectra are observed. Since electrons are inefficient in providing rotational energy to molecules owing to their small mass, the population of rotational states is controlled by collisions with heavy particles. Therefore, the rotational temperature

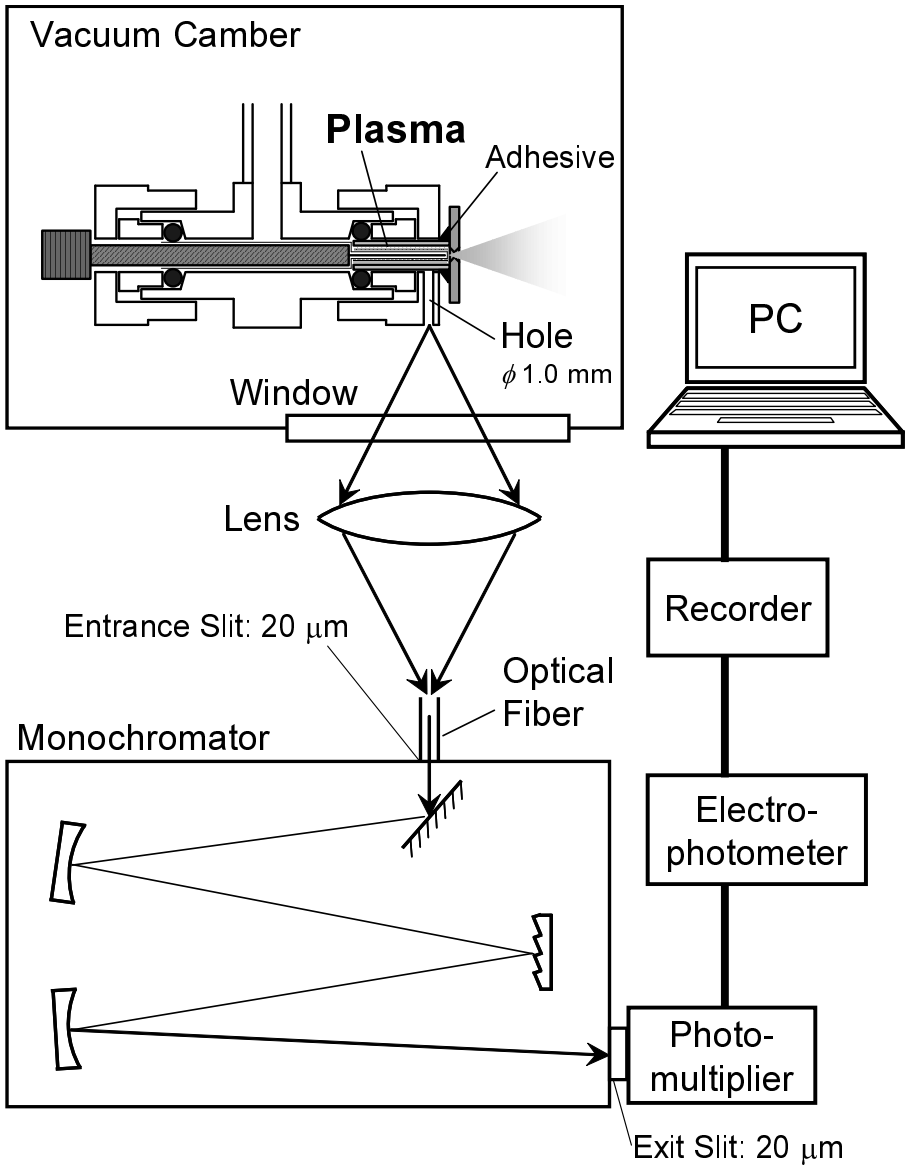

Figure 5.6: Schematic of the experimental setup for optical diagnostics of the microplasma source.

is an estimate of the heavy particle kinetic (gas) temperature. Figure 5.6 shows a schematic of the experimental setup for optical diagnostics of the microplasma source. A single hole 1.0 mm in diameter was made in the nut of the vacuum fitting. The emissions from the hole are collected by a lens and transmitted through an optical fiber to a monochromator, as in Chap. 4.

5.3 Performance testing

5.3.1 Cold-gas operation

Figures 5.7(a)–(c) show the result of a comparison of the specific impulse evaluated by the pendulum method and that evaluated by the target method in cold-gas operation for three types of micronozzles: (a) ϕ200, (b) ϕ120t=1, and (c) ϕ120t=1.4. The specific impulse is almost constant about the value of 50 s, being independent of the gas flow rate for all micronozzles, and there is little difference in specific impulses between the two methods with the difference of the values below $\pm$ 2 %. This is smaller than values of error bars, so that the accuracy of the measurement by the target method is sufficient in cold-gas operation. There are still some uncertainties in the case of plasma-discharging operation because the direct comparison can not be conducted. Nonetheless, the difference in specific impulses between the two methods could be expected to be within the error of the measurement.

Figures 5.8(a) and (b) show the thrust and specific impulse in cold-gas operation as a function of gas flow rate for three types of micronozzles: ϕ200, ϕ120t=1, and ϕ120t=1.4. Note that the specific impulse shown in Fig. 5.8(b) is the same as that obtained by the target method shown in Figs. 5.7(a)–(c). There is no significant difference in thrust performances among three types of micronozzles within the range of error bars although the average values seem to have a tendency to be larger for micronozzles with smaller throat diameters.

5.3.2 Plasma-discharging operation

Figures 5.9 (a) and (b) show photograph images of the thruster in plasma-discharging operation with the micronozzle of ϕ200 for different Ar gas flow rates of 10 sccm (0.30 mg/s) and 50 sccm (1.5 mg/s) and for different 4-GHz microwave powers from 1.9 to 4.9 W. We observed longer plasma plumes downstream of the micronozzle and

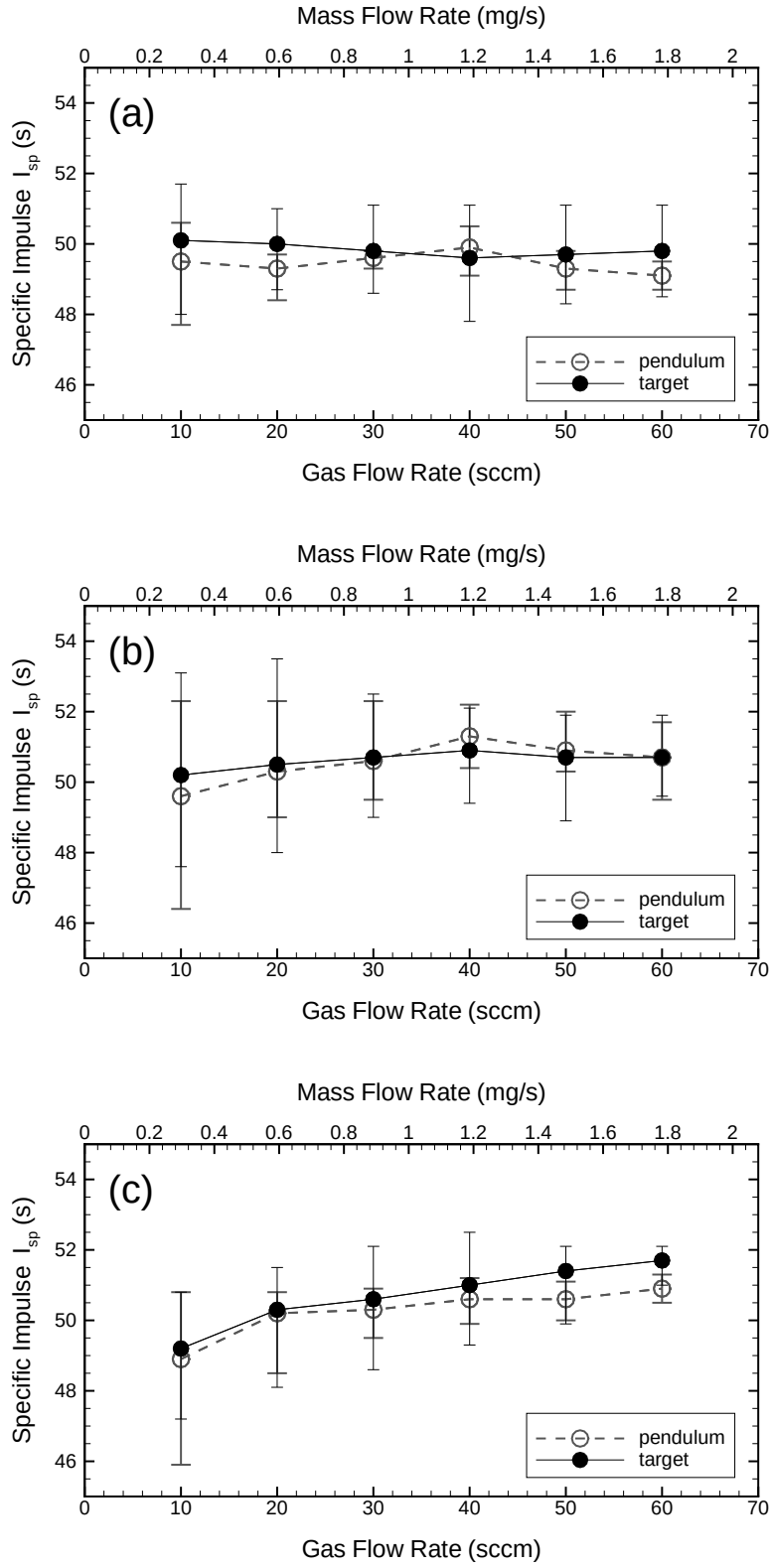

Figure 5.7: Comparison of the specific impulse evaluated by the pendulum method and that evaluated by the target method in cold-gas operation for three types of micronozzles: (a) ϕ200, (b) ϕ120t=1, and (c) ϕ120t=1.4.

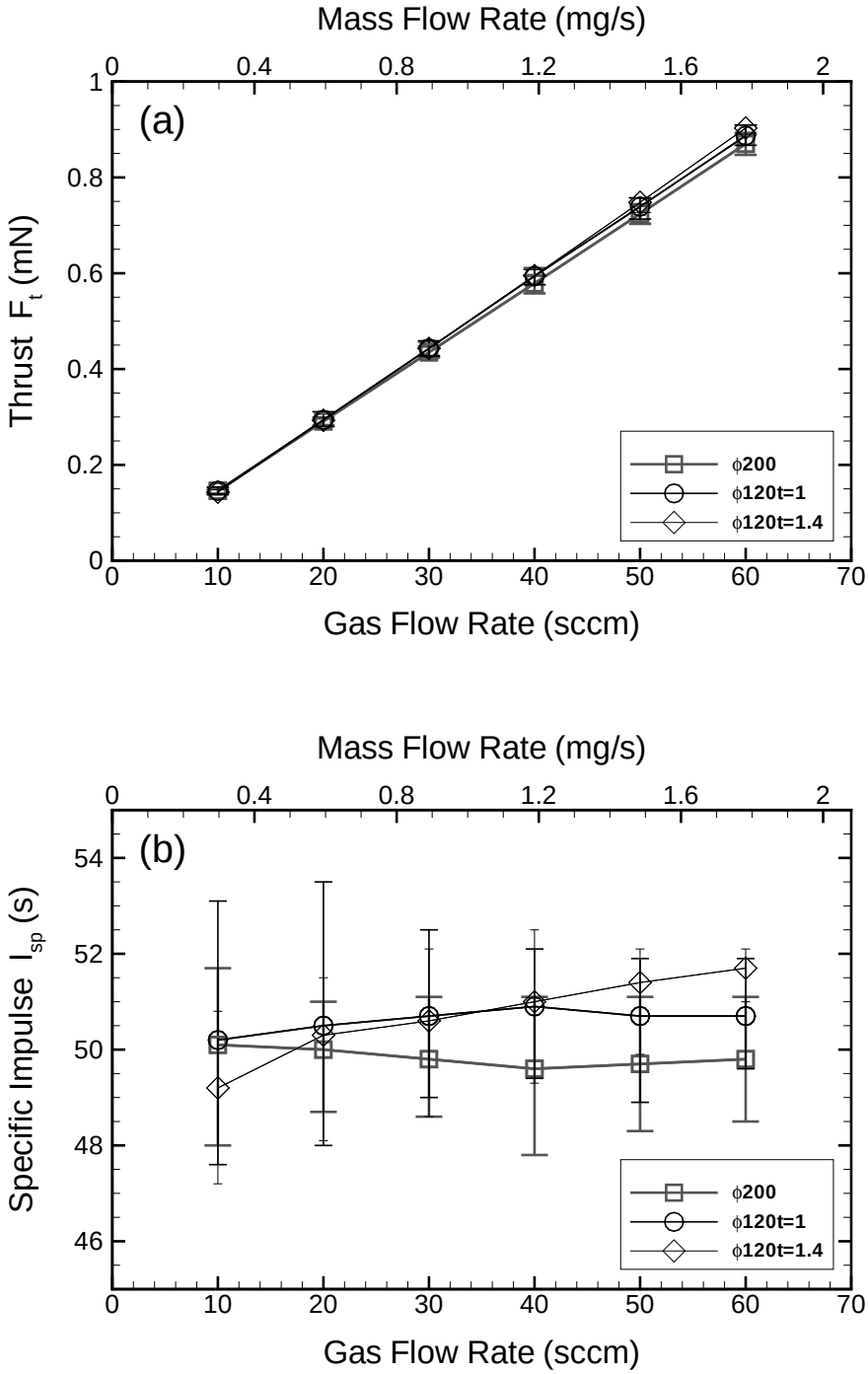

Figure 5.8: (a) Thrust and (b) specific impulse in cold-gas operation as a function of gas flow rate for three types of micronozzles: ϕ200, ϕ120t=1, and ϕ120t=1.4.

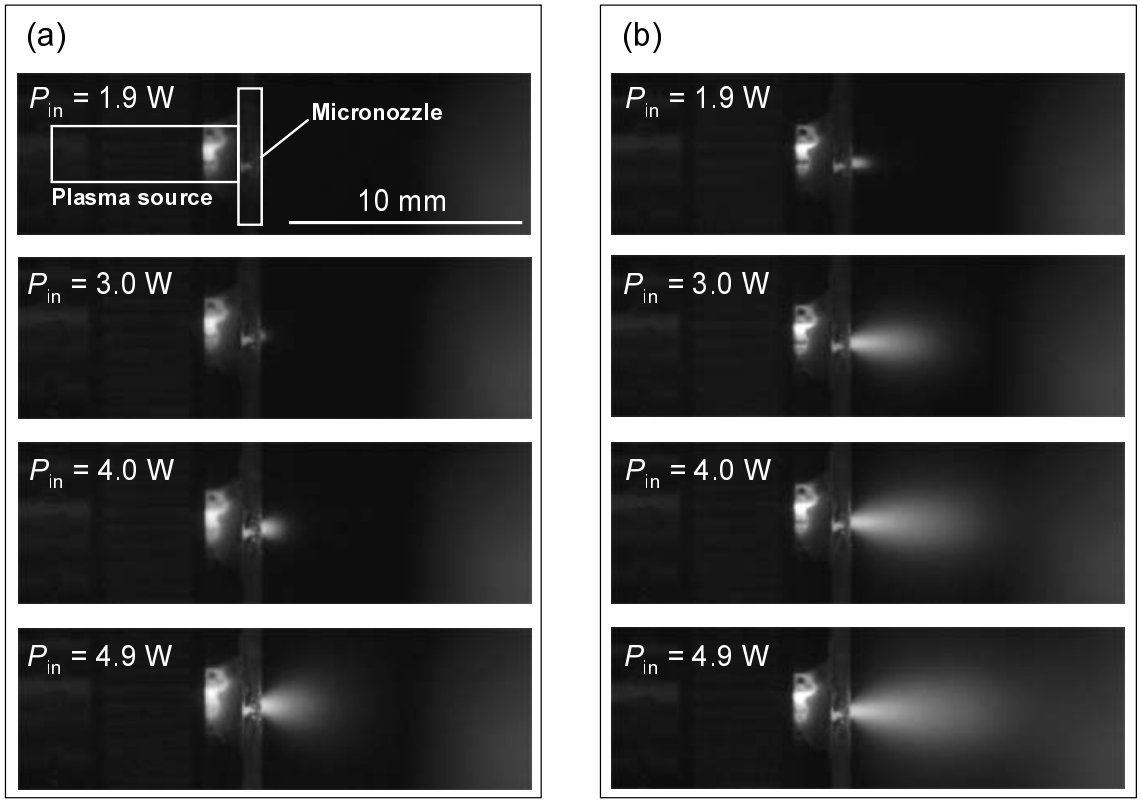

Figure 5.9: Photograph images of the thruster in plasma-discharging operation with the micronozzle of ϕ200 for different Ar gas flow rates of (a) 10 sccm (0.30 mg/s) and (b) 50 sccm (1.5 mg/s) and for different 4-GHz microwave powers from 1.9 to 4.9 W.

stronger emission intensities in the microplasma source with increasing Ar gas flow rates and microwave powers. Stable plasma discharges were also confirmed during the operation within a time span of a few tens of minutes. Moreover, the quartz cover of the microwave antenna was found to have no damage after repetitive operations in contrast to the ceramic cover employed in Chap. 4. In view of the long time operation, quartz is better than ceramic as a dielectric material of the microplasma thruster.

Figures 5.10 (a) and (b) show the thrust and specific impulse in plasma-discharging operation as a function of gas flow rate for three types of micronozzles: ϕ200, ϕ120t=1, and ϕ120t=1.4, measured at microwave powers of 3 and 6 W. The thrust and specific impulse increase with increasing gas flow rates and microwave powers. Compared with the result shown in Fig. 5.8(b), the specific impulse in plasma-discharging operation tends to increase with increasing gas flow rate. The difference in thrust performances among three nozzles is within the error bars and insignificant. In the case of a gas

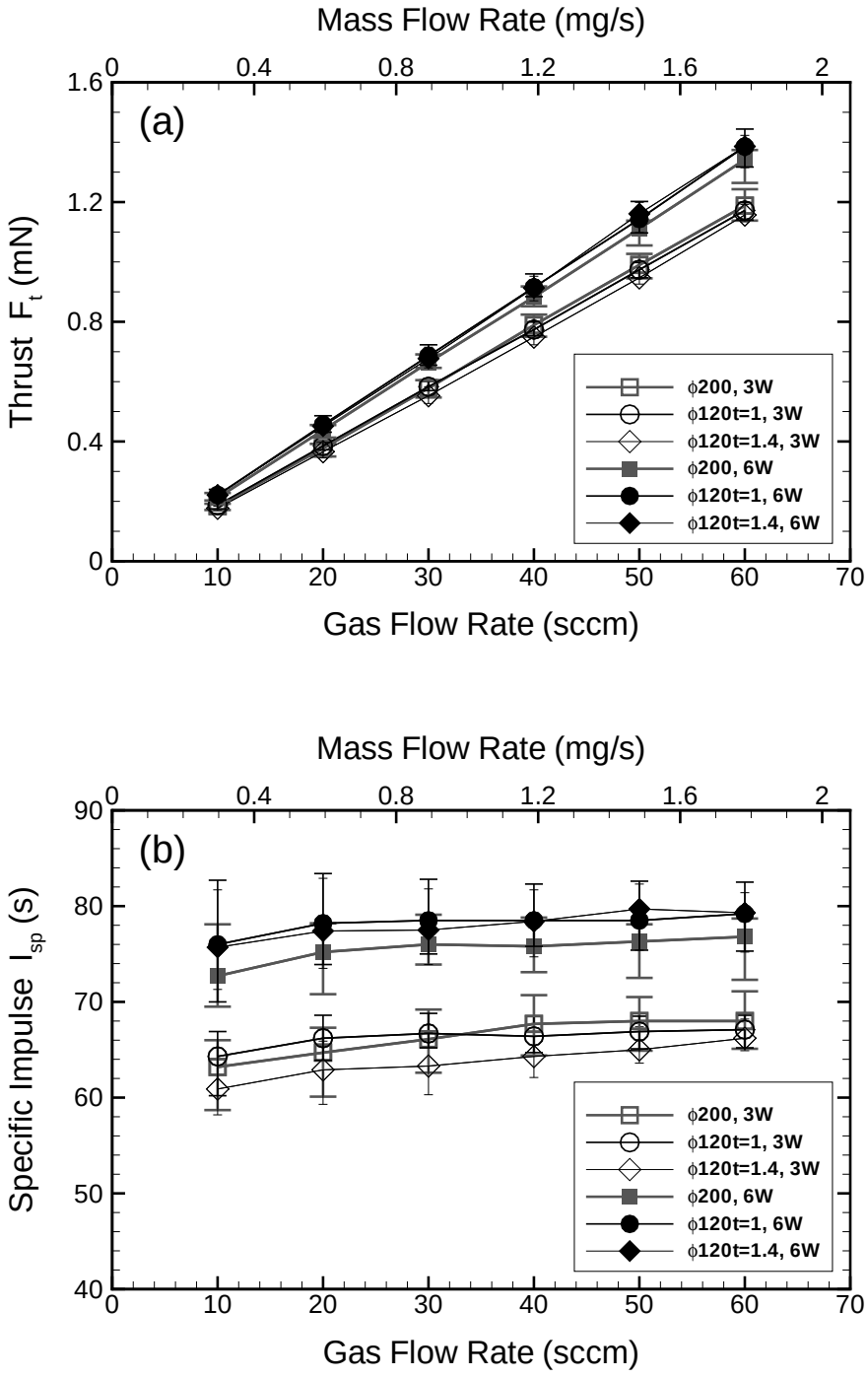

Figure 5.10: (a) Thrust and (b) specific impulse in plasma-discharging operation as a function of gas flow rate for three types of micronozzles: ϕ200, ϕ120t=1, and ϕ120t=1.4, measured at microwave powers of 3 W (open symbols) and 6 W (closed symbols).

flow rate of 60 sccm (1.8 mg/s) for the micronozzle of ϕ120t=1.4, the thrust obtained is 1.2 mN giving the specific impulse of 66 s with the thrust efficiency of 12 % at a microwave power of 3 W, and the thrust obtained is 1.4 mN giving the specific impulse of 79 s with the thrust efficiency of 8.7 % at a microwave power of 6 W, while the thrust and specific impulse are 0.9 mN and 51 s, respectively, in cold-gas operation. The thrust efficiency decreases with increasing microwave power, so that there is a trade-off between the fuel efficiency and power efficiency. Although the specific impulse obtained shows low values, the thrust obtained is on the order of mN at higher gas flow rates, which could be used for a station-keeping maneuver for microspacecraft less than 10 kg [1, 2].

5.4 Numerical model

Since it is complicated to develop a model for the entire part of the microthruster and it is expected to be a time-consuming calculation even if a complete model is developed, we focus only on the micronozzle part and have developed a simple model to compare the experimental data and numerical results. To conserve the mass flow rate more rigorously, the scheme employed in Chap. 2 is changed, being detailed in the following subsections.

5.4.1 Assumptions

To describe the plasma flow inside the micronozzle, at least a two-temperature model is generally required, which is composed of the temperature of electrons and heavy particles (neutrals and ions). However, it is impossible for the current setup to measure the electron density and temperature in the microplasma source, so that the electrons are not taken into account in the model and a calorically perfect gas is assumed. Thus, the plasma is treated as a non-ionized high-temperature gas, and the same model is employed for both cold-gas and plasma-discharging flows. Fortunately, since the particles contributing significantly to the thrust of this microthruster are not electrons but heavy particles, the effect of electrons on the flow fields could be negligible and the model would be enough to estimate macroscopic parameters, such as the thrust and specific impulse.

5.4.2 Governing equations

The equations that describe the flow field inside micronozzles are the general compressive Navier-Stokes equations. The equations can be written in a conservative form as

$$\frac{d}{dt}\iiint \boldsymbol{Q}\, dV + \iint \boldsymbol{F}_j\, dA_j = 0, \tag{5.3}$$

where $\boldsymbol{Q} = [\rho, \rho u, \rho v, E_\mathrm{t}]^t$ is the vector of conservative variables to be solved, $\boldsymbol{F}$ is the inviscid/viscous fluxes, V is the volume of a control volume, and A_k is the k-component of the area vector $\boldsymbol{A}$ of the control volume. The total energy E_t is defined as

$$E_\mathrm{t} = \rho\varepsilon + \frac{1}{2}\rho(u^2 + v^2), \tag{5.4}$$

using the density ρ, axial velocity u, radial velocity v, and internal energy $\varepsilon = c_\mathrm{v}T$, where T is the temperature and c_v is the specific heat at constant volume. The relation between the pressure p and the internal energy ε is defined as $p = (\gamma - 1)\rho\varepsilon$ with the ratio of specific heats $\gamma = 5/3$ for Ar. To evaluate the viscosity, Sutherland's law is used, i.e., the viscosity μ is obtained from

$$\mu = \mu_0 \frac{T_0 + C}{T + C}\left(\frac{T}{T_0}\right)^{3/2}, \tag{5.5}$$

where $\mu_0 = 22.3 \times 10^{-6}$ Pa s and $T_0 = 293.15$ K are reference values at standard sea level conditions and $C = 142$ K is Sutherland's constant for Ar [63]. Once the viscosity is obtained, the thermal conductivity κ can be calculated from

$$\kappa = \mu \frac{c_\mathrm{p}}{P_r}, \tag{5.6}$$

where $P_r = 2/3$ is the Prandtl number for Ar and c_p is the specific heat at constant pressure.

5.4.3 Finite volume formulation

The Navier-Stokes equations are discretized by a finite volume approach, where a cell-centered scheme is employed, so that all flow properties are defined at center of the control volume. For a conventional numerical scheme, one transfers the equation system from Cartesian coordinates (x, y, z) to cylindrical coordinates (r, θ, z) and set the azimuthal derivatives $\partial/\partial\theta$ to zero. This results in an equation set composed of two-dimensional equations and additional source terms which represent the axisymmetric

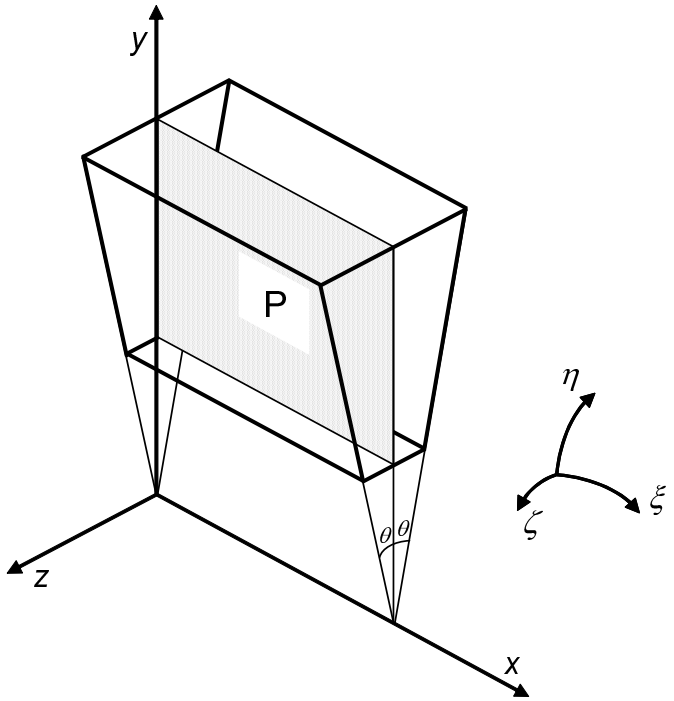

Figure 5.11: Quasi three-dimensional control volume depicted with thick lines. The physical properties P are all defied at the center of the each computational mesh. The equation system is transformed from the physical domain (x, y, z) to computational domain (ξ, η, ζ). We have assumed here $\theta \ll 1$.

effect. In the present computation, instead of using above approach, we discretized the governing equations in a three-dimensional fashion for an infinitely thin control volume under the axisymmetric assumption. The quasi three-dimensional control volume is shown in Fig. 5.11. The equation system is transformed from the physical domain (x, y, z) to computational domain (ξ, η, ζ) and discretized in the same manner as Cartesian mesh. The discretization is described in Ref. [103]. The advantage of this discretization is that the scheme becomes rigorously conservative.

5.4.4 Integration scheme

The inviscid fluxes at the cell boundary are evaluated using the Modified Advection Upstream Splitting Method by Pressure-based Weight Function (AUSM-PW+) scheme [104]. The space accuracy is kept to second order by the Monotone Upstream-centered Scheme for Conservation Laws (MUSCL) interpolation method [105]. For the viscous term, the usual central-average representation is used at the cell interface, so

that all the diffusive terms are discretized in a central-difference fashion. Time integration is performed implicitly by Lower-Upper Symmetric Gauss Seidel (LU-SGS) method since it is robust and efficient [106]. The steady state solution is obtained as an asymptotic solution of the unsteady equations for large time.

5.4.5 Boundary conditions

At the inlet, the flow is assumed to be subsonic and hence one flow variable should be determined from the interior region. In cold-gas operation, the inlet temperature T_{in} is set at 300 K and the same mass flow rate $\dot{m}$ is given as the experimental condition. The radial velocity is set to be zero, and the axial velocity is obtained by extrapolation from the downstream point adjacent to the inlet [63, 70]. The inlet density ρ_{in} is obtained from the mass flow rate and the axial velocity, giving the static pressure p_{in} from the equation of state: $p_{\text{in}} = \rho_{\text{in}} R T_{\text{in}}$ with gas constant R for Ar. In plasma-discharging operation, since the inlet temperature can not be determined directly in the experiment, the static pressure is given to the system, which is assumed to be equal to the pressure obtained from the pressure gauge. Here, the pressure has an error of $\pm$ 1 kPa because the Bourdon tube pressure gauge is used for the inlet pressure measurement, the minimum scale of which is 10 kPa. The other inlet conditions are set in a similar manner to cold-gas operation. At the nozzle wall, an isothermal-wall (T_{wall} = 300 K) and non-slip ($u = v = 0$) conditions are employed. At the nozzle exit, the flow velocity is supersonic for most part, but reduces to subsonic inside the boundary layer. In subsonic cases, one flow property should be determined outside the nozzle, and hence small pressure value is specified at that point. In turn, if the flow is supersonic, all flow properties are obtained from the zeroth extrapolation. Along the symmetric axis, the radial velocity component v is set at the opposite sign to the adjacent value, and other properties are set equal to the corresponding adjacent values.

5.5 Comparison with numerical analysis

5.5.1 Configuration

Figures 5.12(a)–(c) show cross-sectional view and computational grids for three types of micronozzles: ϕ200, ϕ120t=1, and ϕ120t=1.4, which are formed based on the nozzle configuration shown in Figs. 5.3(b)–(d). The simulation area of each nozzle is divided

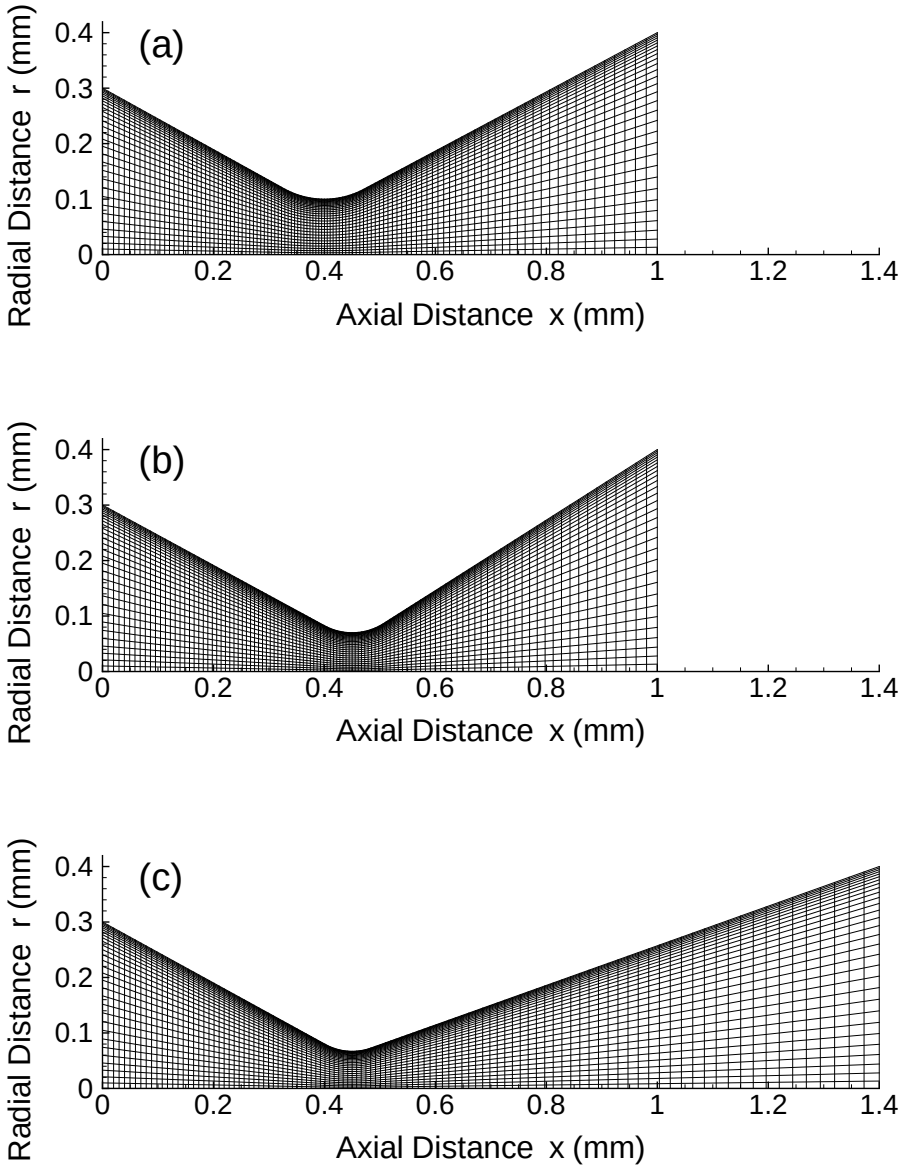

Figure 5.12: Cross-sectional view and computational grids for three types of micronozzles: (a) ϕ200, (b) ϕ120t=1, and (c) ϕ120t=1.4. The simulation area of each nozzle is divided into 110 cells in the axial direction and 30 cells in the radial direction.

into 110 cells in the axial direction and 30 cells in the radial direction with the grid spacing being finer near the throat and the nozzle wall.

5.5.2 Inlet pressure

The diameter of the micronozzle throat has a large effect on the flow properties. However, the direct measurement of the throat size of micronozzles can not be conducted to an accuracy of 1 μm. To determine the throat diameter, several calculations with different throat sizes were performed for each micronozzle in cold-gas operation, and compared the calculated inlet pressure with the pressure measured by the Bourdon tube pressure gauge. Figure 5.13 shows the result of comparison of the measured inlet pressure and calculated inlet pressure for three types of micronozzles: ϕ200, ϕ120t=1, and ϕ120t=1.4. The error bars of the experimental data are due to the scale of the Bourdon tube pressure gauge. The numerical results are in good agreement with the experimental data. From these results, the throat diameters of three micronozzles are determined to be 0.2 mm, 0.14 mm, and 0.134 mm for ϕ200, ϕ120t=1, and ϕ120t=1.4, respectively.

5.5.3 Cold-gas operation

Figures 5.14(a) and (b) show the thrust and specific impulse in cold-gas operation as a function of gas flow rate, calculated for three types of micronozzles: ϕ200, ϕ120t=1, and ϕ120t=1.4. Here, the thrust F_t and specific impulse I_sp are defined as

$$F_\mathrm{t} = 2\pi \int_0^{r_\mathrm{ex}} (\rho u^2 + p)\, r dr, \tag{5.7}$$

$$I_\mathrm{sp} = F_\mathrm{t} \left(g\, 2\pi \int_0^{r_\mathrm{ex}} \rho u\, r dr \right)^{-1} = \frac{F_\mathrm{t}}{\dot{m} g}, \tag{5.8}$$

where r_ex is the exit radius of the nozzle [70]. The thrust increases monotonically with increasing gas flow rate, where the difference among three nozzles can hardly be detected. The specific impulse indicates a constant value of about 53 s, being independent of the gas flow rate for all micronozzles. Moreover, micronozzles with smaller throat diameters give slightly larger specific impulses in numerical analysis. This tendency is consistent with the experimental data shown in Figs. 5.8(a) and (b) although the numerical values are larger than the experimental ones.

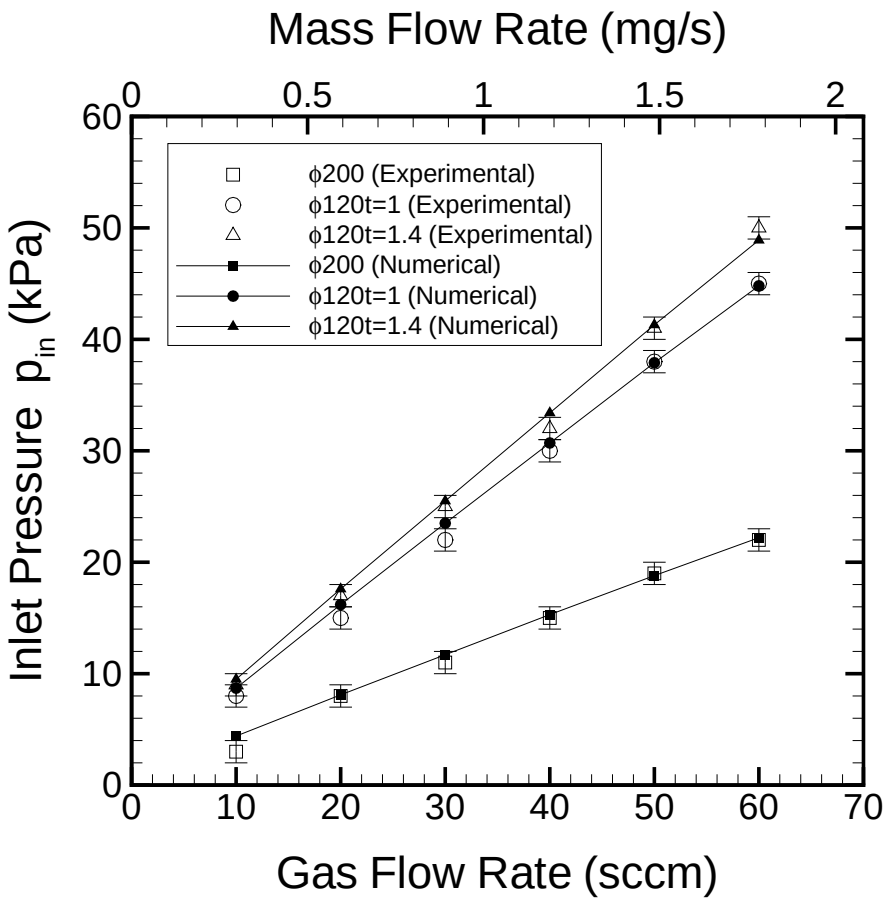

Figure 5.13: Comparison of the measured inlet pressure and calculated inlet pressure in cold-gas operation for three types of micronozzles: ϕ200, ϕ120t=1, and ϕ120t=1.4.

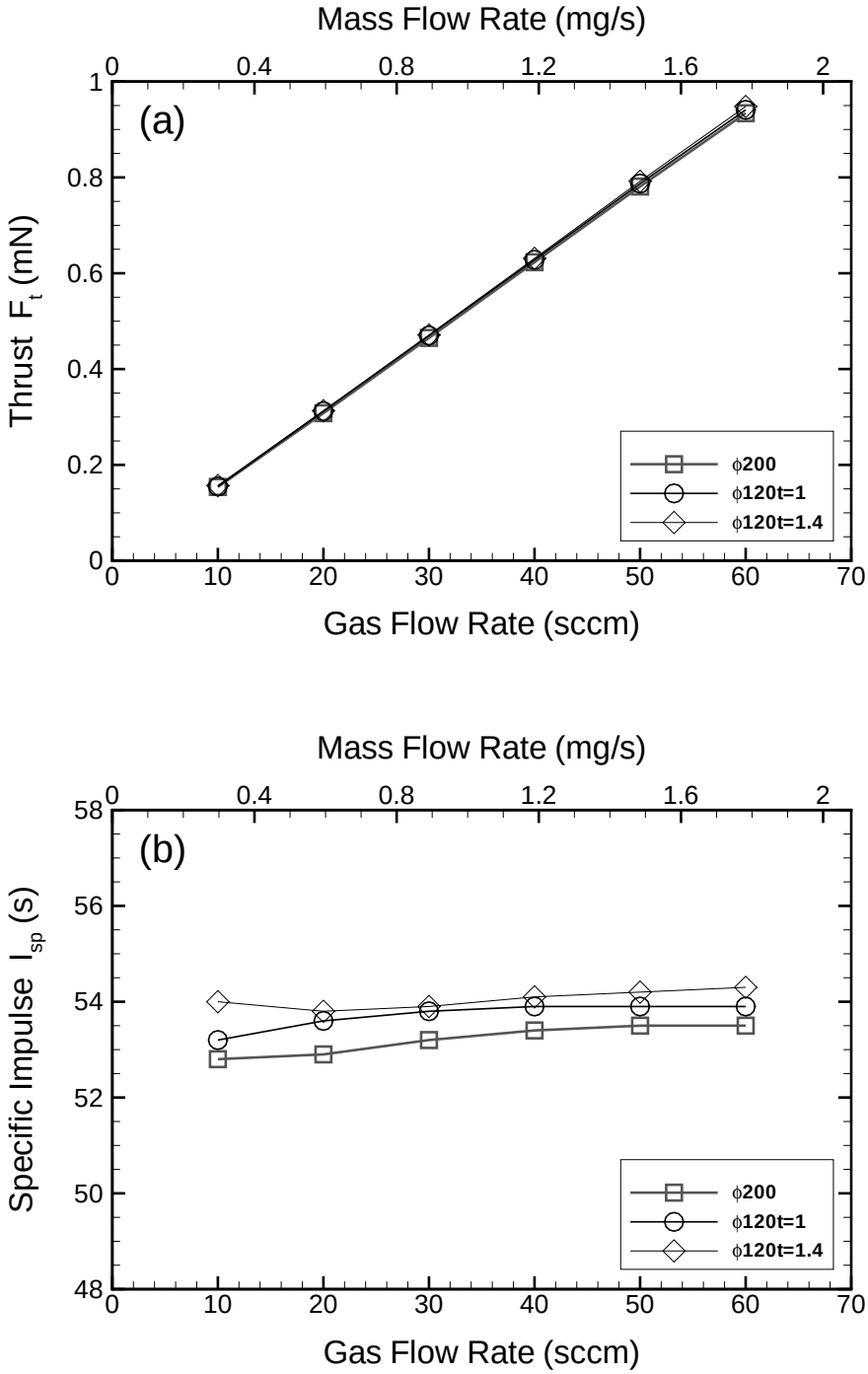

Figure 5.14: Calculated (a) thrust and (b) specific impulse in cold-gas operation as a function of gas flow rate for three types of micronozzles: ϕ200, ϕ120t=1, and ϕ120t=1.4.

Figure 5.15 shows the result of a comparison of the measured specific impulse and calculated specific impulse in cold-gas operation for the micronozzle of ϕ120t=1.4. Here, using the following thrust F_{t}', the specific impulse I_{sp}' is defined as

$$F_{\mathrm{t}}' = 2\pi \int_0^{r_{\mathrm{ex}}} \rho u^2 \, r dr, \tag{5.9}$$

$$I_{\mathrm{sp}}' = F_{\mathrm{t}}' \left(g \, 2\pi \int_0^{r_{\mathrm{ex}}} \rho u \, r dr \right)^{-1} = \frac{F_{\mathrm{t}}'}{\dot{m} g}. \tag{5.10}$$

It is noted that F_{t}' is the momentum thrust only whereas F_{t} in Eq. (5.7) consists of the momentum and pressure thrust. As shown in the figure, while the specific impulse I_{sp}' increases dramatically with increasing gas flow rate, the specific impulse I_{sp} remains almost constant, which is in good agreement with the experimental result. This result can be found in the flow fields inside the micronozzle in Figs. 5.16(a) and (b), showing the Mach number contours at Ar gas flow rates of 10 and 60 sccm. Although at both gas flow rates the significant boundary layers are confirmed, the layer at a gas flow rate of 10 sccm is much thicker than that at 60 sccm. Moreover, the maximum Mach number is observed inside the micronozzle, not at the exit for 10 sccm flows. Since the thicker boundary layers impede the flow expansion at lower gas flow rates, the nozzle flow is heavily under-expanded and higher pressures are obtained at the nozzle exit. Increasing the gas flow rate, in turn, alleviates this effect, leading to larger flow velocities and lower pressures at the nozzle exit. These two effects compensate each other, resulting in the almost constant specific impulse in cold-gas operation. We thus conclude that the pressure thrust significantly contributes to the total thrust at lower gas flow rates for the microthruster as indicated in Chap. 2.

5.5.4 Plasma-discharging operation

To calculate the thrust performance in plasma-discharging operation, the nozzle inlet pressure is required. As described in boundary conditions, the inlet pressure p_{in} is assumed to be equal to the pressure measured by the Bourdon tube pressure gauge. Table 5.1 summarizes the pressure measured at different conditions for three types of micronozzles: ϕ200, ϕ120t=1, and ϕ120t=1.4. Using these pressures and mass flow rates as nozzle inlet conditions, we calculated the thrust and specific impulse in plasma-discharging operation at microwave powers of 3 and 6 W for three micronozzles; the results are shown in Figs. 5.17(a) and (b), where the error bars are derived from the

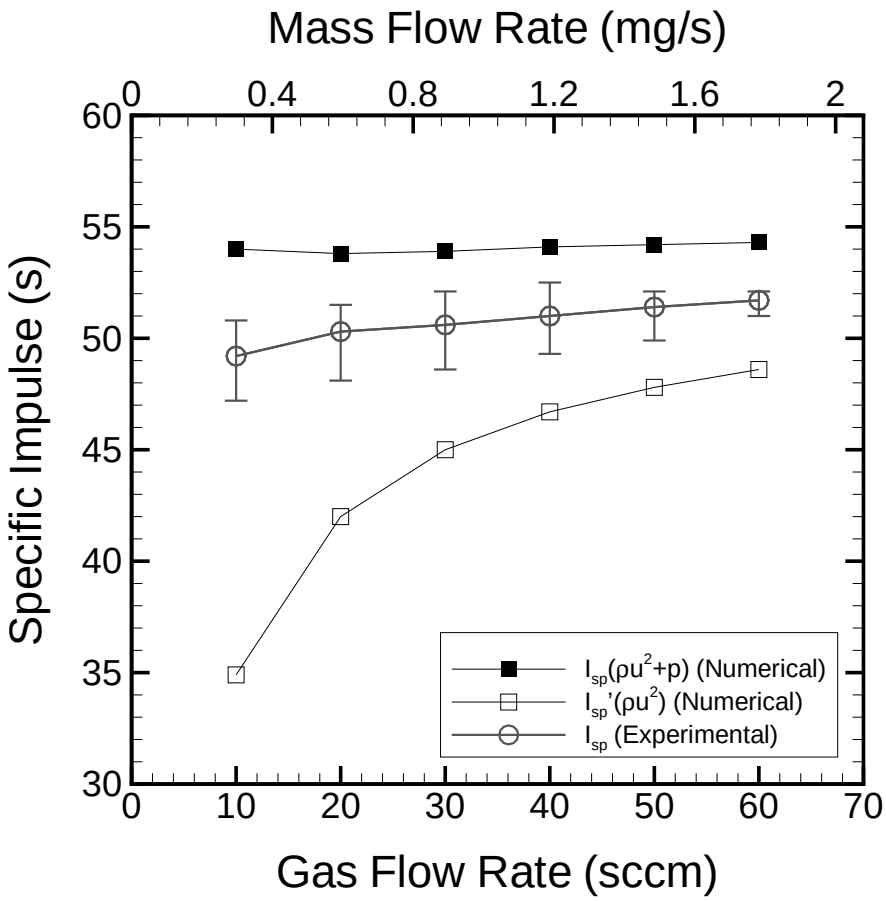

Figure 5.15: Comparison of the measured specific impulse and calculated specific impulse in cold-gas operation for the micronozzle of ϕ120t=1.4. Here, to take into account the effect of the pressure thrust, two types of the specific impulse are employed. The one ($I_{\rm sp}$) is derived from the thrust consisting of the momentum and pressure thrust while the other ($I'_{\rm sp}$) is derived from the thrust consisting of the momentum thrust only.

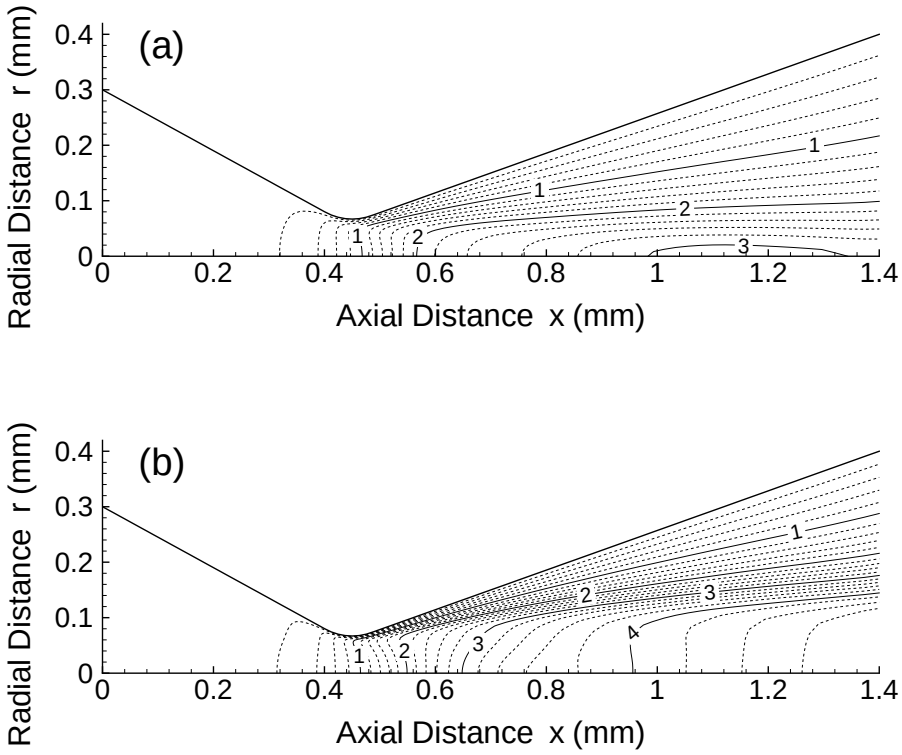

Figure 5.16: Mach number contours in cold-gas operation for the micronozzle of ϕ120t=1.4 at Ar gas flow rates of (a) 10 sccm (0.30 mg/s) and (b) 60 sccm (1.8 mg/s).

Table 5.1: Inlet pressure p_{in} measured by the Bourdon tube pressure gauge at microwave powers of 3 and 6 W for different gas flow rates from 10 to 60 sccm and for three types of micronozzles: (a) ϕ200, (b) ϕ120t=1, and (c) ϕ120t=1.4. Here, the pressure has an error of ± 1 kPa because of the minimum scale of the pressure gauge.

	(a) ϕ200		(b) ϕ120t=1		(c) ϕ120t=1.4	
	3 W	6 W	3 W	6 W	3 W	6 W
Ar (sccm)	p_{in} (kPa)	p_{in} (kPa)	p_{in} (kPa)	p_{in} (kPa)	p_{in} (kPa)	p_{in} (kPa)
10	5 ± 1	6 ± 1	10 ± 1	12 ± 1	11 ± 1	13 ± 1
20	10 ± 1	12 ± 1	20 ± 1	24 ± 1	22 ± 1	27 ± 1
30	15 ± 1	18 ± 1	30 ± 1	36 ± 1	33 ± 1	40 ± 1
40	20 ± 1	24 ± 1	40 ± 1	48 ± 1	44 ± 1	54 ± 1
50	25 ± 1	30 ± 1	50 ± 1	60 ± 1	55 ± 1	67 ± 1
60	30 ± 1	36 ± 1	60 ± 1	71 ± 1	66 ± 1	79 ± 1

error of the pressure p_{in}. The thrust performances increase with increasing gas flow rates and microwave powers. The difference among three micronozzles is also found to be within the error bars and insignificant; this result is consistent with the experiment shown in Figs. 5.10(a) and (b). However, the specific impulse is underestimated at lower gas flow rates while it is overestimated at higher gas flow rates in comparison to the experiment. The degree of this discrepancy becomes larger at lower gas flow rates. At lower gas flow rates in plasma-discharging operation, the Reynolds number becomes smaller than that in cold-gas operation because of higher viscosities due to the increase in temperature. For micronozzle flows at low Reynolds numbers, it appears that the direct simulation Monte Carlo (DSMC) method gives more accurate results for macroscopic performance characteristics [107]. Since it is time-consuming to use the DSMC method for the part from the inlet through the throat, it would be better to employ a combined Navier-Stokes/DSMC approach [108]. In addition, a new approach to measure the thrust performance in plasma-discharging operation is required to obtain experimental results more accurately. These are left for future work.

5.5.5 Dependence of wall conditions

The numerical analysis has been conducted using the isothermal wall ($T_{\mathrm{wall}} = 300$ K) condition so far. However, there is no means of knowing the wall condition directly. To investigate the effect of nozzle wall conditions, the calculation was also conducted using the adiabatic wall condition. Figure 5.18 shows the calculated inlet temperatures T_{in} under the adiabatic and isothermal wall conditions for the micronozzle of ϕ120t=1.4 at a microwave power of 6 W, together with the rotational temperature of the microplasma source measured at the same conditions by optical emission spectroscopy as shown in Fig. 5.6. Here, the inlet temperature is obtained at the nozzle inlet on the symmetric axis, i.e., at the origin of the computational grids shown in Fig. 5.12(c). While the inlet temperature increases with increasing gas flow rate under the adiabatic wall condition, the temperature decreases under the isothermal wall condition. The rotational temperature, which should be close to the nozzle inlet temperature, also decreases with increasing gas flow rate, and the tendency is similar to that under the isothermal wall condition. Note that the wall condition does not have a significant effect on the thrust performance. Because the microwave power is fixed at 6 W, that is, the power per unit mass flow rate decreases with increasing gas flow rate, it

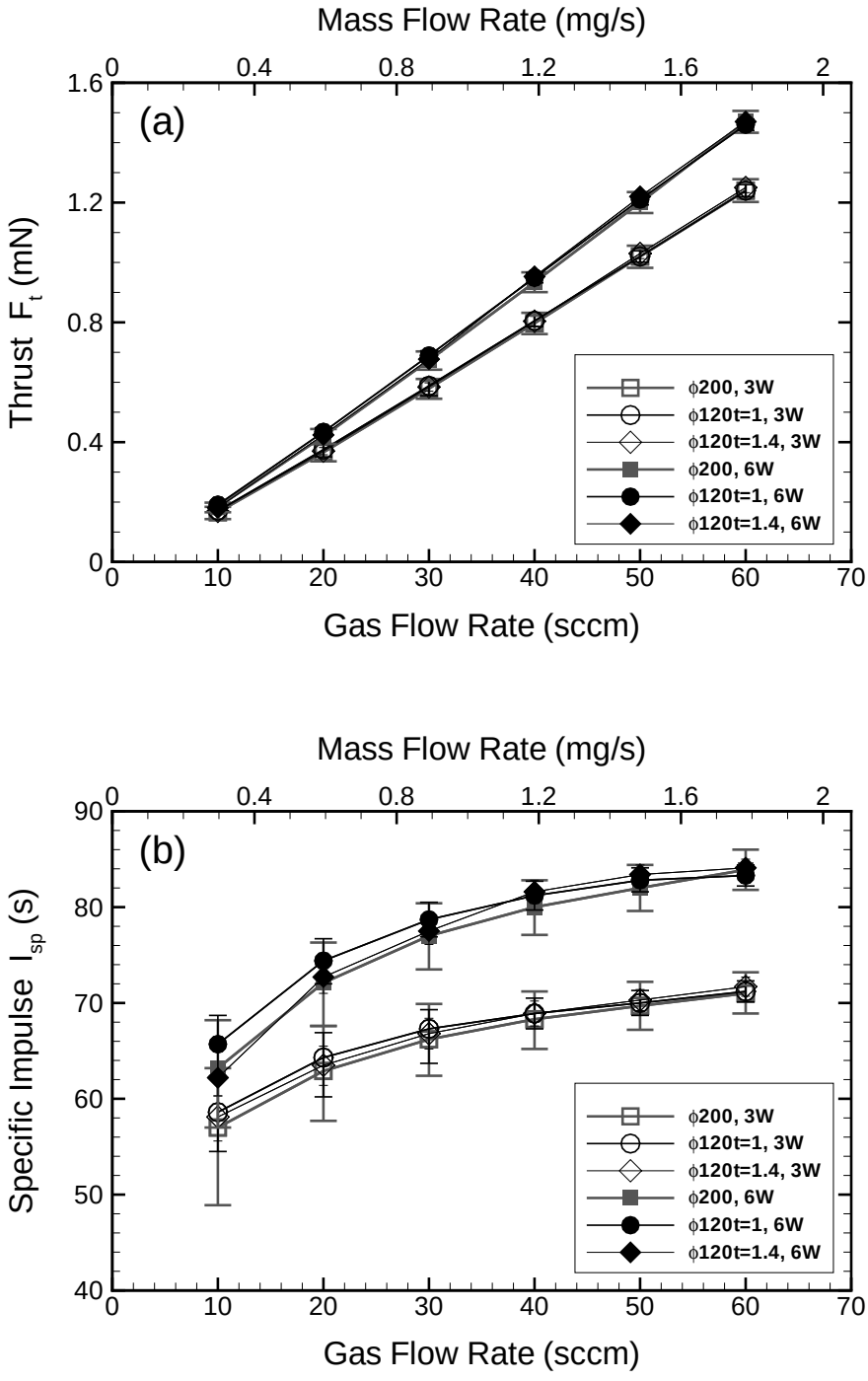

Figure 5.17: Calculated (a) thrust and (b) specific impulse in plasma-discharging operation as a function of gas flow rate at microwave powers of 3 W (open symbols) and 6 W (closed symbols) for three types of micronozzles: ϕ200, ϕ120t=1, and ϕ120t=1.4. Here, the error bars are derived from the error of the inlet pressure p_{in} measured by the Bourdon tube pressure gauge.

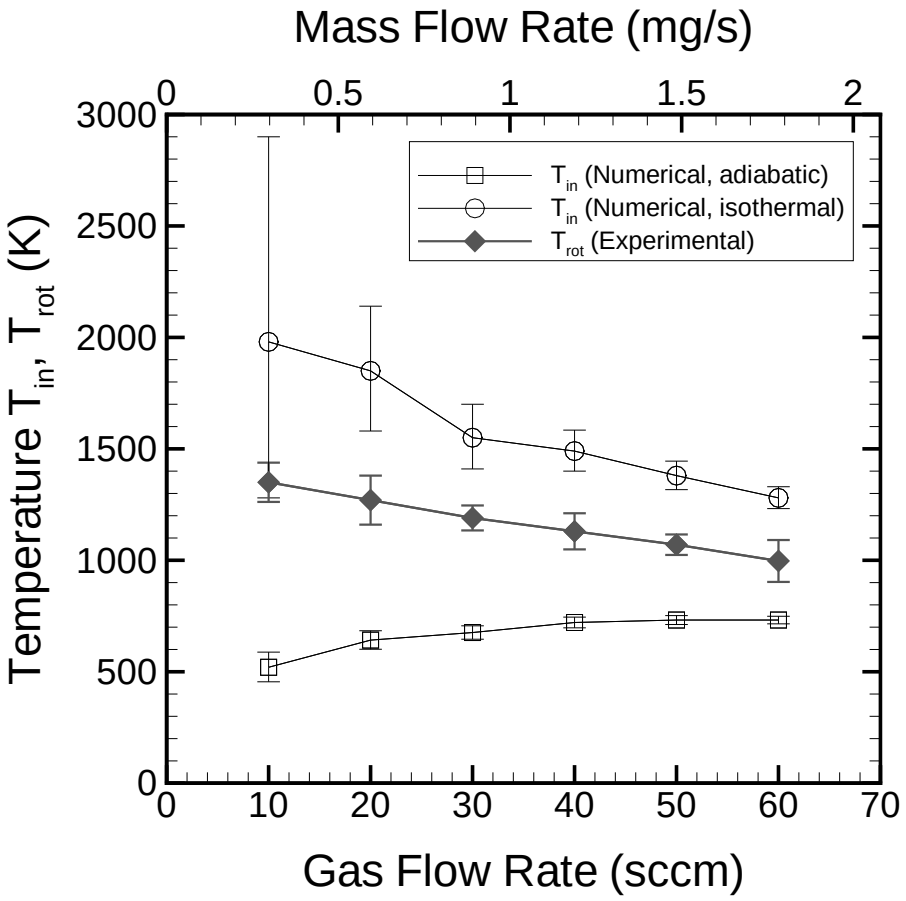

Figure 5.18: Comparison of the calculated inlet temperatures T_{in} under the adiabatic and isothermal wall conditions and the measured rotational temperature T_{rot} (N_2) of the microplasma source for the micronozzle of ϕ120t=1.4 at a microwave power of 6 W. Here, the error bars of the simulation are derived from the error of the inlet pressure p_{in} measured by the Bourdon tube pressure gauge, and the error bars of the experiment show the maximum/minimum values for five times measurements.

is reasonable that the gas temperature should decrease with increasing gas flow rate. The micronozzle is fabricated in a quartz plate, which has much larger area compared with the micronozzle as shown in Fig. 5.3(a), so that the quartz plate seems to play a role as a kind of heat sink although the quartz has a low thermal conductivity. The nozzle wall condition is important because the flow properties are heavily affected by the condition as discussed in Chap. 2. The result obtained here would be useful for more precise simulation.

5.6 Conclusions

A microplasma thruster has been developed, consisting of a cylindrical microplasma source 10 mm long and 1.5 mm in inner diameter and a conical micronozzle 1.0–1.4 mm long with a throat 0.12–0.2 mm in diameter. The propellant gas employed is Ar at pressures of 10–100 kPa, and the plasma is established by 4-GHz microwave powers of < 10 W. Stable plasma discharges are confirmed during the thruster operation within a time span of a few tens of minutes.

The thrust performance has been measured by a combination of target and pendulum methods, being compared with numerical analysis based on the general compressive Navier-Stokes equations. The thrust performance is improved by discharging the plasma; in the case of gas flow rates of 10–60 sccm (0.30–1.8 mg/s), the thrust obtained is 0.18–1.2 mN giving the specific impulse of 61–66 s with the thrust efficiency of 1.7–12 % at a microwave power of 3 W, and the thrust is 0.22–1.4 mN giving the specific impulse of 76–79 s with the thrust efficiency of 1.4–8.7 % at a microwave power of 6 W, while the thrust and specific impulse are 0.14–0.9 mN and 50–51 s, respectively, in cold-gas operation. The thrust performance indicates that the microplasma thruster could be used for a station-keeping maneuver for microspacecraft less than 10 kg. Note that the difference in thrust performances among three different micronozzles developed can hardly be detected in both the experiment and simulation.

A comparison with numerical analysis demonstrates that the pressure thrust contributes significantly to the total thrust at lower gas flow rates for the microthruster owing to the viscous loss in the thick boundary layers of the micronozzle, which is consistent with the results in Chap. 2. Moreover, comparing the experiment and simulation implies that the micronozzle tends to have an isothermal wall rather than an

adiabatic one because of the nozzle fabrication in a large quartz plate, which seems to play a role as a kind of heat sink. Since the distribution of flow properties is heavily affected by the wall conditions, the implication would be useful for more precise simulation of micronozzle flows.

6
Conclusions

6.1 Concluding remarks

In this study, a miniature electrothermal thruster using microwave-excited microplasmas has been presented. The microthruster consists of a microplasma source and a micronozzle, where the inner radius and length of the plasma source are about 1 and 10 mm, respectively, and the length of the nozzle is about 1 mm with a throat diameter about 0.2 mm. The microplasma source is composed of a cylindrical dielectric tube, the outside of which is covered with a grounded metal. Microwaves are injected into the plasma chamber, and then the propellant gas of Ar is ionized and heated up in the pressure range from 10 to 100 kPa. Such high thermal energy is converted into kinetic energy through the micronozzle, and then the thrust is produced.

In Chap. 2, we have performed numerical investigations of the microplasma source and the micronozzle flow separately for a microwave power of interest ($\leq$ 10 W). (i) In the microplasma source analysis, microwave powers absorbed in the plasma tend to increase with increasing microwave frequency f (= 1–25 GHz) and dielectric constant $\varepsilon_{\rm d}$ (= 3.8, 9.2, and 20). The plasma density, electron temperature, and heavy particle temperature obtained are in the range 2.7×10^{19}–1.7×10^{22} m^{-3}, 7.9×10^{3}–1.0×10^{4} K, and 9.5×10^{2}–1.0×10^{4} K, respectively. A comparison with the theoretical dispersion relation indicates that to absorb the microwave power effectively, at least one

wavelength is required to occur in the plasma chamber, e.g., over $f = 5$ GHz at $\varepsilon_{\mathrm{d}} = 20$. Under such conditions, the plasma is sustained by surface waves, where the absorbed power reaches local peaks at a certain combination of the frequency and permittivity owing to the geometric structure of microplasma sources. (ii) In the micronozzle flow analysis, the flow is found to be very lossy because of high viscosity in thick boundary layers, resulting in the fact that shortening the nozzle length enhances the thrust more effectively than providing as much power as possible. Such viscous effect is less significant under conditions in order of adiabatic, radiative, and isothermal walls. The thrust performances calculated are thrusts of 2.5–3.5 mN and specific impulses of 130–180 s at a mass flow rate of 2.0 mg/s. Notice that the flow rarefaction has little effect on the thrust performance.

In Chap. 3, a miniature microwave-sustained plasma source has been fabricated and its characteristics have been preliminarily investigated by optical emission spectroscopy. Depending on the microwave power and Ar gas flow rate, plasma discharges inside the quartz tube 10 mm long and 1.5 mm in inner diameter using 4-GHz microwaves show a sudden shift of emission intensities with a slight hysteresis. This result implies that a mode change occurs in the microplasma source, being apparently due to whether the plasma density is above the surface-wave resonance density or to the existence of different patterns of standing waves in the plasma source. Lower flow rates can easily maintain the high-intensity mode at lower applied powers. However, the reflected microwave power is found to be unfavorably large.

In Chap. 4, a miniature plasma source has been improved; the plasma source is composed of a quartz tube 10 mm long and 1.5 mm in diameter and a microwave rod antenna 10 mm long covered with a ceramic tube, resulting in reduction of the reflected microwave power below 5 %. Plasma diagnostics, consisting of optical emission spectroscopy and an electrostatic probe measurement, show that the emission intensity, electron density, and rotational temperature increases with the increase in incident microwave power, microwave frequency, and dielectric constant of ceramic tubes. The microplasma source produces the electron densities of 10^{17}–10^{19} m^{-3} and the rotational temperatures of 700–1800 K in the range of microwave powers 2–10 W at an Ar gas flow rate of 50 sccm. Since the rotational temperature, which should be close to the gas temperature, increases from the upstream toward the exit of the plasma chamber where a micronozzle will be equipped, the microplasma source is found to be desirable in the

microthruster. Assuming that the rotational temperature equals the gas temperature, numerical analysis indicates that reducing the throat diameter of micronozzles could produce better thrust performances.

In Chap. 5, a conical micronozzle has been fabricated in a 1.0–1.4 mm thick quartz plate with a throat diameter of 0.12–0.2 mm using a micromachining process with a diamond drill, being joined to the microplasma source with a ceramic adhesive. Then, performance testing of the microplasma thruster has been conducted and compared with numerical analysis. The thrust and specific impulse obtained are 1.4 mN and 79 s, respectively, with the thrust efficiency of 8.7 % at an Ar gas flow rate of 60 sccm (1.8 mg/s) and an input power of 6 W, while the thrust is 0.9 mN with the specific impulse of 51 s in cold-gas operation. A comparison with numerical analysis indicates that the effect of the pressure thrust is not negligible at lower gas flow rates for the microthruster, and implies that the micronozzle tends to have an isothermal wall rather than an adiabatic one; this implication would be useful for more precise simulation of micronozzle flows.

Although numerical results overestimate the thrust performance, the thrust level measured in the experiment indicates that the microplasma thruster can reduce the propellant mass more than 30 % compared with a cold-gas thruster in the case of the NSSK for microspacecraft of 10 kg.

6.2 Future work

From an academic viewpoint, there are several interesting points to be investigated. Throughout the thesis, numerical analysis has been conducted separately for the microplasma source and the micronozzle flow. As described in Chap. 3, the flow has a significant effect on plasma discharges, so that flow dynamics should be taken into account for numerical analysis of the microplasma source and both the plasma source and nozzle flow are to be calculated altogether.

Because of the low resolution of the monochromator employed, the electron density inside the microplasma source can not be measured. A more precise monochromator can recognize the Stark broadening of the H_β line by adding a small amount of H_2 to the microplasma source, resulting in measurement of the plasma density. A comparison with the theoretical dispersion relation could clarify whether this microplasma is

generated by surface waves or not.

Moreover, Ar has been used as a working gas for simplicity of analysis in this study. However, other propellants which have high constant-pressure specific heat, such as hydrogen, should be employed for better thrust performances in the case of the practical use of this microthruster. In view of the storage problem, solid or liquid propellant would be taken into account, so that water (H_2O) could be a good candidate for the future microplasma thruster [109].

References

[1] J. Mueller, *Proc. 33rd AIAA/ASME/SAE/ASEE Joint Propulsion Conf.*, Seattle, WA, 1997 (American Institute of Aeronautics and Astronautics) Paper AIAA-97-3058.

[2] J. Mueller, *Micropropulsion for Small Spacecraft*, ed. M. M. Micci and A. D. Ketsdever (American Institute of Aeronautics and Astronautics, Reston, 2000) Chap. 3.

[3] S. W. Janson, *Proc. 30th AIAA/ASME/SAE/ASEE Joint Propulsion Conf.*, Indianapolis, IN, 1994 (American Institute of Aeronautics and Astronautics) Paper AIAA-94-2998.

[4] D. J. Barnhart, T. Vladimirova, and M. N. Sweeting, *Proc. CANEUS 2006 Conf.*, Toulouse, France, 2006 (American Society of Mechanical Engineers) Paper CANEUS2006-11045.

[5] N. Yamamoto, H. Kataharada, T. Chikaoka, H. Masui, H. Nakashima, and Y. Takao, *Proc. 29th Int. Electric Propulsion Conf.*, Princeton, NJ, 2005, Paper IEPC-2005-036.

[6] R. Wirz, R. Sullivan, J. Przybylowski, and M. Silva, *Proc. 42nd AIAA/ASME/SAE/ASEE Joint Propulsion Conf.*, Sacramento, CA, 2006 (American Institute of Aeronautics and Astronautics) Paper AIAA-2006-4498.

[7] V. Khayms and M. Martinez-Sanchez, *Micropropulsion for Small Spacecraft*, ed. M. M. Micci and A. D. Ketsdever (American Institute of Aeronautics and Astronautics, Reston, 2000) Chap. 9.

[8] T. Ito and M. A. Cappelli, *Appl. Phys. Lett.* **89** (2006) 061501.

[9] S. Marcuccio, A. Genovese, and M. Andrenucci, *J. Propul. Power* **14** (1998) 774.

[10] M. Tajmar, A. Genovese, and W. Steiger, *J. Propul. Power* **20** (2004) 211.

[11] A. Genovese, M. Tajmar, N. Buldrini, and W. Steiger, *J. Propul. Power* **20** (2004) 219.

[12] M. Gamero-Castaño and V. Hruby, *J. Propul. Power* **17** (2001) 977.

[13] M. S. Alexander, J. Stark, K. L. Smith, B. Stevens, and B. Kent, *J. Propul. Power* **22** (2006) 620.

[14] D. H. Simon and H. B. Land III, *Proc. 40th AIAA/ASME/SAE/ASEE Joint Propulsion Conf.*, Fort Lauderdale, FL, 2004 (American Institute of Aeronautics and Astronautics) Paper AIAA-2004-3622.

[15] R. L. Bayt, A. A. Ayon, and K. S. Breuer, *Proc. 33rd AIAA/ASME/SAE/ASEE Joint Propulsion Conf.*, Seattle, WA, 1997 (American Institute of Aeronautics and Astronautics) Paper AIAA-97-3169.

[16] D. H. Lewis, Jr., S. W. Janson, R. B. Cohen, and E. K. Antonsson, *Sensors and Actuators* A **80** (2000) 143.

[17] C. Rossi, D. Briand, M. Dumonteuil, T. Camps, P. Q. Phamb, and N. F. de Rooij, *Sensors and Actuators* A **126** (2006) 241.

[18] J. Blandino, M. McDevitt, J. Mueller, D. Bame, and A. Green, *J. Propul. Power* **22** (2006) 677.

[19] Z. Ahmed, S. F. Gimelshein, and A. D. Ketsdever, *J. Propul. Power* **22** (2006) 749.

[20] H. Horisawa, T. Noda, K. Onodera, and I. Kimura, *Proc. 41st AIAA/ASME/SAE/ASEE Joint Propulsion Conf.*, Tucson, AZ, 2005 (American Institute of Aeronautics and Astronautics) Paper AIAA-2005-4075.

[21] H. Horisawa, K. Onodera, T. Noda, and I. Kimura, *Proc. 42nd AIAA/ASME/SAE/ASEE Joint Propulsion Conf.*, Sacramento, CA, 2006 (American Institute of Aeronautics and Astronautics) Paper AIAA-2006-4496.

[22] C. Phipps and J. Luke, *AIAA J.* **40** (2002) 310.

[23] H. Koizumi, T. Inoue, K. Kojima, K. Mori, K. Komurasaki, and Y. Arakawa, *Proc. 39th AIAA/ASME/SAE/ASEE Joint Propulsion Conf.*, Huntsville, AL, 2003 (American Institute of Aeronautics and Astronautics) Paper AIAA-2003-4568.

[24] M. Martinez-Sanchez and J. E. Pollard, *J. Propul. Power* **14** (1998) 688.

[25] K. Terashima, L. Howald, H. Haefke, and H. Guntherodt, *Thin Solid Films* **281–282** (1996) 634.

[26] H. Yoshiki and Y. Horiike, *Jpn. J. Appl. Phys.* **40** (2001) L360.

[27] K. Taniguchi, T. Fukasawa, H. Yoshiki, and Y. Horiike, *Jpn. J. Appl. Phys.* **42** (2003) 6584.

[28] J. Hopwood, O. Minayeva, and Y. Yin, *J. Vac. Sci. Technol.* B **18** (2000) 2446.

[29] T. Ito and K. Terashima, *Appl. Phys. Lett.* **80** (2002) 2648.

[30] E. Stoffels, A. J. Flikweert, W. W. Stoffels, and G. M. W. Kroesen, *Plasma Sources Sci. Technol.* **11** (2002) 383.

[31] A. M. Bilgic, U. Engel, E. Voges, M. Kückelheim, and J. A. C. Broekaert, *Plasma Sources Sci. Technol.* **9** (2000) 1.

[32] A. Kono, T. Sugiyama, T. Goto, H. Furuhashi, and Y. Uchida, *Jpn. J. Appl. Phys.* **40** (2001) L238.

[33] F. Iza and J. A. Hopwood, *IEEE Trans. Plasma Sci.* **31** (2003) 782.

[34] F. Iza and J. A. Hopwood, *IEEE Trans. Plasma Sci.* **32** (2004) 498.

[35] F. Iza and J. A. Hopwood, *IEEE Trans. Plasma Sci.* **33** (2005) 306.

[36] J. Kim and K. Terashima, *Appl. Phys. Lett.* **86** (2005) 191504.

[37] V. Karanassios, *Spectrochim. Acta, Part B* **59** (2004) 909.

[38] K. H. Becker, K. H. Schoenbach, and J. G. Eden, *J. Phys. D* **39** (2006) R55.

[39] M. Moisan and Z. Zakrzewski, *J. Phys. D* **24** (1991) 1025.

[40] H. Sugai, I. Ghanashev, and M. Nagatsu, *Plasma Sources Sci. Technol.* **7** (1998) 192.

[41] I. Ganachev and H. Sugai, *Surf. Coat. Technol.* **174**–**175** (2003) 15.

[42] M. A. Lieberman and A. J. Lichtenberg, *Principles of Plasma Discharges and Materials Processing* (Wiley-Interscience, New York, 1994).

[43] C. Lee and M. A. Lieberman, *J. Vac. Sci. Technol.* A **13** (1995) 368.

[44] S. Ashida, C. Lee, and M. A. Lieberman, *J. Vac. Sci. Technol.* A **13** (1995) 2498.

[45] S. Panda, D. J. Economou, and M. Meyyappan, *J. Appl. Phys.* **87** (2000) 8323.

[46] E. J. Tonnis and D. B. Graves, *J. Vac. Sci. Technol.* A **20** (2002) 1787.

[47] Y. Ikeda, J. P. Verboncoeur, P. J. Christenson, and C. K. Birdsall, *J. Appl. Phys.* **86** (1999) 2431.

[48] H. Kousaka and K. Ono, *Jpn. J. Appl. Phys.* **41** (2002) 2199.

[49] H. Kousaka and K. Ono, *Plasma Sources Sci. Technol.* **12** (2003) 273.

[50] S. Kuchi-ishi and M. Nishida, *Proc. 26th Int. Electric Propulsion Conf.*, Kitakyushu, Japan, 1999, p. 193, Paper IEPC-99-029.

[51] S. Kuchi-ishi and M. Nishida, *Proc. 26th Int. Electric Propulsion Conf.*, Kitakyushu, Japan, 1999, p. 310, Paper IEPC-99-044.

[52] G. V. Candler and R. W. MacCormack, *Proc. 26th Aerospace Sciences Meeting*, Reno, NV, 1988 (American Institute of Aeronautics and Astronautics) Paper AIAA-88-0511.

[53] V. A. Godyak and N. Sternberg, *IEEE Trans. Plasma Sci.* **18** (1990) 159.

[54] A. Grainer, C. Boisse-Laporte, P. Leprince, J. Marec, and P. Nghiem, *J. Phys. D* **20** (1987) 204.

[55] M. Zethoff and U. Kortshagen, *J. Phys. D* **25** (1992) 1574.

[56] Y. Bartosiewicz, P. Proulx, and Y. Mercadier, *J. Phys. D* **35** (2002) 2139.

[57] M. Mitchner and C. H. Kruger, Jr., *Partilally Ionized Gases* (Wiley-Interscience, New York, 1973).

[58] M. I. Hoffert and H. Lien, *Phys. Fluids* **10** (1967) 1769.

[59] J. J. Beulens, D. Milojevic, D. C. Shram, and P. M. Vallinga, *Phys. Fluids* B **3** (1991) 2548.

[60] O. B. Minayeva and J. Hopwood, *J. Appl. Phys.* **94** (2003) 2821.

[61] F. P. Incropera and D. P. DeWitt, *Fundamentals of Heat and Mass Transfer* (Wiley-Interscience, New York, 1996).

[62] K. S. Yee, *IEEE Trans. Antennas Propagat.* **14** (1966) 302.

[63] J. D. Anderson, Jr., *Computational Fluid Dynamics: The Basics with Applications* (McGraw-Hill, New York, 1995).

[64] S. V. Patankar, *Numerical Heat Transfer and Fluid Flow* (McGraw-Hill, New York, 1980).

[65] J. Mostaghimi, P. Proulx, and M. I. Boulos, *J. Appl. Phys.* **61** (1987) 1753.

[66] J. Mostaghimi and M. I. Boulos, *J. Appl. Phys.* **68** (1990) 2643.

[67] H. Tahara, T. Yonezawa, Y. Andoh, and T. Yoshikawa, *IEEE Trans. Plasma Sci.* **26** (1998) 1307.

[68] V. K. Liau, M. T. C. Fang, J. D. Yan, and A. I. Al-Shamma'a, *J. Phys. D* **36** (2003) 2774.

[69] G. Mur, *IEEE Trans. Electromagn. Compat.* **23** (1981) 377.

[70] S. C. Kim, *J. Spacecr. Rockets* **31** (1994) 259.

[71] D. H. Manzella, P. F. Penko, K. J. De Witt, and T. G. Keith Jr., *J. Propul. Power* **5** (1989) 452.

[72] Y. Takao, K. Ono, K. Takahashi, and Y. Setsuhara, *Thin Solid Films* **506–507** (2006) 592.

[73] H. Kokura, K. Nakamura, I. Ganashev, and H. Sugai, *Jpn. J. Appl. Phys.* **38** (1999) 5262.

[74] A. W. Trivelpiece and R. W. Gould, *J. Appl. Phys.* **30** (1959) 1784.

[75] I. Ghanashev, H. Sugai, S. Morita, and N Toyoda, *Plasma Sources Sci. Technol.* **8** (1999) 363.

[76] J. Park, I. Henins, H. W. Herrmann, and G. S. Selwyn, *J. Appl. Phys.* **89** (2001) 15.

[77] Z. Yu, K. Hoshimiya, J. D. Williams, S. F. Polvinen, and G. J. Collins, *Appl. Phys. Lett.* **83** (2003) 854.

[78] A. D. Ketsdever, *Micropropulsion for Small Spacecraft*, ed. M. M. Micci and A. D. Ketsdever (American Institute of Aeronautics and Astronautics, Reston, 2000) Chap. 4.

[79] C. Rossi, M. D. Rouhani, and D. Estève, *Sensors and Actuators* A **87** (2000) 96.

[80] H. W. Liepmann and A. Roshko, *Elements of Gasdynamics* (Wiley, New York, 1957) Chap. 2.

[81] G. P. Sutton and O. Biblarz, *Rocket Propulsion Elements* (Wiley-Interscience, New York, 2001) Chap. 3.

[82] M. Gad-el-Hak, *The MEMS Handbook*, ed. M. Gad-el-Hak (CRC Press, New York, 2002) Chap. 4.

[83] I. D. Boyd, G. Chen, and G. V. Candler, *Phys. Fluids* **7** (1995) 210.

[84] M. Tuda and K. Ono, *J. Vac. Sci. Technol.* A **16** (1998) 2832.

[85] M. Tuda, K. Ono, H. Ootera, M. Tsuchihashi, M. Hanazaki, and T. Komemura, *J. Vac. Sci. Technol.* A **18** (2000) 840.

[86] V. M. Zakharova, Yu. M. Kgan, K. S. Mustafin, and V. I. Perel, *Zh. Tekhn. Fiz.* **30** (1960) 411.

[87] Y. Takao and K. Ono, *Plasma Sources Sci. Technol.* **15** (2006) 211.

[88] J. O. Arnold, E. E. Whiting, and G. C. Lyle, *J. Quant. Spectrosc. Radiant. Transfer.* **9** (1969) 775.

[89] E. E. Whiting, J. O. Arnold, and G. C. Lyle, *NASA TN* D-5088 (1969).

[90] D. M. Phillips, *J. Phys. D* **9** (1976) 507.

[91] R. G. Jahn, *Physics of Electric Propulsion* (McGraw-Hill, New York, 1968).

[92] R. Goldstein and F. N. Mastrup, *AIAA J.* **4** (1966) 99.

[93] R. Yanagi and I. Kimura, *J. Spacecr. Rockets* **19** (1982) 246.

[94] J. A. Burkhart, *J. Spacecr. Rockets* **8** (1971) 240.

[95] T. W. Haag, *Rev. Sci. Instrum.* **62** (1991) 1186.

[96] A. Sasoh and Y. Arakawa, *Rev. Sci. Instrum.* **64** (1993) 719.

[97] S. Orieux, C. Rossi, and D. Estève, *Rev. Sci. Instrum.* **73** (2002) 2694.

[98] T. W. Haag, *Rev. Sci. Instrum.* **68** (1997) 2060.

[99] A J. Jamison, A. D. Ketsdever, and E. P. Muntz, *Rev. Sci. Instrum.* **73** (2002) 3629.

[100] Manuel Gamero-Castaño, *Rev. Sci. Instrum.* **74** (2003) 4509.

[101] H. Koizumi, K. Komurasaki, and Y. Arakawa, *Rev. Sci. Instrum.* **75** (2004) 3185.

[102] H. Tahara, K. Minami, T. Yasui, K. Onoe, Y. Tsubakishita, and T. Yoshikawa, *Jpn. J. Appl. Phys.* **32** (1993) 1822.

[103] S. Kuchi-ishi, "Numerical Studies of Thermochemical Nonequilibrium Flows in a DC Arcjet Thruster," Ph.D. Dissertation, Dept. Aeronautics and Astronautics, Kyushu Univ., Fukuoka, Japan, Dec. 1999.

[104] K. H. Kim, C. Kim, and O. H. Rho, *J. Comput. Phys.* **174** (2001) 38.

[105] W. K. Anderson, J. L. Thomas, and B. V. Leer, *AIAA J.* **24** (1986) 1453.

[106] S. Yoon and A. Jameson, *AIAA J.* **26** (1988) 1025.

[107] M. S. Ivanov, G. N. Markelov, A. D. Ketsdever, and D. C. Wadsworth, *Proc. 37th Aerospace Sciences Meeting*, Reno, NV, 1999 (American Institute of Aeronautics and Astronautics) Paper AIAA-99-0166.

[108] J. D. George and I. D. Boyd, *Proc. 33rd Thermophysics Conf.*, Norfolk, VA, 1999 (American Institute of Aeronautics and Astronautics) Paper AIAA-99-3454.

[109] J. E. Brandenburg and M. E. Zooghby, *Proc. 42nd AIAA/ASME/SAE/ASEE Joint Propulsion Conf.*, Sacramento, CA, 2006 (American Institute of Aeronautics and Astronautics) Paper AIAA-2006-5179.

List of publication

Journals

1. Y. Takao and K. Ono, "Development of a Microplasma Thruster," *J. High Temp. Soc. Jpn.* **31** (2005) 283–290 [in Japanese].

2. Y. Takao and K. Ono, "A miniature electrothermal thruster using microwavew-excited plasmas: a numerical design consideration," *Plasma Sources Sci. Technol.* **15** (2006) 211–227.

3. Y. Takao, K. Ono, K. Takahashi, and Y. Setsuhara, "Microwave-sustained miniature plasmas for an ultra small thruster," *Thin Solid Films* **506–507** (2006) 592–596.

4. Y. Takao, K. Ono, K. Takahashi, and K. Eriguchi, "Plasma Diagnostics and Thrust Performance Analysis of a Microwave-Excited Microplasma Thruster," *Jpn. J. Appl. Phys.* **45** (2006) 8235–8240.

5. Y. Takao, K. Eriguchi, and K. Ono, "A miniature electrothermal thruster using microwave-excited microplasmas: Thrust measurement and its comparison with numerical analysis," *J. Appl. Phys.* (submitted).

International Conferences

1. Y. Takao, K. Ono, K. Takahashi, and Y. Setsuhara, "A Micro Plasma Thruster Using Microwave-Excited Surface Wave Discharges for Nanospacecrafts: A Numerical Study and Design," *Extended Abstracts 3rd Int. Workshop on Basic Aspects of Non-equilibrium Plasmas Interacting with Surfaces*, Awaji, Hyogo, Japan, Feb. 2003, p. 37.

2. Y. Takao, K. Ono, K. Takahashi, and Y. Setsuhara, "Micro Plasma Thruster Using Azimuthally Symmetric Surface Wave Discharges Excited by Microwaves: A Numerical Study and Experiments," *Proc. 16th Int. Symp. Plasma Chemistry*, Taormina, Italy, Jun. 2003, Paper ISPC-441.

3. Y. Takao, K. Ono, K. Takahashi, and Y. Setsuhara, "A New Type Microplasma Thruster Using Surface Wave Discharges Excited by Microwaves," *Bull. Am. Phys. Soc.* **48**(6) (2003) 55, San Francisco, CA, Oct. 2003.

4. Y. Takao and K. Ono, "Miniature Electrothermal Thruster Using Microwave Excited Plasmas: A Numerical Design Consideration and Experiment," *Proc. 24th Int. Symp. Space Technology and Science*, Miyazaki, Japan, May 2004, ISTS Paper 2004-o-1-08v.

5. Y. Takao, K. Ono, K. Takahashi, and Y. Setsuhara, "Microwave-sustained miniature plasmas for an ultra small thruster," *Abstracts 7th Asia Pacific Conf. Plasma Science and Technolgy and 17th Symp. Plasma Science for Materials*, Fukuoka, Japan, Jun. 2004, p. 316.

6. Y. Takao and K. Ono, "Development and Modeling of a Microwave-Excited Microplasma Thruster," *Proc. 40th AIAA/ASME/SAE/ASEE Joint Propulsion Conf.*, Fort Lauderdale, FL, Jul. 2004, Paper AIAA-2004-3621.

7. Y. Takao, K. Ono, K. Takahashi, and Y. Setsuhara, "Optical Emission Spectroscopy of a Microwave-excited Miniature Plasma Source for Very Small Propulsion," *Bull. Am. Phys. Soc.* **49**(5) (2004) 40, Bunratty, Ireland, Sep. 2004.

8. Y. Takao, K. Ono, K. Takahashi, and K. Eriguchi, "Optical and Electrical Diagnostics of a Miniature Microwave-Excited Plasma Source for an Ultra Small Thruster," *Proc. 17th Int. Symp. Plasma Chemistry*, Toronto, Canada, Aug. 2005, Paper ISPC-433.

9. Y. Takao and K. Ono, "Development of a Microwave-Excited Microplasma Thruster," *Proc. 29th Int. Electric Propulsion Conf.*, Princeton, NJ, Oct. 2005, Paper IEPC-2005-056.

10. Y. Takao, K. Ono, K. Takahashi, and K. Eriguchi, "Plasma Diagnostics and Thrust Performance Analysis of a Microwave-Excited Microplasma Thruster," *Proc. 6th Int. Conf. Reactive Plasmas and 23rd Symp. Plasma Processing*, Sendai, Japan, Jan. 2006, pp. 329–330.

11. Y. Takao and K. Ono, "Performance Testing of a Miniature Electrothermal Thruster Using Microwave-Excited Microplasmas," *Proc. 42nd AIAA/ASME/ SAE/ASEE Joint Propulsion Conf.*, Sacramento, CA, Jul. 2006, Paper AIAA-2006-4492.

12. Y. Takao and K. Ono, "A Miniature Electrothermal Thruster Using Microwave-Excited Microplasmas: Fabrication and Performance Testing," *CANEUS 2006 Conf.*, Toulouse, France, Aug. 2006.

13. Y. Takao, K. Ono, and K. Eriguchi, "A Microwave-Excited Microplasma Thruster: Plasma Diagnostics, Performance Testing, and Numerical Analysis," *Bull. Am. Phys. Soc.* **51**(5) (2006) 40, Columbus, OH, Oct. 2006.